Secondary Electron Yield Measurements of Anti-multipacting Surfaces for Accelerators

A Doctoral Thesis Submitted in partial fulfilment of the requirements for the award of Doctor of Philosophy

By Sihui Wang

March of 2016

Abstract

Electron cloud is an unwanted effect limiting the performance of particle accelerators with positively charged particle beams of high-intensity and short bunch spacing. However, electron cloud caused by beam induced multipacting can be sufficiently suppressed if the secondary electron yield (SEY) of accelerator chamber surface is lower than unity. Usually, the SEY is reduced by two ways: modification of surface chemistry and engineering the surface roughness. The objective of this PhD project is a systematic study of SEY as a function of various surface related parameters such as surface chemistry and surface morphology, as well as an effect of such common treatments for particle accelerators as beam pipe bakeout and surface conditioning with a beam, ultimately aiming to engineer the surfaces with low SEY for the electron cloud mitigation. In this work, transition metals and their coatings and laser treated surface were studied as a function of annealing treatment and electron bombardment. The transition metal thin films have been prepared by DC magnetron sputtering for further test.

In the first two Chapter of this thesis, the literature review on electron emission effect is introduced, which includes the process of the electron emission, the influence factor and examples of low SEY materials. In the third Chapter, the experimental methods for SEY measurements and surface investigation used in this work are described. In Chapter 4, the SEY measurement setup which is built by myself are introduced in detail. In Chapter 5 transition metals and their coatings and non-evaporable getter (NEG) coatings have been studied. All the samples have been characterized by SEY measurements, their surface morphology was analysed with Scanning Electron Microscopy (SEM) and their chemistry was studied with X-ray Photoelectron Spectroscopy (XPS). Different surface treatments such as conditioning by electron beam, thermal treatment under vacuum on the sample surfaces have been investigated. For example,

the maximum SEY (δ_{max}) of as-received Ti, Zr, V and Hf were 2.30, 2.31, 1.72 and 2.45, respectively. After a dose of 7.9×10^{-3} C mm^{-2}, δ_{max} of Ti drops to 1.19. δ_{max} for Zr, V and Hf drop to 1.27, 1.48 and 1.40 after doses of 6.4×10^{-3} C·mm^{-2}, 1.3×10^{-3} and 5.2×10^{-3} C·mm^{-2}, respectively. After heating to 350 ^{0}C for 2.5 hours, the SEY of bulk Ti has dropped to 1.21 and 1.40, respectively. As the all bulk samples have a flat surface, there are no difference of morphology. So this reduction of SEY is believed to be a consequence of the growth of a thin graphitic film on the surface after electron bombardment and the removal of the contaminations on the surface after annealing.

Chapter 6 of this thesis is about the laser treated surface. Laser irradiation can transform highly reflective metals to black or dark coloured metal. From SEM results, metal surfaces modified by a nanosecond pulsed laser irradiation form a highly organised pyramid surface microstructures, which increase the surface roughness. Due to this reason, δ_{max} of as-received laser treated surface could be lower than 1, which can avoid the electron cloud phenomenon. In this Chapter, the influence of different laser treatment parameters, such as power, hatch distance, different atmospheres on SEY has been investigated. Meanwhile, different surface treatments such as electron conditioning and thermal treatments are studied on the laser treated surface with the investigation of XPS. For example, the δ_{max} of as-received type I with hatch distance 50, 60 and 80 μm in Air are 0.75, 0.75 and 0.80, respectively. After heating to 250 ºC for 2 hours, in all case the δ_{max} drop to 0.59, 0.60, 0.62, respectively. The SEYs of all as-received samples are lower than 1 due to the increasing the roughness on the surface by the special pyramid structure. After thermal treatment, the SEY reduces even further. This is caused by removing the contaminations on the surfaces.

In conclusion, the present study has largely improved the knowledge of the electron cloud mitigation techniques by surface engineering of vacuum

chambers. On the one hand, the surface treatments can modify the surface chemistry, such as the produce the graphic carbon layer on the surface by electron condition and the removal the contamination layer on the top of the surface by thermal treatment. On the other hand, the SEY could be critically low by engineering the surface roughness. Both methods allow reaching δ_{max} less than unity. The efficiency of laser treated surface for e-cloud was demonstrated for a first time leading to a great interest to this new technology application for existing and future particle accelerators.

Key words: Electron cloud, Secondary electron yield, Transition metals and their coatings, Laser treated surfaces, X-ray Photoelectron Spectroscopy

Contents

Acknowledgments

First and foremost, I would like to express my sincere gratitude to my industry supervisors Dr Oleg Malyshev and Dr Reza Valizadeh for the support of my PhD study and research, for their patience, motivation, enthusiasm, and expertise. Their guidance helped me in all the time of practical experiments, theoretical guidance and writing of this thesis. I appreciate all their contributions of time, ideas and funding to my PhD experience productive and interesting. I could not successfully complete my PhD project without their support and advice.

I would also like to thank to my university supervisor, Dr Mike Cropper for supporting me during these past four years. Mike is the most understanding, easy-going supervisor and one of the smartest people I know. I hope that I could be as lively, enthusiastic, and energetic as Mike. He has been supportive and provided insightful discussions about the research. He gave me very useful resource for the answer of my science questions and was instrumental in helping me writing this thesis.

Very special thanks go out to Dr Elaine Seddon. Without her motivation and guidance, my experiments would proceed with a lot of difficulties. I am very grateful that she spent almost every day with me to teach me how to design good physics experiments in the first year, which lays a good foundation for me to build my own setup in the second year and obtain all my results in the third year. The joy and enthusiasm she has for research was contagious and motivational for me.

The members of the Vacuum group have contributed immensely to my personal and professional time at the work. Mr Adrian Hannah and Mr Neil Pashley gave me detail practical experimental directions, which helped me gain a great knowledge of vacuum design and application. The students of the group have brought me a source of friendships as well as good advice and collaboration. I

am thankful to Miss Sonal Mistry, Mr Stuart Wilde, Mr Paolo Pizzol. I should thank to Mr Mark Roberts for helping me to do these measurements.

Most important, I take this opportunity to express the profound gratitude from my deep heart to my parents, grandparents for their unflagging love and unconditional support throughout my life and my studies. The best outcome from these past four years is to marry the best person in the world in my mind, Dr Yonghao Gao. He has unconditionally loved, supported and encouraged me during my good and bad times. I could overcome the difficulties easily with his love.

Finally, I appreciate the financial support from AsTeC and university, which made my life much easier during my PhD.

List of Abbreviations:

SEY	Secondary Electron Yield
NEG	Non-evaporable Getter
SEM	Scanning Electron Microscopy
XPS	Photoelectron Spectroscopy
RF	Radio Frequency
ISR	Intersecting Storage Rings
SEE	Secondary Electron Emission
SR	Surface roughness
EE	Elastic Electron
RE	Re-scattered Electron
SE	Secondary Electron
PVD	Physical Vapour Deposition
XRD	X-ray Diffraction
BE	Backscattered Electron
PEY	Photon Electron Yield
SPS	Super Proton Synchrotron

Figure Captions

Table Captions

Chapter 1. Introduction

1.1 Background

The electron cloud (e-cloud) is an unwanted limitation in operating particle accelerators such as (Large Hadron Collider) LHC and B-factory (KEKB with positively charged beams of high-intensity and short bunch spacing [1]. The original electron in the chamber comes from residual gas molecules ($\mathrm{X} \rightarrow \mathrm{X}^{+} + e^{-}$) by beam particles, photoelectron ($\mathrm{X} + \mathrm{hv} \rightarrow \mathrm{X}^{+} + e^{-}$) and secondary electron emission ($\mathrm{X} + 2e^{-} \rightarrow \mathrm{X}^{+} + 3\mathrm{e}^{-}$) from the vacuum chamber walls under synchrotron radiation emitted by accelerated particles in dipoles and quadrupoles. These original electrons are accelerated by the electric field of the passing bunches and acquire kinetic energies of up to several hundreds of eV. Meanwhile, they can produce secondary electrons by colliding with both the charged particle beam and the walls in the vacuum chamber [2]. An electron multipacting may happen in the case of the resonant movement generated by the electromagnetic field of the beam pattern [3]. Electron multipacting is a high frequency vacuum conduction phenomenon. For example, in RF cavity, an initial electron leaves a point on the surface is driven by the RF field and impacts again at the same point after an integer number of RF periods for the case of single-point electron multipacting [4]. Overall, the photon electron emission, residual gas ionisation and secondary electron emission are the significant sources of electrons and then these electrons impact with energies in the range of 100 to 300 eV. If the secondary electron yield (SEY, written as ‘δ’, the number of secondary electrons over the number of primary electrons) of the chamber wall is greater than unity then under certain resonant conditions of beam pattern, beam induced multipacting will happen and the electron density will be increased to several orders of magnitude over the primary electron density. These lead to the build-up of e-cloud [5]. The secondary electron emission will be introduced in detail in Chapter 2.

E-clouds can affect the operation and performance of high-energy charged particle accelerators in a variety of ways, for example, the increase of vacuum pressure, beam instability, beam losses, emittance growth, reduction of the beam lifetime and additional heat loads on a cryogenic vacuum chamber [6]. The secondary electrons can also affect the performance of other instruments. In radio frequency (RF) waveguides, electron multipacting leads to power loss and multipacting electrons damage the surface and limit the lifetimes of the wave guides. In detectors, the secondary electrons increase the background of the signal and reduce the sensitivity. In addition, satellites in space suffer from similar problems with e-cloud in accelerators and waveguides, which included the motion of satellites through electron clouds in outer space, the relative charging of satellite components under the influence of sunlight and the performance loss of high power microwave devices on space satellites [2].

The sufficient condition to suppress the effect of electron multipacting is $\delta<1$. It has been proven both theoretically and experimentally that the build-up of e-cloud density depends on the SEY function $\delta(E)$ over all electron impact energy and beam bunch parameters. In order to suppress the effects of e-cloud, the maximum value of $\delta(E)$, $\delta_{max}=\max(\delta(E))$, should be less than a certain threshold value, for example, $\delta_{max}<1.3$ in the Super Proton Synchrotron (SPS) at CERN [7, 8].

The first observation of e-cloud was discovered at a small proton storage ring of the INP Novosibrisk in Russia around in 1965. The first observation of e-cloud at CERN was in the world's first hadron collider (Intersecting Storage Rings (ISR)) in 1972. The first detailed theory of the e-cloud effect has been summarized and discussed by F. Zimmermannin [1]. The SEY gradually reduces in time with particle accelerator operation due to electron bombardment of the vacuum chamber walls by the e-cloud. This decrease is known as the "conditioning effect" which changes the surface chemistry through a gradual build-up of a thin layer of graphitic-like C-C bonded carbon. However,

in many cases δ_{max} may still not be able to be low enough to avoid the e-cloud phenomenon even with δ(E) reducing to its lowest levels [9]. In the past 15 years, significant effort has been made to mitigate e-cloud through a number of techniques. There are three main ways to eliminate e-cloud: (1) Modification in the vacuum chambers such as mechanical grooving [10], clearing electrodes [11] and external solenoid windings [12]. However, mechanical grooving and clearing electrodes can hardly be implemented in an existing accelerator without reducing the machine aperture. The solutions of solenoids have been applied successfully in the straight sections of KEKB at KEK to mitigate the electron cloud [13]. However, it cannot apply in the case of dipoles or quadrupoles. (2) Modification of the surfaces of vacuum chamber such as introducing low SEY thin film coatings. (3) Modification of beam bunch parameters.

1.2 The goal of this study

The aim of this project was to systematically study low SEY materials and engineer surfaces for accelerator vacuum chamber. The project commenced with design, producing the components and building up the new SEY measurement facility. The theory and experimental methods used for measuring SEY, as well as the SEY measurement facility has been described in detail in the Chapters 2-4, correspondingly.

In the work reported in this thesis, two classes of materials have been studied: the transition metals (Ti, Zr, V and Hf) in form of both bulk sample and their coatings in Chapter 5 and nanosecond pulsed laser treated metal surfaces in Chapter 6. Non-evaporable Getter (NEG) is composed by transition elements. After activation (heated to atomically clean surfaces), the NEG coatings have low SEY and a large pumping speed [13]. They have been used in the particle accelerators, for example, Ti-Zr-V thin film have been applied in long straight sections of the LHC due to its low SEY, , low photon stimulated desorption and

pumping properties [14]. In Chapter 5, SEY between the transition bulk metals and their coatings have been studied as a function of electron bombardment and thermal treatment. Then Ti-Zr-V thin films on stainless steel and silicon substrates have also been investigated as a function of electron bombardment and thermal treatment. The morphology for all coatings has been shown by Scanning Electron Microscopy (SEM). Photoelectron Spectroscopy (XPS) analysis has been measured for all the samples before and after each treatment to determine surface chemical composition of the surface. Other materials we are interested in are nanosecond pulsed laser treated metals (Cu, Stainless steel and Al alloys) due to their critically low SEY, no inducing materials and low cost. After laser treatment, the SEY can be dramatically reduced due to special pyramid microstructures. This surface treatment only modifies the surface microstructure and is easy to apply to existing vacuum surfaces with minimum disturbance to the in-situ beam line. The actual cost of this so called 'blackening' process is low. In addition, the surface is highly reproducible and is very stable [2]. In Chapter 6, the SEYs of different nanosecond pulsed laser treated surfaces on the Cu as a function of thermal treatment with XPS analysis have been studied. The influence of electron bombardment to nanosecond pulsed laser treated surface on the Cu, Al alloys and 316L SS have also been introduced in this chapter with XPS analysis.

1.3 Conclusion

E-cloud is an unwanted limitation in operation accelerator due to its side effects, such as increase of vacuum pressure, beam instability, beam losses and so on. In this thesis, low SEY materials have been studied to avoid e-cloud phenomenon, which include transition metals and their coatings and laser treated metals. Before these studies, the SEY measurement setup has been designed and built. SEY studies are accompanied by the effects of electron conditioning and thermal treatments. Besides that, the analysis of SEM and XPS have been studied in order to investigate the surface composition and

morphologies before and after each treatment.

References

[1] Zimmermann F. Review of single bunch instabilities driven by an electron cloud. Physical Review Special Topics - Accelerators and Beams 2004;7:124801.

[2] Valizadeh R, Malyshev OB, Wang S, Zolotovskaya SA, Allan Gillespie W, Abdolvand A. Low secondary electron yield engineered surface for electron cloud mitigation. Applied Physics Letters 2014;105:231605.

[3] Le Pimpec F, Kirby RE, King F, Pivi M. Properties of TiN and TiZrV thin film as a remedy against electron cloud. Nuclear Instruments and Methods in Physics Research Section A: Accelerators, Spectrometers, Detectors and Associated Equipment 2005;551:187-99.

[4] Lyneis C M, Schwettman H A, Turneaure J P. Elimination on electron multipacting in superconducting structures for electron accelerators[J]. Applied Physics Letters, 1977, 31(8):541-543.

[5] Furman MA. Electron Cloud Effects in Accelerators. The fifth Electron-Cloud Workshop, ECLOUD12. La Biodola, Isola d'Elba, Italy2014.

[6] Grosso DR, Commisso M, Cimino R, Larciprete R, Flammini R, Wanzenberg R. Effect of the surface processing on the secondary electron yield of Al alloy samples. Physical Review Special Topics - Accelerators and Beams 2013;16:051003.

[7] Pinto PC, Bellunato A, Basso T, Edwards P, Mensi M, Sublet A, et al. Implementation of carbon thin film coatings in the super proton synchrotron (SPS) for electron cloud mitigation. Link to Fulltext 2014.

[8] Giovannozzi M, Métral E, Métral G, Rumolo G, Zimmermann F. Electron cloud buildup and instability: Numerical simulations for the CERN Proton Synchrotron. Physical Review Special Topics - Accelerators and Beams 2003;6:427-33.

[9] Cimino R, Commisso M, Grosso DR, Demma T, Baglin V, Flammini R, et al. Nature of the Decrease of the Secondary-Electron Yield by Electron Bombardment and its Energy Dependence. Physical Review Letters 2012;109:064801.

[10] Pivi M, Collet G, King F, Kirby R, Markiewicz T, Raubenheimer T, et al. Secondary electron yield and groove chamber tests in PEP-II. Particle Accelerator Conference, 2007 PAC IEEE2007. p. 1997-9.

[11] Suetsugu Y, Fukuma H, Wang L, Pivi M, Morishige A, Suzuki Y, et al. Demonstration of electron clearing effect by means of a clearing electrode in

high-intensity positron ring. Nuclear Instruments & Methods in Physics Research 2009;598:372-8.

[12] Fukuma H, Flanagan J, Hosoyama K, Ieiri T, Kawamoto T, Kubo T, et al. Status of Solenoid System to Suppress the Electron Cloud Effects at the KEKB. AIP Conference Proceedings 2002;642:357-9.

[13] Zemek J, Jiricek P. XPS and He II photoelectron yield study of the activation process in Ti–Zr NEG films. Vacuum 2003;71:329-33.

[14] Henrist B, Hilleret N, Scheuerlein C, Taborelli M. The secondary electron yield of TiZr and TiZrV non-evaporable getter thin film coatings. Applied Surface Science 2001;172:95-102.

Chapter 2. The Basic Theory of Secondary Electron Yield

The phenomenon of secondary electron emission (SEE) was discovered by Austin and Starke in 1902 [1]. However, there was little interest until electronic tubes came into general use when SEE was investigated in more depth.

When electrons or ions of sufficient kinetic energy hit a surface or pass through a material, electrons are emitted from the surface. These emitted electrons are called secondary electrons, the incident electrons are called primary electrons. A part of primary electron beam is reflected.

2.1 Basics of SEE

When a surface is hit by an electron beam, SEE is caused by energy transfer [2]. The secondary electrons come from the outer layers of the target. The secondary emission process has three steps; 1) the generation of secondary electrons, 2) transport to the surface and 3) emission from the surface, as shown in **Figure 2-1**. As the primary electron energy is increased the primary beam goes in deeper and deeper into the metal, transferring energy to the metal atoms and their electrons. Most secondary electrons are absorbed into the bulk, few electrons can escape from the surface.

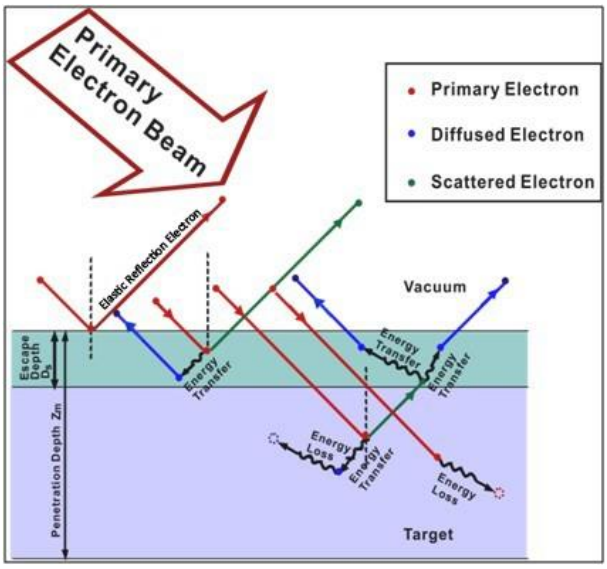

Figure 2-1. Schematic secondary electron emission process.

A) Generation of Secondary Electrons

Secondary electron generation occurs in the interaction volume, where the secondary electrons interact with the bulk materials. The penetration depth (Z_m) of primary electrons varies with primary electron energy and the chemical composition of the target. For example, for primary electrons from 3 to 2000 eV the penetration depth varies from a few to tens of nanometres [3].It has been recognised that the penetration depth increases with the primary electron energy. It is clearly shown in the **Figure 2-2** which can be explained by a simple description of the primaries move through the solid: the high-velocity electrons at high primary energies have a relatively short time to interact with the lattice electrons. So the internal yield per unit length is low. Then the primary electrons lose energy, so the interaction time and the yield increase. The combined effect is that the internal secondary electrons originate deeper through the surface with the increases of primary electron energy [4].

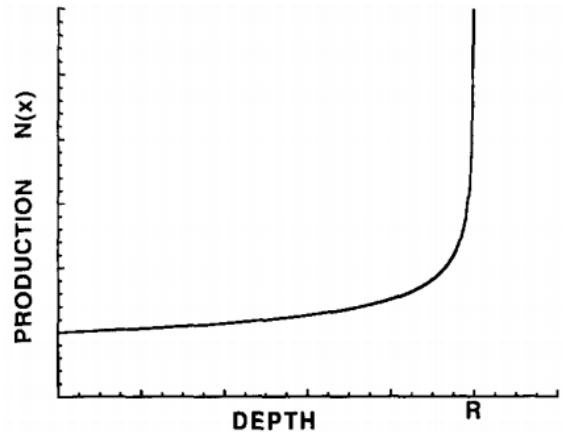

Figure 2-2.The production rate of internal secondary electrons as a function of distance along the primary electron path [4]

The shape of the SEY curve as a function of primary electron energy can be explained by the relations between penetration depth and escape depth [4]. At very low primary electron energies ($Z_m \leq d_s$, E <~50 eV), only a few secondary electrons are generated. As the number of internal secondary electrons created increases with primary energy, SEY also rises with increasing primary energy. However, at very high primary energies ($Z_m \geq d_s$, E >~50 eV), the secondary electrons have been absorbed into the bulk instead of escaping from the surface. Thus, SEY decreases with increasing primary electron energy. The SEY reached a maximum value at a primary energy when $Z_m = d_s$.

If the incidence of the primary beam is at an angle θ to the surface, the maximum penetration depth is reduced by a factor $\cos\theta$ relative to the normal incidence. Thus, the SEYs are larger at angles, and the enhancement in yield is more apparent at the higher primary electron energies for which $Z_m \geq d_s$.

B) Secondary Electron Transport

The secondary electron generation is isotropic. However, only a fraction of these electrons will migrate to the surface. Most secondary electron are not always observed because most secondary electrons lose energy through collisions and fall below vacuum level. A secondary electron can have many

different interactions, such as electron-electron, electron-vacancy, and electron-phonon, etc. Only those that are travelling towards the surface and are generated on a depth less than the escape depth d_s can eventually reach the vacuum/surface interface [2] In metals, the secondary electrons lose energy by interacting with electrons and defects. The kinetic energy of a secondary electron must be at least $E_F+\Phi$ when it has enough energy to escape out of the surface，where E_F is the Fermi energy and Φ is the metal work function. The minimum escape energy $E_F+\Phi$ of metal is typically about 10 eV. The large minimum escape energy and the high collision probability due to the large number of conduction electrons cause the low SEY of metals. However, in insulating materials, the minimum kinetic energy for a secondary electron to escape is the electron affinity χ, which is the difference between the vacuum level and the conduction-band minimum. The electron affinity is typically about 1 eV for insulators. Due to the small number of conduction electrons in insulators, the secondary electrons lose energy through the excitation of valence electrons into the conduction band. The wide band gap prevents secondary electrons less than E_{gap} from the electron-electron collisions. Electron to phonon and electron to impurity collisions are mainly responsible for the energy loss. So due to the absence of electron to electron scattering, the secondary electron loses much less energy when it moves through material to the surface and the escape depth becomes large, where d_s can be about 100 nm [3-5]. Therefore, the SEY of insulators are general high.

C) Emission from the Surface/Vacuum Barrier

Once a secondary electron reaches the target surface it must have enough energy to escape from the material. For a metallic target this extra energy is known as the work function. The secondary electrons from the target surface have low energy and come from the surface vicinity. Hence, the state of target

surface, such as oxidation, contamination and thermal treatment is very important for SEE [6, 7].

2.2 Work function

The work function of a metal is defined as the difference between the electrochemical potential inside the metal and the electrostatic potential outside the metal [8]. The work function corresponds to the minimum amount of energy which is needed to remove an electron from the metal. The value of the work function has a great influence to determine the rate of electron emissions from a metal surface. The work function of a surface is strongly affected by the condition of the surface, such as the roughness, the contamination and so on [9].

2.2.1 Contamination effect on the work function

The work function depends on both the electronic structure of the individual ion and the crystallographic structure of ion assemblies. However, it is profoundly affected by the surface contaminations adsorbed on the metal surface (sometimes no more than one atomic layer in thickness). The effect of this impurity layer is particularly noticeable in electron tubes which depend on the thermionic electron emission for their operation. The thermionic electron emission from a metal surface may be influenced by an adsorbed layer, which may increase the electron emission for some contaminants or decrease emission for others. The change of work function is attributed to the rearrangement of electronic structure of the outermost layers, which has a tendency to decrease the surface energy.

A physically adsorbed layer on the metal surface gives rise to very little change in the work function since the adsorption mechanism brings about only slight rearrangement of the adsorbed material. On the contrary, the electronic structures of impurity atoms which are attached by chemisorption are affected

strongly both in the absorbate and in the metal. This rearrangement gives rise to the formation of a dipole layer. The conduction electron will penetrate the dipole layer, and also pass through the surface barrier to become a free electron external to the metal. As a result, the direction of electron movements in the bonding process determines whether the work function is increased or decreased. For example, cesium atoms have a very low ionisation potential which is about 3.9 eV. When cesium atoms deposited on the metal surface, they tend to lose electrons to the metal. So they produce a dipole layer with the negative sides adjacent to the metal and the positive side on the surface. In contrast, oxygen has an affinity for electrons. When it bonds onto a metallic surface, the electrons are attracted from the metal. Thus, a dipole layer is formed with the positive side adjacent to the metal and the negative side on the surface. As expected, the effects on the work function of surface contamination by these two materials are opposite in nature. As a result, the SEY of an oxide layer is usually much higher than that of atomically clean surface. In addition, the work function of copper can be increased by the adsorption of oxygen and decreased by the adsorption of water vapour [10].

2.2.2 Roughness effect on the work function

Surface roughness (SR) is a configurational characteristic of a surface and plays an import role in determining physical, chemical and mechanical behaviour of the surface. However, both experimental and theoretical research on the effect of surface roughness and work function is very rare and some existing results are even controversial [8, 11]. Generally, the larger the surface roughness is, the smaller the work function is. It is generally explained by surface roughness effect on the dipole barrier. However, the effect of surface roughness on the work function is always accompanied by other factors, such as oxidation and contamination on the surface.

2.3 Energy distribution of SE emission

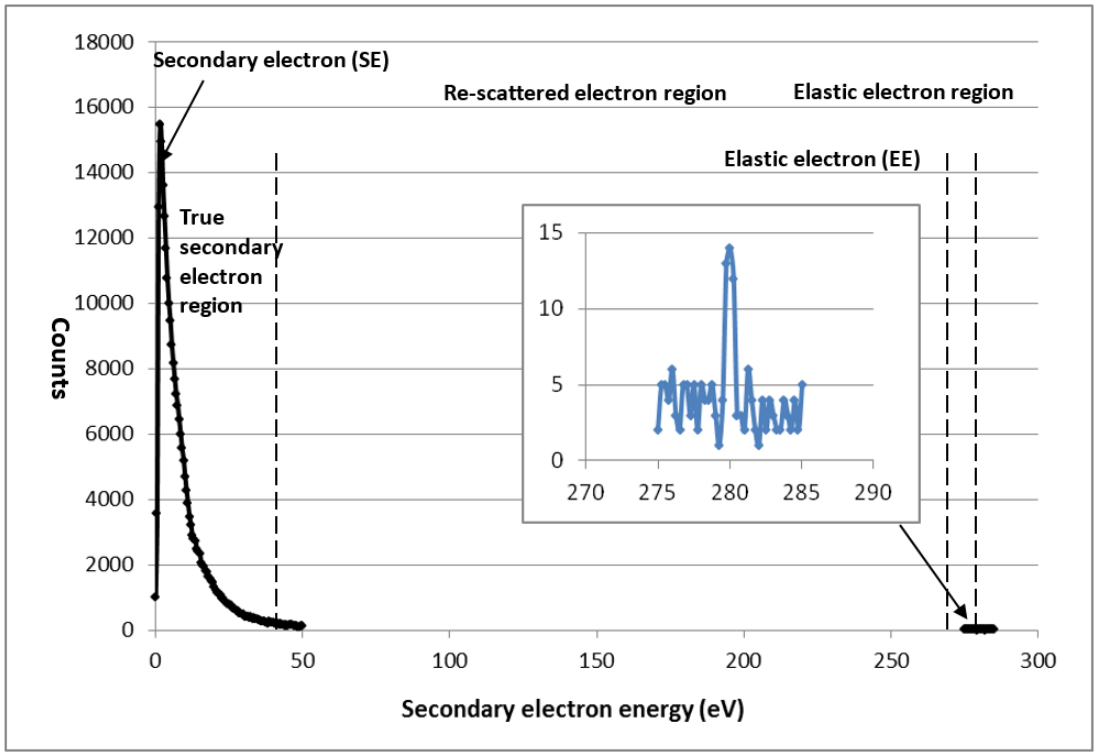

Figure 2-3 Energy distribution of electrons emitted by stainless steel upon bombardment with 280 eV primary electrons.

The SEE can be principally divided into three energy regions, these are the elastic electron (EE) region, the re-scattered electron (RE) region and the true secondary electrons (SE) region [12, 13]. **Figure 2-3** shows an example of an electron energy distribution curve. The first peak (0-50 eV) represents SE region. The second peak about 280 eV is EE region. The energies between 50 and 280 eV is RE region.

(a) Elastically scattered electrons

The EE region covers the elastically scattered electrons of the primary electron beam. The elastic electron reflection increases at low energies, where the SEY approaches unity. This means that low energy electrons persist for a long time in the accelerator vacuum chamber.

(b) True secondary electrons

The true SE region comprises arbitrarily those electrons with emission energy from 0 eV up to 50 eV.

(c) Re-scattered electrons

The RE region covers the emission of electrons with energies between 50 eV and the elastic peak.

2.4 Theory calculation of secondary electron emission

The classic elementary theory initially proposed by Bruining [14]. Based on this assumption, Dionne developed the semi-empirical theory, where the secondary electron yield δ as a function of the energy E_0 of the incident primary electrons may be written in the form [15, 16]

$$\delta = \int \boldsymbol{n}(\boldsymbol{x}, \boldsymbol{E_0}) \boldsymbol{f}(\boldsymbol{x}) \boldsymbol{dx} \qquad \text{Eq.(2-1)}$$

where $n(x, E_0)dx$ represents the average number of secondary electrons produced per incident primary electron with energy E_0 in the layer of thickness dx at a depth x below the surface.

In **Eq.(2-1)**, $f(x)$ represents the probability for a secondary electron to migrate to and escape from the surface. For the one-dimensional model. It is generally assumed that

$$\boldsymbol{f}(\boldsymbol{x}) = \boldsymbol{B}\boldsymbol{e}^{-\boldsymbol{\alpha x}} \qquad \text{Eq.(2-2)}$$

It is generally assumed that $n(x, E_0)$ is proportional to the average energy loss per unit path length

$$\boldsymbol{n}(\boldsymbol{x}, \boldsymbol{E_0}) = -\frac{\mathbf{1}}{\varsigma}\left(\frac{\boldsymbol{dE}}{\boldsymbol{dx}}\right) \qquad \text{Eq.(2-3)}$$

where ς is the average energy required to produce one secondary electron inside the solid; relate to ϕ: work function for metal or χ+E_g: electron affinity plus

band gap for insulators or semiconductors.

Where B is escape probability for an excited electron that reaches the surface and is $\propto$ 1-*r*, where *r* is a quantum-mechanical reflection coefficient which may depend on the physical condition of the surface. α is the secondary electron absorption constant equivalent to an inverse diffusion length and $\propto$ is electrical conductivity.

Thus, upon substitution of **Eq.(2-2)** and **(2-3)** into **Eq.(2-1)**, the δ as a function of incident electron energy E becomes:

$$\boldsymbol{\delta = -\left(\frac{B}{\varsigma}\right)\int\left(\frac{dE}{dx}\right)e^{-\alpha x}dx} \qquad \text{Eq.(2-4)}$$

The primary electrons are assumed to travel in a straight-ahead path, but slow down through collisions with electrons and ions and transfer kinetic energy to internal secondary electron generation. Most of the theories treat the energy loss of the primaries are governed by a power law:

$$\boldsymbol{\frac{dE}{dx} = -\frac{A}{E^{n-1}}} \qquad \text{Eq.(2-5)}$$

where E is the energy of a primary electron at a depth x, A is a constant characteristic of the material and n is power-law exponent. (n =1.35 has been used widely since it provides the most reasonable fit to the experimental data). The integration of **Eq.(2-5)** reaches:

$$\boldsymbol{E^n(x) = E_o^n - Anx} \qquad \text{Eq.(2-6)}$$

From **Eq.(2-6)**, it clearly shows that the maximum penetration depth *d* (where $\mathrm{E^n(x) = 0}$) as:

$$\boldsymbol{d = \frac{E_0^n}{An}} \qquad \text{Eq.(2-7)}$$

If the scattering of primaries has been taken into account, it was suggested that

not all the primaries reach a depth *d* and some have been scattered with a constant energy loss through the range. Then the number of secondary electrons produced per unit length would be constant and the number of primaries would decrease linearly with a depth d:

$$\frac{dE}{dx} = -\frac{E_0}{d} = -\varsigma n(x, E_0) \qquad \text{Eq.(2-8)}$$

Upon substitution of Eq.(2-8) into Eq. (2-4), then it becomes:

$$\delta = \left(\frac{B}{\varsigma}\right) \int_0^d \frac{E_0}{d} e^{-\alpha x} dx \qquad \text{Eq.(2-9)}$$

which may be integrated to get the following form:

$$\delta(E_0) = B \cdot \frac{E_0}{\varsigma d} \cdot \frac{\left(1 - e^{-\alpha d}\right)}{\alpha} \qquad \text{Eq.(2-10)}$$

2.5 Existing methods used to suppress electron clouds

A number of possible remedies for electron clouds have been studied so far these are:

(i) Modification of the vacuum chamber

(a) Beam pipe geometry and size, such as ante-chambers

(b) Clearing electrodes [17, 18] chambers with grooves [19] and solenoids [20]. Both of them require power supplies, controller and cables.

(ii) Beam parameters

Beam parameters include the bunch spacing, the number of bunches and the charge bunch intensity. All these parameters affect the resonant optimum for electron multipacting and secondary electron emission. Therefore, beam parameter optimisation aims to turn parameters away from a resonance and

reduce the energy that electrons gain in the beam electric field. The disadvantage of this method is the limited tuning range of beam parameters as they are selected for the experiment for which the accelerator is designed.

(iii) Low SEY of the surface materials

Low SEY coatings, such as TiN, C, and Ti or its alloys, have been applied on the basic accelerator chamber. However, SEE as a surface process is influenced by different surface properties, such as surface roughness, surface contamination and cleaning processes. The great advantages of this method are that, once the coating is deposited, it does not require in-vacuum connection, it does not reduce the machine aperture or affect the beam parameters, and finally it is low cost. However, the limitation of these methods is the in-vacuum deposition.

Another new technology reported is to produce blackened surfaces, which are nanosecond pulsed laser treated surfaces [21]. This technology forms highly organised surface microstructures and emission electrons from the surface are absorbed by itself. This technique is easy to apply to the existing vacuum surface and keep the materials the same. The actual cost of the technology is low and it provides a very stable surface chemistry.

2.5.1 The influence of surface treatment on SEY

Although many experiments are performed on clean well defined metal surfaces (which is important for understanding the basic processes involved) the internal surfaces of accelerators, of whatever material, have been exposed to air, water and often other contaminants. As SEY is affected by different modifications of a material's outer layers, the SEY on the as-received surface is much higher than that of pure clean materials. Also some surface treatments can be applied to reduce the SEY, such as rough surfaces (grooved), thermal treatment and ion and electron bombardment. Thus, in the following sections,

the effect of different surface treatments will be considered.

2.5.2 Suppression of the SEY for a grooved (rough) metal surface

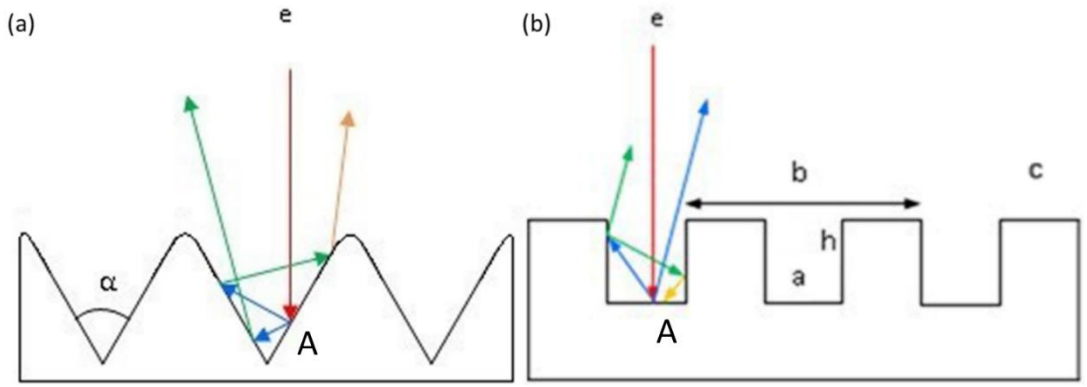

Figure 2-4 (a) Triangular grooves are characterized by the angle α. (b) Rectangular grooves have a period b width a and depth h.

Previous work has found that a grooved surface has a lower secondary electron yield than a flat one. Two different geometries of grooves, triangular (with angle α) and rectangular (characterized by the period *b*, width *a* and depth *h*) have been studied, and schematically illustrated in Figure 2-4 [22].

A primary electron (shown in red) hits the surface at Point A produces secondary electrons shown in blue. Due to different emission angles, some of the secondary electrons can escape the groove and move away from the surface. However, the others continue hitting the groove sides. With some probability they will be absorbed, the rest continue generating other secondary electrons (which are called second generation secondary electrons and are shown in green). This process may repeat several times until the higher generations of the secondary electron energies are so low that the electrons cannot escape from the surface and they are eventually absorbed by the surface.

Although several collisions of the secondary electrons with the groove sides reduce the SEY there is also a competing mechanism for triangular grooves

that increases the SEY. This is because a primary electron that travels perpendicularly to the horizontal surface in Figure 2-4 would in the grooved case hit the surface of the groove at an angle of (π-α)/2 relative to the normal to the surface. As the SEY usually increases with the angle of incidence relative to the surface normal of the primary electron, so the number of first generation secondary electrons on the triangular grooved surface will be larger than that on a flat surface. So the SEY of a triangular grooved surface does not only depend on the size of the grooves. In fact the most important factor is the angle *α*. The smaller the angle *α* is, the larger SEY of the triangular grooved surface.

For rectangular grooves, the higher the aspect ratio (h/a) and the higher the fraction a/b of the rectangular grooves, the higher the suppression of secondary emission is. In both cases the deeper the grooves the greater the suppression of secondary emission will be. The limitation of this approach is that no suppression effect occurs on the top of the grooves, *e.g.* the flat angle of the triangular grooves and the flat top of the rectangular grooves c shown in Figure 2-4 (b).

Similarly, the rough surface usually has a lower SEY than that on the flat surface. The reason is that the secondary electrons leave from a rough surface and they may again intercept with surrounding substance, which is similar with the grooved surface. Then a big fraction of secondary electrons will be absorbed by the surface instead of escaping from the surface. Therefore, the SEY is critically low [14].

2.5.3 The influence of thermal treatment on SEY

Air-exposed metals can have a high SEY due to the formation of insulating surface oxides or a hydroxide layer [7]. Adsorbed gases and oxidation layers can be removed by surface heating. For example, Stainless steel, copper and aluminium need to be heated to 673 K, 523 K and 473 K respectively, in order

to reach pressures < 10^{-5} mbar for vacuum applications [23].

2.5.4 The influence of electron conditioning on SEY

Surface conditioning with an electron beam is well-developed and powerful method to deal with problems related with electron multiplication.

Researchers at SLAC and CERN have made efforts to understand the effect of electron beam bombardment on the SEY of copper. They found that electron bombardment of copper results in desorption of gases followed by electron-induced adsorption of carbon-containing residual gas molecules [24, 25].

R. Cimino *et. al.* [26] describe the nature of the decrease of the SEY by electron bombardment. Cu as received surface, a representative of the large hadron collider accelerator inner walls converts the sp3 hybridized C atoms into a network having predominantly sp2 bonds, which is indicated by the appearance of the graphitic component after electron irradiation at 500 eV. Hence, the electron bombardment modifies the chemical state and produces a graphite-like layer on the copper surface. This graphitization process causes a decrease of the SEY value.

2.5.5 The influence of ion bombardment on SEY

The surface composition of solid materials are often different with the bulk itself due to the surface chemical reactions, particularly with typical atmospheric components such as O_2, CO_2, H_2O, etc. [27] Ar^+ sputtering is a useful technique for removing the surface layers on the metals and creating a surface whose composition reflects that of the bulk material [27]. For example, the influence of the dose of argon ions on cleaning Al (6061) by argon ion bombardment has been studied [28]. The initial SEY is 3 at 300 eV, however, the SEY value reduces with increasing dose to the pure aluminium value of 0.95 [28].

2.6 Examples of low SEY materials

There are many materials or coatings used for reducing SEY, such as TiN [29, 30], NEG coatings [31] and various carbon coatings [32, 33]. In the recent years, the significant interest was paid to NEG and amorphous carbon coatings.

2.6.1 Non evaporable getters

Non evaporable getter (NEG) thin film coatings are currently being used in the ultra-high vacuum (UHV) system of many particle accelerators, for example in the Large Hadron Collider (LHC). NEG coatings normally consist of Ti, Zr and V deposited by PVD [34]. The selection of getter materials should meet the requirements as below [35].

(1) During the activation, oxygen from the surface oxides is dissolved in the materials bulk by heating. The activation temperature of the getter is low but implies high oxygen diffusivity. The activation temperature should not be over the maximum baking temperature allowed by the mechanical properties of construction materials. For example, the temperature for stainless steel is not higher than 300 ^{0}C or even not higher than 250 ^{0}C for vacuum chambers made of copper and 180 ^{0}C for aluminium alloys.

(2) A high oxygen solubility limitation is required to allow many activation air exposure cycles. To guarantee a reasonable getter life time, a desirable limit of solubility is at least 10%.

(3) In order to have a large pumping capacity for H_2 at ambient temperature and under UHV conditions, the getter should provide high diffusivity and form a hydride phase with low dissociation pressure. So the ideal material should offer a large adsorption for all typical residual gas inside UHV vacuum systems, such as H_2, CO, N_2.

(4) In addition, the selected getter material should also present other essential characteristics, such as good adhesion to the substrate, high mechanical resistance and high melting point to resist cathode heating during the coating process. Furthermore, the getter should be non-toxic, non-pyrophotic. Finally, the most important thing is that it should be non-magnetic and provide a low photoelectric and secondary electron yield to reduce the electron emission and avoid electron multipacting.

Overall, the elements of the column IV B of the chemical periodic table fulfil all these requirements best, i.e. Ti, Zr, Hf. The most restrictive requirement is the high oxygen solubility limitation, which exceeds 10% for these elements only. Therefore, Ti, Zr Hf and their binary combinations have been taken as important getter materials to study. However, another family of elements, column VB (i.e. V) present much higher oxygen diffusivity but a low oxygen solubility limitation. As a result, elements of IV and V columns were combined to produce the ternary or quaternary coatings. This then is the origin of the NEG.

NEG coatings are deposited onto the inner walls of accelerator vacuum chambers to deal with surface outgassing. Surface outgassing is the release of residual gas that dissolved or absorbed in the accelerator chamber. The clean NEG surface could absorb residual gas in the chamber. After baking, NEG films exhibit a good pumping character and low outgassing [36]. This means that NEG surface could absorb residual gases in the chamber and release very little gases. In addition, a clean NEG surface reduces the SEY and photon and electron stimulated desorption yields (PSD and ESD respectively). NEG coatings have the large of oxygen solubility and oxygen diffusivity. NEG coatings also have high reactivity to the residual gases in UHV system (H_2, O_2, CO, CO_2, H_2O and N_2), good adhesion to the typical substrate materials (stainless steel, aluminium and copper), magnetic permeability near 1 [36]. These important characteristics help to improve beam stability and beam lifetime [35]. However, the NEG surface must be clean in order to adsorb gas

molecules. The activation procedure is shown in Figure 2-5. When native oxide layers are on the surface of NEG at room temperature, there is no pumping properties. Clean surfaces of getters are obtained by baking to temperature high enough to dissolve the native oxide layer into the bulk. This process is called activation. The NEG coatings require a lower activation temperature than stainless steel (673 K), copper (523 K) and aluminium (473K) in order to reach pressures < 10^{-5} Pa for ultra-high vacuum (UHV) applications [37]. After activation, NEG starts to show a good pumping property at room temperature.

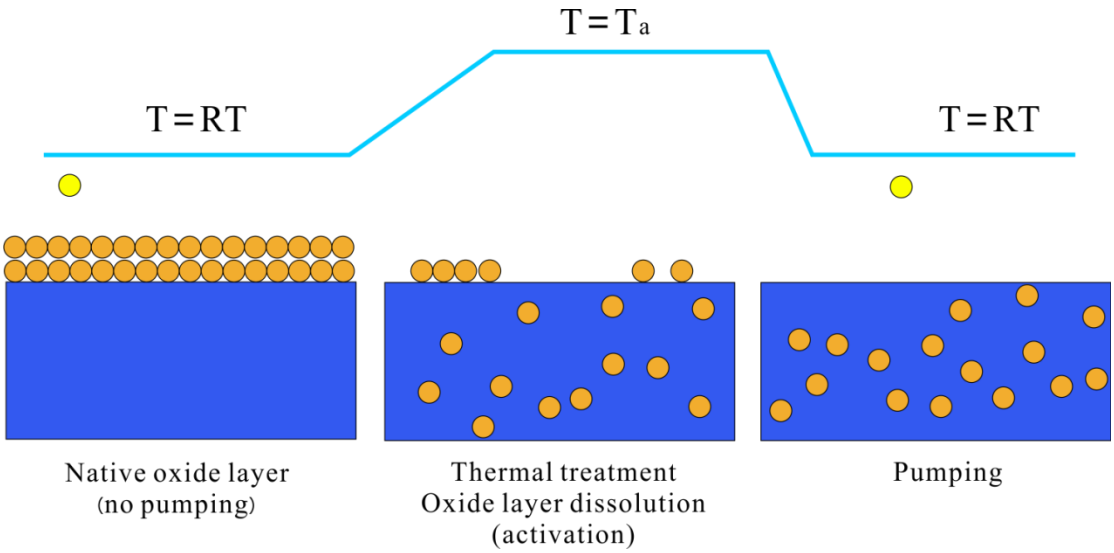

Figure 2-5 The process of thermal treatment for NEG coatings and their pumping properties after activation

2.6.2 Carbon coatings

Most carbon coatings have a maximum SEY in the range of 0.9 to 1.1 after air-transfer to the measurement instrument. The SEY of amorphous carbon (α-C) coatings after bake-out at 150 ℃ measured at room temperature and at 4.7 K show no significant difference at 1.12 [38]. These coatings can be applied to the cryogenic systems of an accelerator and their performance has been demonstrated in the Super Proton Synchrotron (SPS) at CERN.

2.7 Conclusion

In this chapter, the basic theory of secondary electron yield has been described. Secondary electrons are emitted from the surface when electrons or ions with sufficient kinetic energy hit or pass through a material. The secondary emission process includes the secondary electron generation, transport to the surface and emission from the surface. Secondary electrons should overcome the energy of work function before emitting from the materials. The energy distribution of SE emission is divided to elastic electron region, re-scattered electron region and true secondary electron region. The energy of secondary electron is very low, which is from 0 eV to 50 eV. Theory calculation of secondary electron emission has been studied. Besides these, existing methods used to suppress electron clouds have been introduced, such as modification of the vacuum chamber, beam parameters and low SEY of the surface materials. Finally, some examples of recent low SEY materials have been described.

Reference

[1] Austin L, Starke H. Ueber die Reflexion der Kathodenstrahlen und eine damit verbundene neue Erscheinung secundärer Emission. Annalen der Physik 1902;314:271-92.

[2] Balcon N, Payan D, Belhaj M, Tondu T, Inguimbert V. Secondary Electron Emission on Space Materials: Evaluation of the Total Secondary Electron Yield From Surface Potential Measurements. IEEE Transactions on Plasma Science 2012;40:282-90.

[3] Dionne GF. Origin of secondary-electron-emission yield-curve parameters. Journal of Applied Physics 1975;46:3347-51.

[4] Shih A, Yater J, Hor C, Abrams R. Secondary electron emission studies. Applied Surface Science 1997;111:251-8.

[5] Cazaux J. About the secondary electron yield and the sign of charging of electron irradiated insulators. European Physical Journal Applied Physics 2001;15:167-72.

[6] Bojko I, Hilleret N, Scheuerlein C. Influence of air exposures and thermal treatments on the secondary electron yield of copper. Journal of Vacuum Science & Technology A 2000;18:972-9.

[7] Hilleret N, Scheuerlein C, Taborelli M. The secondary-electron yield of air-exposed metal surfaces. Applied Physics A 2003;76:1085-91.

[8] Li W, ., Li DY. On the correlation between surface roughness and work function in copper. Journal of Chemical Physics 2005;122:954-.

[9] Eaton JR. Front Matter - Electrons, Neutrons and Protons in Engineering. Electrons Neutrons & Protons in Engineering 1966:iii.

[10] Spitzer A, Lüth H. The adsorption of oxygen on copper surfaces : I. Cu(100) and Cu(110). Surface Science Letters 1987;182:1–12.

[11] Kim JS, Cacialli F, Granström M, Friend RH, Johansson N, Salaneck WR, et al. Characterisation of the properties of surface-treated indium-tin oxide thin films. Synthetic Metals 1999;101:111-2.

[12] Cimino R. Surface related properties as an essential ingredient to e-cloud simulations. Nuclear Instruments and Methods in Physics Research Section A: Accelerators, Spectrometers, Detectors and Associated Equipment 2006;561:272-5.

[13] Grosso DR, Commisso M, Cimino R, Larciprete R, Flammini R, Wanzenberg R. Effect of the surface processing on the secondary electron yield of Al alloy samples. Physical Review Special Topics - Accelerators and Beams 2013;16:104-.

[14] Bruining H. Physics and applications of secondary electron emission: Pergamon Press; 1954.

[15] Dionne GF. Effects of secondary electron scattering on secondary emission yield curves. Journal of Applied Physics 1974;44:5361-4.

[16] A.Dekker. Solid State Physics. In: F. Seitz DT, editor. Advances in Research and Applications. Salt Lake City: Academic Press; 1958. p. 251-311.

[17] Suetsugu Y, Fukuma H, Wang L, Pivi M, Morishige A, Suzuki Y, et al. Demonstration of electron clearing effect by means of a clearing electrode in

high-intensity positron ring. Nuclear Instruments and Methods in Physics Research Section A: Accelerators, Spectrometers, Detectors and Associated Equipment 2009;598:372-8.

[18] Alesini D, Battisti A, Coiro O, Demma T, Guiducci S, Lollo V, et al. Design and Test of the Clearing Electrodes for e- cloud Mitigation in the e+ DAFNE Ring. Storage Ring 2013.

[19] Pivi M, Collet G, King F, Kirby R, Markiewicz T, Raubenheimer T, et al. Secondary electron yield and groove chamber tests in PEP-II. Particle Accelerator Conference, 2007 PAC IEEE2007. p. 1997-9.

[20] Fukuma H, Flanagan J, Hosoyama K, Ieiri T, Kawamoto T, Kubo T, et al. Status of Solenoid System to Suppress the Electron Cloud Effects at the KEKB. AIP Conference Proceedings 2002;642:357-9.

[21] Valizadeh R, Malyshev OB, Wang S, Zolotovskaya SA, Allan Gillespie W, Abdolvand A. Low secondary electron yield engineered surface for electron cloud mitigation. Applied Physics Letters 2014;105:231605.

[22] Wang L, Raubenheimer TO, Stupakov G. Suppression of secondary emission in a magnetic field using triangular and rectangular surfaces. Nuclear Instruments & Methods in Physics Research 2007;571:588-98.

[23] Ferreira MJ, Seraphim RM, Ramirez AJ, Tabacniks MH, Nascente PAP. Characterization and Evaluation of Ti-Zr-V Non-evaporable Getter Films Used in Vacuum Systems. Physics Procedia 2012;32:840-52.

[24] Kirby RE, King FK. Secondary electron emission yields from PEP-II accelerator materials ☆. Nuclear Instruments & Methods in Physics Research 2001;469:1-12.

[25] Hilleret N, Baglin V, Henrist B, Mercier E, Scheuerlein C. Ingredients for the understanding and the simulation of multipacting. 10th Workshop on LEP-SPS Performance. Chamonix, France2000. p. 130-5.

[26] Cimino R, ., Commisso M, ., Grosso DR, Demma T, ., Baglin V, ., Flammini R, ., et al. Nature of the decrease of the secondary-electron yield by electron bombardment and its energy dependence. Physical Review Letters 2012;56:112-8.

[27] Umezawa Y, Reilley CN. Effect of argon ion bombardment on metal complexes and oxides studied by x-ray photoelectron spectroscopy. Analytical Chemistry 1978;50:1290-5.

[28] Baglin V, J.Bojko, Gröbner O, Henrist B, Hilleret N, Scheuerlein C. The Secondary Electron Yield Of Technical Materials And Its Variation With Surface Treatments. EPAC 2000. Vienna, Austria2000. p. 217-21.

[29] Pimpec FL, King F, Kirby RE, Pivi M. Secondary Electron Yield Measurements of TiN Coating and TiZrV Getter Film. Physics - Accelerator Physics 2003.

[30] Pimpec FL, Kirby RE, King FK, Pivi M. The Effect of Gas Ion Bombardment on the Secondary Electron Yield of TiN, TiCN and TiZrV Coatings For Suppressing Collective Electron Effects in Storage Rings. Nuclear Instruments & Methods in Physics Research 2006;564:44–50.

[31] Henrist B, Hilleret N, Scheuerlein C, Taborelli M. The secondary electron yield of TiZr and TiZrV non-evaporable getter thin film coatings. Applied Surface Science 2001;172:95–102.

[32] Vallgren CY, Arduini G, Bauche J, Calatroni S, Chiggiato P, Cornelis K, et al. Amorphous Carbon Coatings for the Mitigation of Electron Cloud in the CERN SPS. Review of Modern Physics 2011;14.

[33] Pinto PC, Calatroni S, Neupert H, Letant-Delrieux D, Edwards P, Chiggiato P, et al. Carbon coatings with low secondary electron yield. Vacuum 2013;98:29-36.

[34] Henrist B, Hilleret N, Scheuerlein C, Taborelli M. The secondary electron yield of TiZr and TiZrV non-evaporable getter thin film coatings. Applied Surface Science 2001;172:95-102.

[35] Benvenuti C, Cazeneuve JM, Chiggiato P, Cicoira F, Santana AE, Johanek V, et al. A novel route to extreme vacua: the non-evaporable getter thin film coatings. Vacuum 1999;53:219-25.

[36] Benvenuti C, Chiggiato P, Costa Pinto P, Escudeiro Santana A, Hedley T, Mongelluzzo A, et al. Vacuum properties of TiZrV non-evaporable getter films. Vacuum 2001;60:57-65.

[37] Prodromides AE, Scheuerlein C, Taborelli M. Lowering the activation temperature of TiZrV non-evaporable getter films. Vacuum 2001;60:35-41.

[38] Vallgren CY, Calatroni S, Pinto PC, Kuzucan A, Neupert H, Taborelli M. Characterization of Carbon Coatings with Low Secondary Electron Yield. Vacuum 2011;98:29-36.

Chapter 3. Experiment methods and procedures

The experimental procedures of this PhD project include the following steps:

1. Sample preparation
2. SEY measurements
3. Surface analysis with available tools and techniques

Samples involved in this project include bulk metal samples, thin film coatings produced by physical vapour deposition (PVD), and nanosecond pulsed laser processed sample. After SEY measurements, these sample surfaces are analysed using scanning electron microscopy (SEM), X-ray diffraction (XRD) and X-ray Photoemission Spectroscopy (XPS). The samples also are processed by several surface treatments to reduce the SEY, which are electron conditioning and annealing under vacuum circumstance.

3.1 Sample preparation

The dimensions of all the bulk samples and coatings are about 12×12 mm^2. The studies of this project are from bulk samples to thin films and then to pulsed laser blackened samples. For example, the bulk samples are Cu, Al alloys, stainless steel and Ti, Zr, V and Hf foil. The coatings are ternary NEG coatings. Finally, the blackening copper, Al alloys, and stainless steel are produced by pulsed laser. The blackening samples are treated directly on the Cu, Al alloys and 316L stainless steel foils with a purity of 99.999% of 1 mm thickness.

3.1.1 Bulk samples

Ti, Zr, V and Hf foils were cut to 12×12 mm^2. The thicknesses of the Ti, V and Hf foils are 0.25 mm and Zr foil thickness is 0.5 mm. The purities of Ti, Zr, V and Hf foils are 99.6%, 99.2%, 99.8% and 97.0%, respectively.

3.1.2 Thin film coatings

DC magnetron sputtering is chosen because it is a well-known and convenient

way to produce thin films in a long straight beam pipe in the accelerator.

Magnetron sputtering is a method to deposit coatings on specific substrates with atoms removed from the target surface by energetic bombardment with ionized inert gases at high impact velocities. Magnetic sputtering happens in low vacuum environmental conditions [1]. The schematic layout of planar magnetron deposition is shown in **Figure 3-1**. A controlled flow of inert gas (Ar) is injected to a sufficient pressure to enable a magnetic glow discharge. A high negative voltage is applied to the target which attracts positive ions with high velocity. As a result, when the impact energy is greater than the binding energy of the lattice, the surface atoms on the target are removed and these deposit on the substrate. The electrons which are trapped by the magnetic field move in a helical path around the magnetic field lines. Thus, more ionizing collisions occur with the inert gases by the moving electrons, which produce more positive ions and increase plasma intensity.

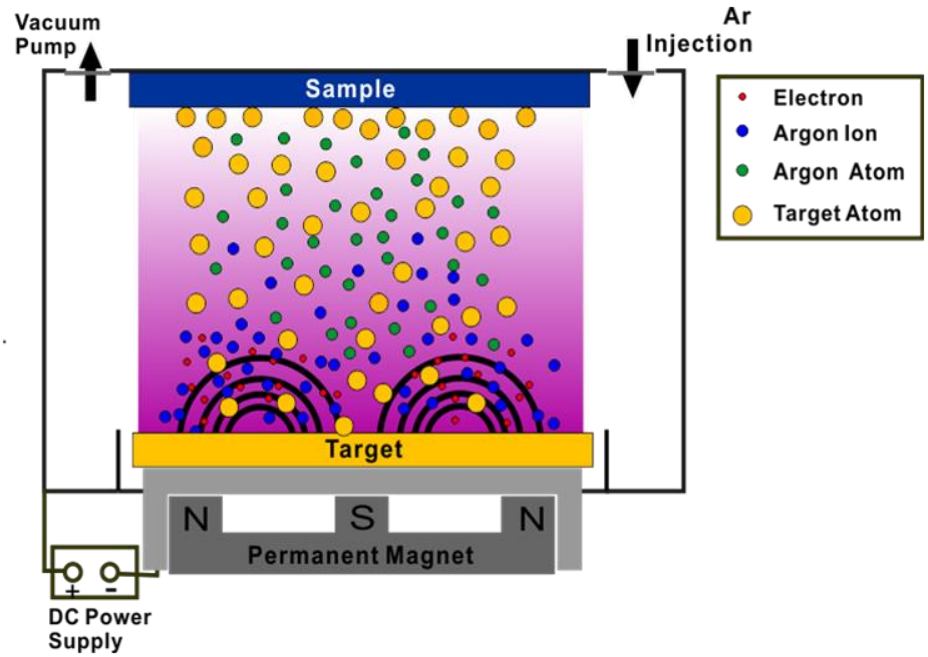

Figure 3-1 A schematic layout of the planar physical vapour deposition process.

The PVD facility used in the ASTeC vacuum laboratory is shown in **Figure 3-2.**

It consists of a load lock chamber at the top, a gate valve, a deposition chamber, equipped with four magnetron guns with different targets and a sample holder for six samples.

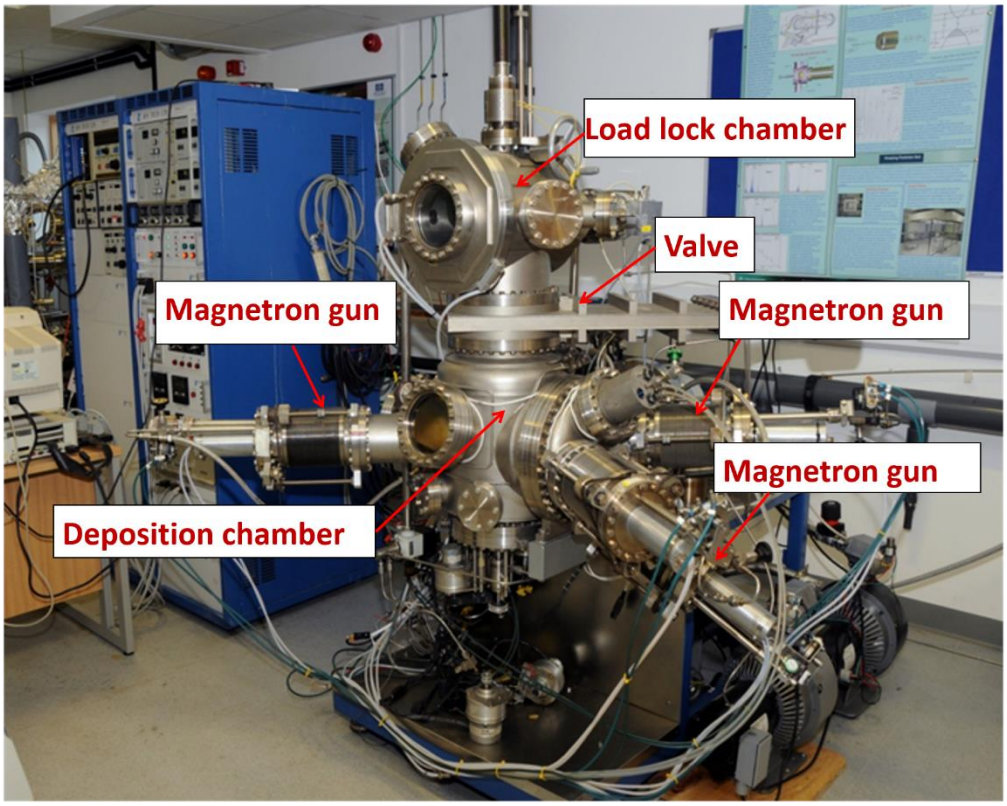

Figure 3-2 Planar physical vapor deposition facility at the ASTeC Vacuum Laboratory

(a) Sample preparation

The films were deposited by PVD onto stainless steel sample plate, silicon wafers and nanosecond pulsed laser treated copper. The dimensions of the substrates were 12 × 12 mm^2. The substrates were ultrasonically cleaned in acetone and then in isopropanol for 10 minutes.

(b) Deposition parameters

The system is unbaked and the typical base pressure of deposition chamber is around 4×10^{-8} mbar. The power is provided by pulsed DC power supply (Advanced Energy).The sputter inert gas is argon. The magnetron gun is cooled

by a chiller and the cooling water is maintained at 5 ^{o}C. The deposition process is usually decided by following parameters, such as different substrates, targets, gas pressures, powers and deposition time. Silicon, stainless steel sample plate and pulsed laser treated sample are used as the substrates for depositing the coatings. The coatings divide into two big categories, which are non evaporable getter (NEG) thin film and carbon coating. NEG thin films are composed of Ti, Zr and V which include ternary alloy coatings. The gas pressure is in the region of 5-8×10^{-3} mbar. The pulsed DC power supply delivers 300 W and the frequency is 350 kHz. The duration of deposition for all the samples was one hour.

3.1.3 Nanosecond pulsed laser treated metals

The metal surfaces modified by a nanosecond pulsed laser, lead to the formation of highly organised surface microstructures. This surface treatment reduced the SEY of basic chamber materials such as Cu, 316L stainless steel and Al, dramatically. In addition, the advantages of this technology also include: (1) low cost (process is carried out in an inert gas environment at atmospheric pressure); (2) no new material introduced (this surface treatment changes only the topography); (3) the surface is highly reproducible and provides a stable surface chemistry; (4) the surface is robust and is immune to any surface delamination (unlike thin film coating). As a result, this is a promising material to solve the electron multipacting in the modern particle accelerator.

Conditioned samples: These samples were degreased before the laser exposure. A Nd:YVO4 laser with maximum average power of 20 W at λ = 1064 nm (for processing Al and stainless steel foils) and 10 W at λ = 532 nm (for processing Cu foil) was utilized for irradiating the samples in an argon atmosphere or in air atmosphere at room temperature. The diameter of the laser beam focused spot on each target, between the points where the intensity has fallen to 1/e^2 of the central value, was measured to be 60 µm. The average laser fluences employed for processing copper, aluminum and stainless steel

should reach the abolition conditions of surfaces, which were 6.1, 6.8 and 3.6 J/cm^2 for single shot, respectively. The beam was raster-scanned over the surface of the targets in both the horizontal and vertical directions using a computer-controlled scanner system [2]. Hatch distance is the distance between the two laser scans. In this studies, the range of hatch distance is from 30 to 90 μm.

Thermal treated samples: There are three types of samples, which have been studied in this thesis. Type I structures on copper and steel are produced by irradiation at 532nm, 80 ns pulsed laser operating at 100 kHz in Ar or Air. The beam spot size on the target was 70 μm. Type II structures on copper are produced by irradiating at 532 m, 50 ns pulse laser operating at 100 kHz in Air. The beam spot size on the target was 70 μm. The beam was raster-scanned over the surface of the targets in only one direction. Type III structures on copper are produced by irradiation at 1064 nm, 30 ps pulse laser operating at 100 kHz in Air. The beam spot size on the target was 60 μm.

3.2 Characterization methods of surface coatings

The following surface facilities were used to analyse the samples.

- Secondary Electron Yield and XPS facility
- XRD
- SEM

SEY and XPS facility is a new built setup in the vacuum lab, ASTeC, which is used for SEY measurements and XPS analysis. XRD, which is for measuring the grain size of the surface, is also available in the vacuum lab. SEM was undertaken Manchester Metropolitan University.

3.2.1 Secondary electron yield measurement

The SEY measurements were carried out in a new, dedicated setup, which was designed and built by myself. A schematic SEY measurement chamber is shown in **Figure 3-3**. The SEY measurement chamber is equipped with an electron gun, a Faraday cup for collecting the emitted electrons and sample

holder. The sample holder is biased to -18 V. The Faraday cup and sample holder are connected to earth through two current meters.

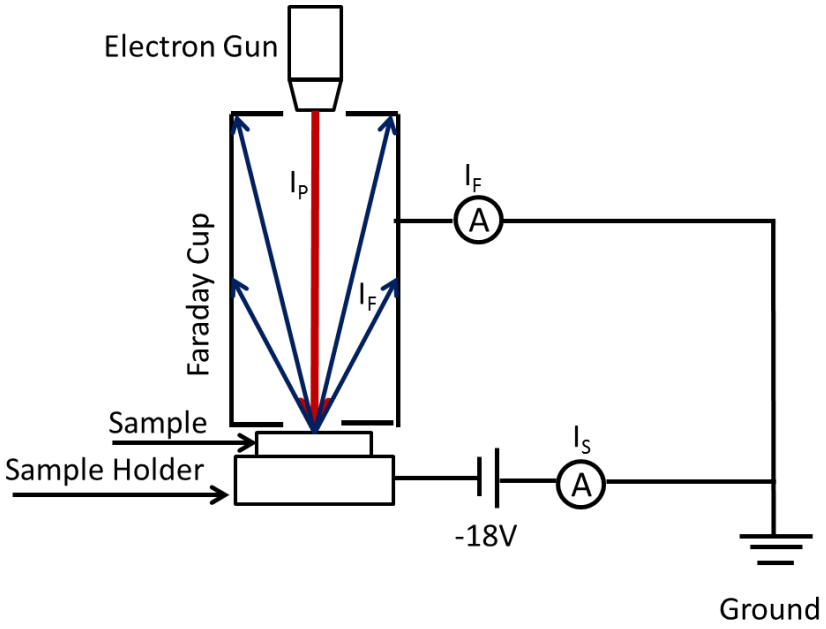

Figure 3-3 Schematic layout of the SEY apparatus

The SEY as a function of primary electron energy was measured over the range 80 to 1000 eV and at normal incidence. Measurements were performed using a Kimball electron gun (ELG-2/EGPS-2). The vacuum system is baked and the pressure in the test chamber was 2×10^{-10} mbar without electron bombardment and $2\text{-}5\times10^{-9}$ mbar during electron bombardment. The net current at the sample biased at –18 V and the Faraday cup at ground potential were measured with two current amplifiers (Keithley 6517A and Keithley 6485, accuracy ±0.01%). As the SEY is very sensitive to the electron dose, the total electron dose during the SEY measurements, as a function of primary energy, was not allowed to exceed 10^{-6} Cmm^{-2}. The accuracy of the SEY measurements was estimated to be within 1% for primary electron energies between 80 and 800 eV and about 6% for primary electron energies above 800 eV, as it will be explained in section 4.7.

The total SEY, δ, is defined as

$$\delta = \frac{I_S}{I_P} = \frac{I_F}{I_F + I_S} \qquad \text{Eq.(3-1)}$$

where I_S is the secondary electron current (including both elastic and inelastic processes) measured from the sample, and I_P is the primary beam current. I_F and I_s are the currents on the Faraday cup and the sample, respectively. The sum of the sample current I_s and the Faraday cup current I_F represents the primary energy current I_P. However, it must be noted that δ measured in this way includes not only true secondary electrons but also inelastically and elastically scattered electrons.

3.2.2 Scanning Electron Microscopy (SEM) measurement

Scanning electron microscopy (SEM) is a widely used technique in various areas like materials, physics, biology, etc. The schematic illustration of SE image recording in the SEM is shown in **Figure 3-4**. In SEM, after being generated by a biased filament the electron beam is then focused by electromagnetic lenses at the sample, where backscattered or secondary electrons are detected. Since backscattered electron (BE) emission is related to the atomic number of atoms within the sample surface, the BE emission image is used to map atomic distributions, with heavier atom being brighter in the image. Characteristic X-rays are unique to each element; therefore, they can be used to identify the chemical composition. Secondary electrons (SE) are very sensitive to surface morphologies like roughness, porosity, cracks, *etc*. As a result, the interpretation of SE images is of significance in revealing surface morphologies. However, it must be noted that separate detectors must be attached in the SEM chamber to identify electron or X-rays.

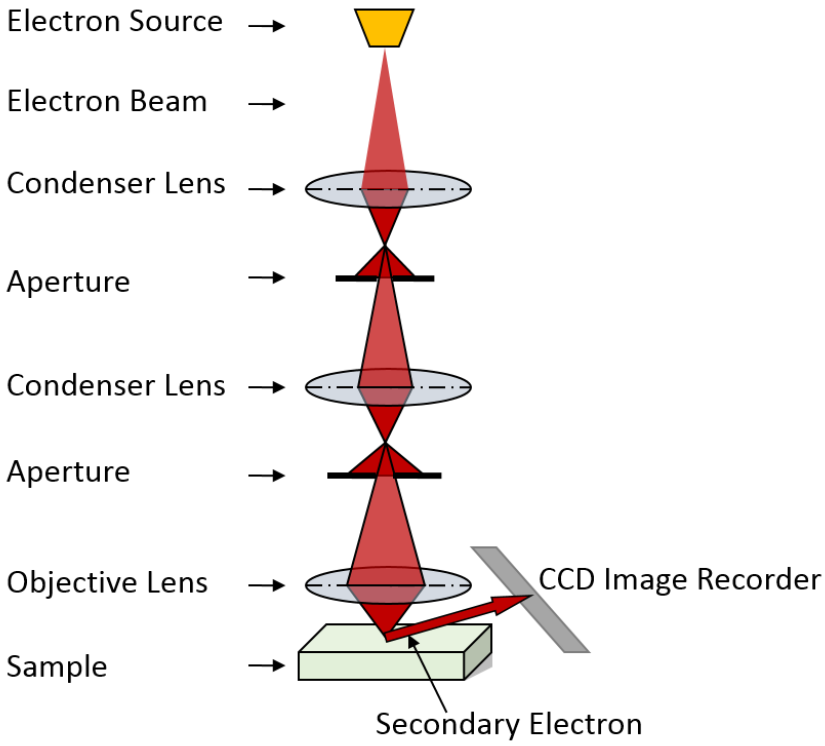

Figure 3-4 Schematic illustration of SEM layout and formation of a secondary electron image

3.2.3 X-ray photoelectron spectroscopy (XPS)

The surface chemical states were studied by XPS in this PhD project. When the surface is irradiated by monoenergetic soft X-rays, the energies of the detected electrons are analysed by electron energy analyser. Mg Kα (1253.6 eV) and Al Kα (1486.6 eV) X-rays are usually used. The physical principles behind XPS are illustrated in **Figure 3-5**, in XPS, incident X-rays with energy of h*v* hit the sample and interact with atoms in the surface. This causes inner shell electron emission by the photoelectric and Auger effect. Auger electrons may be emitted due to relaxation of the excited ions remaining after photoemission. The kinetic energy of the photo electrons, $E_{kinetic}$, is given by

$$E_{binding} = hv - (E_{kinetic} + \varphi) \qquad \text{Eq.(3-2)}$$

where hv is the energy of the photon, $E_{binding}$ is the binding energy and φ is the instrument work function.

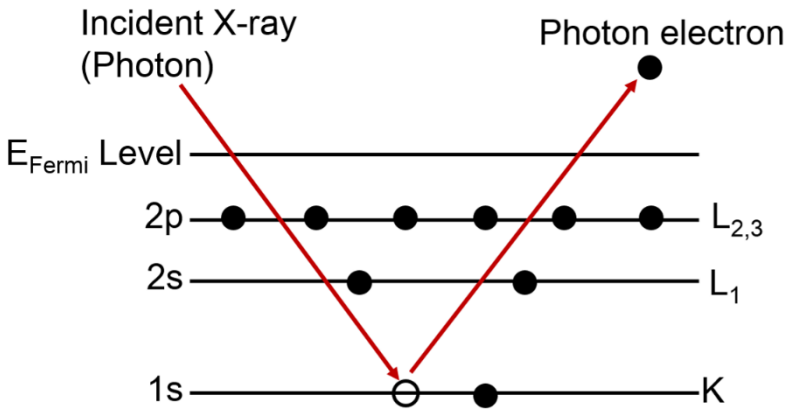

Figure 3-5 Schematic illustration on the principle of XPS

The electrons leaving the sample are detected by an electron spectrometer based on their kinetic energy. The analyzer is usually operated with an energy window related to the pass energy. This energy window may be a set of electrostatic and/or magnetic lens units. It collects a proportion of these emitted electrons that can be transferred through the apertures and focused onto the analyzer entrance slit. Electrostatic fields within the hemispherical analyzer (HSA) are established to only allow electrons of a given energy (pass energy (PE)) to arrive at the detector slits and onto the detectors themselves [3]. To maintain a constant energy resolution, the pass energy is fixed. [4].

Because a set of binding energies are unique to each element, XPS can be used to identify and determine the concentration of the elements within the escape depth of the photoelectrons in the surface. Difference in the chemical potential causes variations in the elemental binding energies (the chemical shifts). As a result, these chemical shifts can be used to identify the chemical state of the materials [4].

In my experiment, the spectrometer was operated at 20 eV pass energy for all samples. The angle between the X-ray source and electron analyser is 70 degree. Photo-electrons are excited by non-monochromated Al Kα X-ray source (hv=1486.6 eV) using VG twin anode. The Al anode was operated at 10 keV and source current is 20 mA. The base pressure during operating the XPS

is about 10^{-9} mbar pumped by 340 l/s turbomolecular pump (Leybold 340M).

3.2.4 X-Ray Diffraction (XRD)

XPS identified the chemical composition but it does not provide any indication of the crystallinity of the coating. XRD provides a solution to this drawback. In materials science, the XRD method is used to identify the phase composition, crystal structure, crystal size as well as residual stress. The basics of this technique rely on the fact that crystals have a periodic arrangement of atoms. When the incident X-ray beam, an electromagnetic wave, interacts with a crystal, it will be reflected by the atomic planes, as shown in **Figure 3-6**. When the reflected beams are in phase, they will interfere constructively. The relationship between the crystal plane spacing, the wavelength of the incident X-rays and the incident angle follows Bragg's Law:

$$2dsin\theta = n\lambda \qquad \text{Eq.(3-3)}$$

Where d is the crystal plane spacing, θ is the incident angle and λ is the X-ray wavelength.

The reflected X-rays only constructively interfere at some specific incident angles. So, it is easy to identify crystalline phase parameters in a material by interpretation of the X-ray diffraction peak. In addition, the relative intensities of the XRD peaks from different crystalline phases are proportional to the concentration. Therefore, XRD can be used to determine the crystalline composition and concentration within a material.

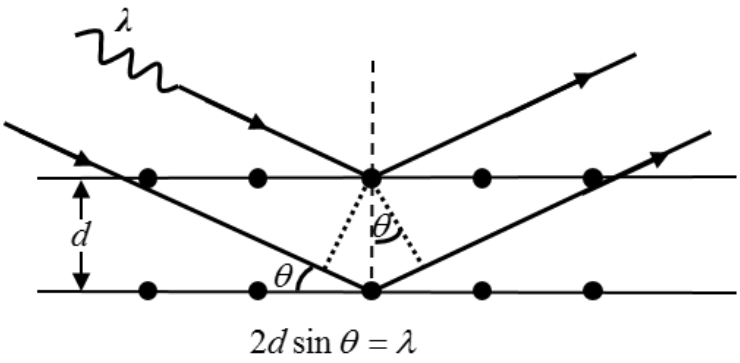

Figure 3-6 Schematic illustration of the XRD principle (the black dots represent atoms).

Experimental procedure

Bulk sample

The experiment was performed in a XRD machine (BRUKER PHASER D2) with CuKα radiation (1.54184 nm), and a 2θ scanning range of 10-100°.The scanning step was 0.01°. The obtained XRD patterns were analysed using EVA software from the Bruker Company.

Grain size calculation

Grain size is calculated by Sherrer's Function:

$$D = \frac{k\lambda}{Bcos\theta} \qquad \text{Eq(3-4)}$$

Where k is constant 1, B is the FWHM, θ is the peak position and λ is the wavelength of X-ray (λ=0.154056 nm).

3.3 Surface treatments of the SEY

The typical surface treatments are the ways to reduce the secondary electron yield of the vacuum chamber, such as conditioning by electron beam, thermal treatments under vacuum and ion bombardments. In this section, all the surface treatment methods involved will be introduced.

3.3.1 Electron irradiation method

The experiments were carried out with a flood gun installed in the surface treatment and analysis chamber. Flood gun is an electromechanical device that provides a steady flow of low-energy electrons to a desired target. It provides stable electron irradiations at the fixed energy onto the samples. The sample held on the manipulator is rotatable in order to change the directions with respect to the guns. Normal incidence is chosen for the electron irradiation experiments. The spot of the flood gun is about 137 mm^2, which is used to calculate the electron dose. The sample is battery biased to +18V when performing the electron irradiation. The energy of the flood gun is about 485 eV and electron dose is controlled by the irradiation time. The sample is cleaned by immersing in acetone and then in isopropanol for 10 minutes. Before the measurements, the samples remained few minutes in air after the cleaning for drying. Both the SEY measurements and XPS spectra were acquired before and after the electron conditioning in order to compare the reduction of the SEY and the changes of the surface compositions.

3.3.2 In-situ thermal treatment method

The samples were heated in the surface treatment and analysis chamber by radiation heating. The heater is inside the sample holder and operated by a power supply (CPX200, DUAL 35V, 10A, PSU). The temperature was measured on the sample plate by a K-type thermocouple and a temperature monitor (RS, 258-186). Both the SEY measurements and XPS spectra were acquired before and after the thermal treatments in order to compare the reduction of the SEY and the changes of the surface compositions.

3.4 Conclusions

Experiment methods and procedures used in this thesis have been described in the chapter. Samples involved include bulk metal samples, thin films and

nanosecond pulsed laser processed samples. The dimension of all samples is about 12 × 12 mm^2. Thin films are deposited by PVD on stainless steel, Silicon and laser treated samples. Nanosecond pulsed laser treated surface is a new technology to lower the SEY. The advantages include low cost, no new material introduced, highly reproducible and stable surface and so on. SEY measurements have been done on all the samples along with XRD, SEM and XPS analysis. The surface treatments are used to reduce the SEY, such as electron irradiation and thermal treatment.

References

[1] P. Kelly, R. Arnell, Vacuum, 56 (2000) 159-172.

[2] R. Valizadeh, O.B. Malyshev, S. Wang, S.A. Zolotovskaya, W. Allan Gillespie, A. Abdolvand, Applied Physics Letters, 105 (2014) 231605.

[3] http://www.casaxps.com/help_manual/XPSInformation/XPSInstr.htm

[4] J.F. Moulder, J. Chastain, R.C. King, Handbook of X-ray photoelectron spectroscopy: a reference book of standard spectra for identification and interpretation of XPS data, Perkin-Elmer Eden Prairie, MN, 1992.

Chapter 4. The SEY measuring facility

The SEY measurement is the key to the work reported here. Design and construction of a SEY measurement setup took most of a year. Each part of this setup is built in four steps, which includes design, materials selection, assembly and test before the practical SEY measurements. The SEY measuring facility consist of three chambers as shown in **Figure 4-1**: a load-lock chamber, the SEY measurement chamber, surface treatment and analysis chamber. After locating the sample into the load lock chamber, it is transferred into measurement chamber. SEY of the sample on the rotary and linear drive is measured using the kimball electron gun. The currents flowing through the Faraday cup and sample holder are recorded for the SEY measurement. Since surface condition is an important factor influencing SEY, it is necessary to measure the difference of surface composition and chemical bonding between atomically cleaned sample and as received sample. The surface measurement and analysis chamber hosts an X-ray gun, electron energy analyser, heatable sample holder, flood electron and argon ion gun. Surface conditioning, argon ion bombardments and thermal treatment also can be performed on the sample.

4.1 Load Lock Chamber

A load-lock chamber is required for loading the sample to SEY measurement chamber and surface analysis chamber and pumping the samples without exposing the other parts of the facility to air. This is achieved by a 110 mm long linear and rotary motion transfer arm with a transfer head mounted on the end. The transfer arm is a magnetically coupled sample transfer drive manufactured by Kurt J Lesker. The transfer head, manufactured by Omicron, is shaped so that it can hold the sample plate by clicking into place, and is shown in **Figure 4-2**. The sample will be released by rotating the transfer 180 degrees and locked again by keeping rotating another 180 degrees.

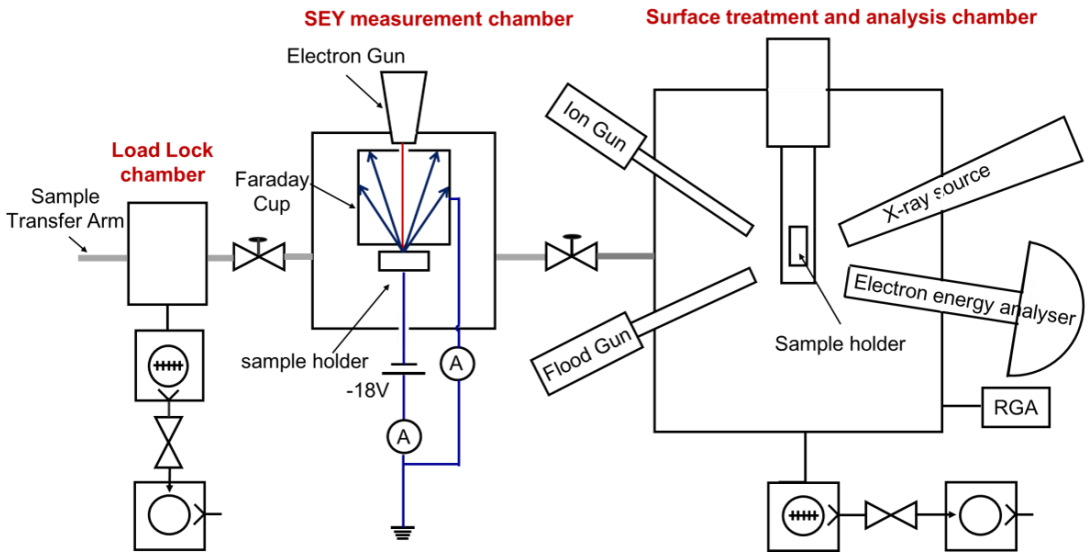

Figure 4-1 A layout of the SEY measuring facility

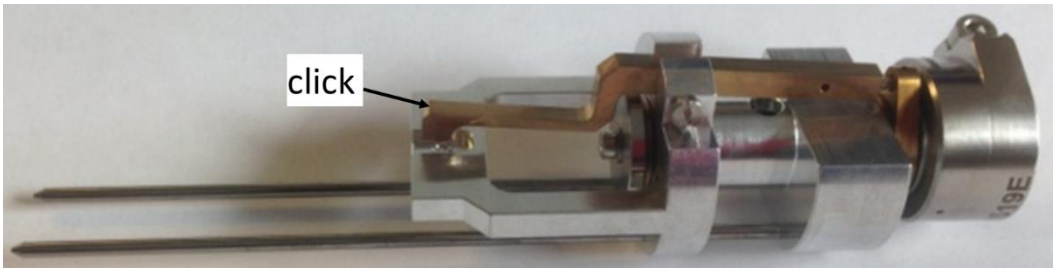

Figure 4-2 The transfer head

A 210 l/s turbomolecular pump (TMU 261, PFEIFFER Vaccum) and MKS pirani are installed in the chamber. The pressure of 2.4×10^{-9} mbar is routinely reached after overnight pumping from atmosphere.

4.2 Measurement Chamber

The SEY measurement chamber is equipped with an extractor gauge and NexTorr-D100 pump which maintains a base pressure of 2×10^{-10} mbar in the test chamber without electron bombardment and $2\text{-}5\times10^{-9}$ mbar during electron bombardment. The SEY chamber also includes the Kimball electron gun (ELG-2/EGPS-2), the Faraday cup, and the sample holder on the linear rotary drive.

The Faraday cup is for collecting electron currents. It is shown in **Figure 4-1**. It is composed of an 85 mm long 304L stainless steel cylinder with 50 mm

diameter and two 304L stainless steel plates on the top and bottom. Each cover plate has a hole in the centre which is for passing the beam. The diameters of the two holes are dictated by the beam size. The diameters of spots vary between 3 and 6 with the primary electron energies between 80 and 1000 eV. The diameter of top primary electron inlet hole is about 8 mm, and the bottom hole (sample side) is about 10 mm diam. These three parts are welded together. SEY is defined by the currents on the Faraday cup and the sample holder. The feedthroughs carry currents from the Faraday cup and sample holder into two Keithley pico-ammeters (Keithley 6517A and Keithley 6485, accuracy ±0.01%).

4.3 Surface Treatment and Analysis Chamber

The surface treatment and analysis chamber allows the performance of XPS analysis of the sample, electron bombardment with a flood gun (AG 31F, VG) with energy of 485 eV and ion etching with Ar^+ gun (PSP, ISIS 3000) with energy of 1.5 keV. Residual gas analysis (RGA, VG Thermo, VGQ) is also included in this chamber in order to check the residual gas in the chamber. The radiation heater is under the sample and inside the sample holder which is made by omicron. Radiant heating is a method for heating samples, which transfer radiant energy from an emitting heat source to an object. The hot filament in the radiation heater heats the sample by transferring radiant energy to the sample. XPS measurements are carried out with a spectrometer fitted with a five channeltron detector. Power supplies are, for the spectrometer a PSP Resolve Control, and for the detectors a PSP # 705. The spectrometer was operated at 20 eV pass energy at all times. The angle between the X-ray source and electron analyser is 70°. Photo-electrons are excited by non-monochromatic Al Kα X-ray source (hv=1486.6 eV) using VG twin anode, the Al anode used at all times operated at 10 keV, 20 mA. The base pressure in the surface treatment and analysis chamber is about 10^{-9} mbar pumped by 340 l/s turbomolecular pump (Leybold 340M).

4.4 Beam Profile Measurements

The primary electron beam is one of the most important parameters in the SEY measurements. Before the SEY measurements, the beam profile of the Kimball electron gun needed to be studied. The aim is to deliver roughly same spot size at different energies and also to make sure that the spot can go through the holes at the top and bottom of the Faraday cup instead of hitting the Faraday cup. The beam sizes at different energies are received by controlling the focus and anode of Kimball electron gun. In this experiment, the beam profile has been measured in two ways, which are using a phosphor screen and a wire scanner, respectively.

4.4.1 Phosphor Screen Methods

The beam profile of high energies has been achieved using P15 phosphor on ITO glass in order to calculate the size, the position and the shape of the spot. However, energies below 200 eV are too weak to show on the phosphor screen, so only the energies from 1000 to 200 eV have been measured using phosphor screen method. The phosphor is located on the sample holder. The electron gun is mounted on the middle port of the flange which is perpendicular to the phosphor screen and the camera is mounted on the side port, shown in **Figure 4-3**. The distance between the bottom of the Kimball electron gun and the phosphor is varied by linear and rotary drive. As the length of the Faraday cup is 85 mm, the distances we chose are 85, 55, 20 and 12 mm, respectively. 12 mm is the closest distance which can be seen from the camera. The energies of electron gun vary from 200 to 1000 eV by a step of 50 eV.

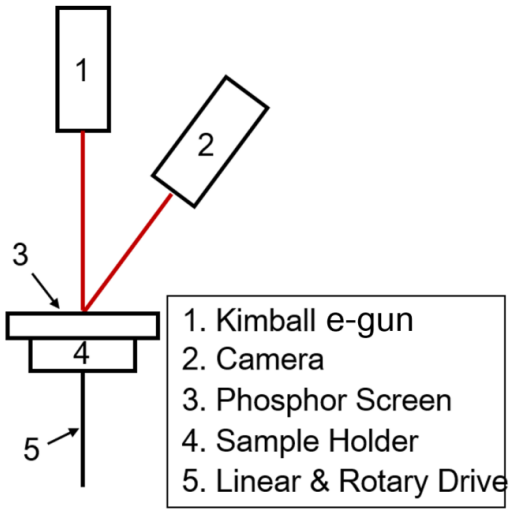

Figure 4-3 A layout of beam profile measurements by phosphor screen method

The results shown in **Figure 4-4** are the beam spots at the position of 85 mm at 1000, 700, 450 and 200 eV, seperately. The round green spots shown on the phosphor are the beam spots and the radiuses of the spots are almost 3 mm.

The centres of the spots are much brighter than the outside which is consistent with a Gaussian profile. This phenomenon is more obvious at low energies than high energies. **Figure 4-5** shows that the trend of the spot sizes with all energies varies with the distance between the bottom of the electron gun and the phosphor screen. It is clearly shown that the spots of different energies keep almost the same size at the same distance. A large difference in spot size appears at 20 mm; the radius of spot decreases from 3 mm at 85 mm to the minimum at 20 mm and then increases again. However, simple extrapolation indicates that the radius should not be over 2 mm below 12 mm from the trend of the curve.

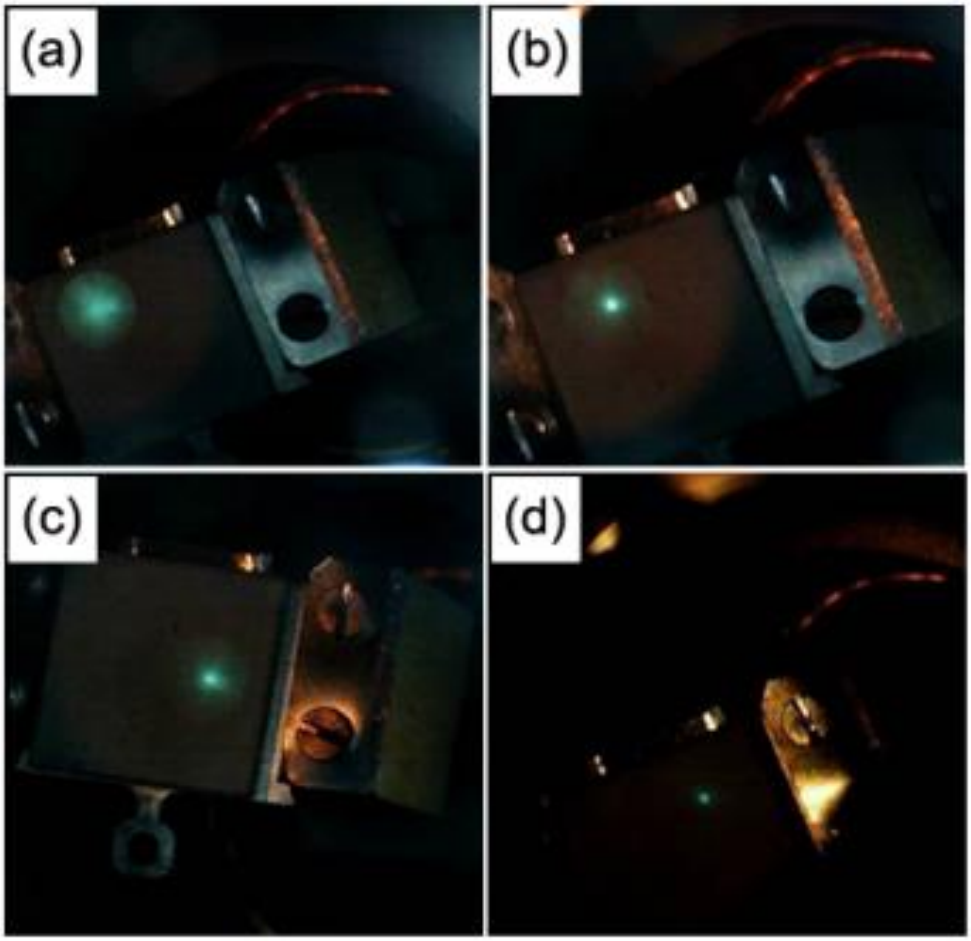

Figure 4-4 Electron beam spot pictures on phosphor screen (12×12 mm^2) at the distance of 85 mm for different energies: (a) 1000 eV, (b) 700 eV, (c) 450 eV, (d) 200 eV

In conclusion, the diameter of spot is about 6 mm at the bottom position of Faraday cup and not over 4 mm at the top position of Faraday cup. The bottom and top apertures of Faraday cup are 10 mm and 8 mm, respectively. As a result, the beam when focused will go through the top and bottom apertures of the Faraday cup.

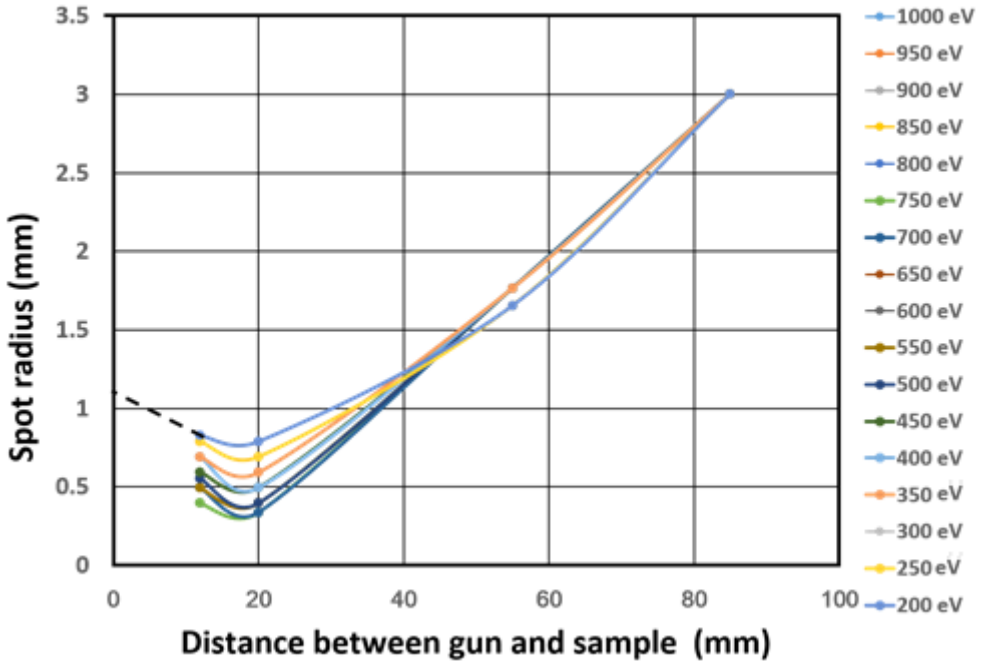

Figure 4-5 The spot radiuses at different energies vs distance between gun and sample

4.4.2 Wire Scanner Methods

The beam profile for low energies (from 80 to 200 eV) has been measured by wire scanner. In this experiment, the wire scanner is used to determine the low energy beam sizes and the alignment of the beam. As there is a linear translation device at the end of the electron gun, the position of the gun can move slightly between in the air and in the vacuum. So the beam path can be moved slightly to make sure the beam passes through the aperture of the Faraday cup without hitting it. The beam patterns follow the Gaussian function. As a result, we use the full width half maximum (FWHM) to describe the beam size.

The wire scanner, displayed in **Figure 4-6**, is used for measuring the beam spots by collecting the currents from the electron gun. Wire scanner is made of 'U' aluminium alloys plate, aluminium alloys rod and three 0.25 mm diameter stainless steel wires (Fe/Cr18/Ni8/Mo3, Goodfellow). The wire distribution is also shown in **Figure 4-6**, which are two cross wires (Wire 1 and Wire 2) and

one level wire in front (Wire 3). The end of the aluminium alloy rod is fixed on a 4-way feedthrough. The whole wire scanner is moved by a linear translation drive. A 150 mm long ruler is glued on the sample drive. Each experiment is achieved by two sequences of measurements, which starts from the ruler position of 150 mm, ends at 90 mm and then come back from 90 to 150 mm. Each point is collected at every 2 mm. The currents were recorded by two current amplifiers (Keithley 6517A and Keithley 6485). The sample holder is placed at the lowest position in the chamber and biased with positive 200 V (power supply SM 400-AR-4, Delta elektronika). The aim is to decrease the secondary electron coming from the sample holder and reduce the noise influence to the scanning. However, there is some limitation of this wire scanning design. Firstly, the cross point of wire scanner assembly does not mount in the centre. It is on the left hand side from the opposite window port. Secondly, the wire scanner is not just under the bottom Faraday cup. The distance between the bottom Faraday cup and the scanner plate is approximately 3 cm. Thirdly, the secondary electrons coming from the aluminium alloys plate can be collected by the three wires. Fourthly, the wire scanner measures the total currents on the wires instead of single point. As a result, the diameters of the spots we received include the spot shape. So they are bigger than the actual spot diameters.

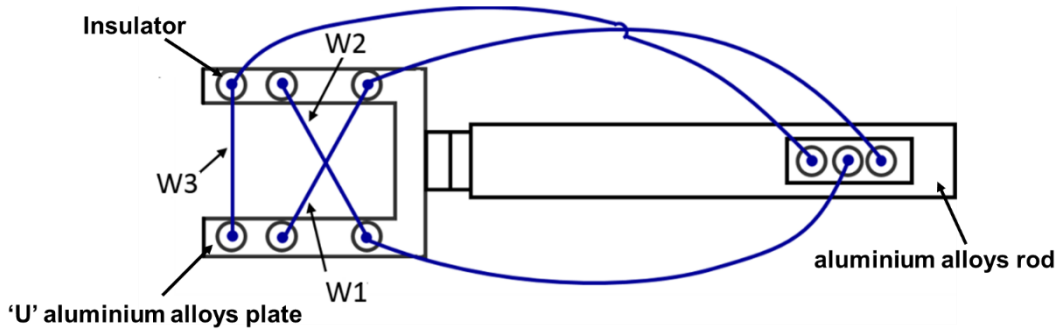

Figure 4-6 A layout of the wire scanner

The beam profile at 200 eV is shown in **Figure 4-7**; I1, I2 and I3 stand for currents on the wire 1, wire 2 and wire 3, respectively. As the beam scanner

plate is not in the centre, there is no overlap between I1 and I2, so it hits wire 2 firstly and then wire 1. The current intensities of these three wires have about 20 nA differences. The FWHM of I1, I2 and I3 are 3, 2.7 and 2 mm, respectively.

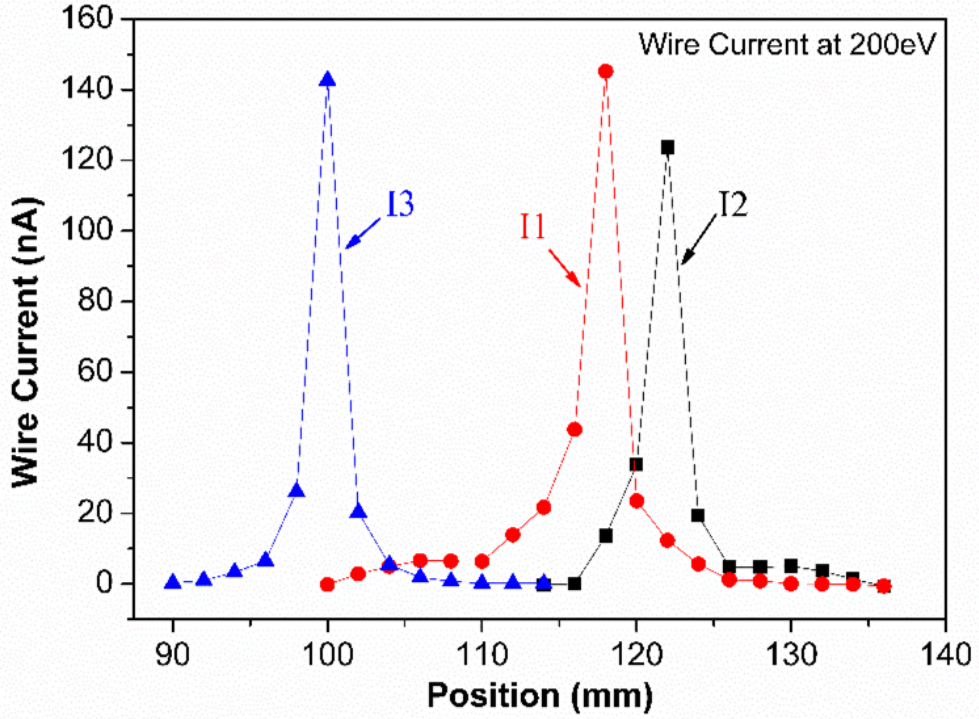

Figure 4-7 Beam profile of 200 eV electron energy beam.

The position of the Faraday cup aperture needs to be confirmed at the scanner plate level. Three directions of aperture dimension are obtained by defocussing the beam. We chose to defocus 1000 eV electron energy beam to make sure the bottom Faraday cup aperture. All the focus peaks with different energies should be in the range of the aperture. The beam profile of three wires for all the energies and the aperture range are shown from **Figure 4-8** to **Figure 4-10.**

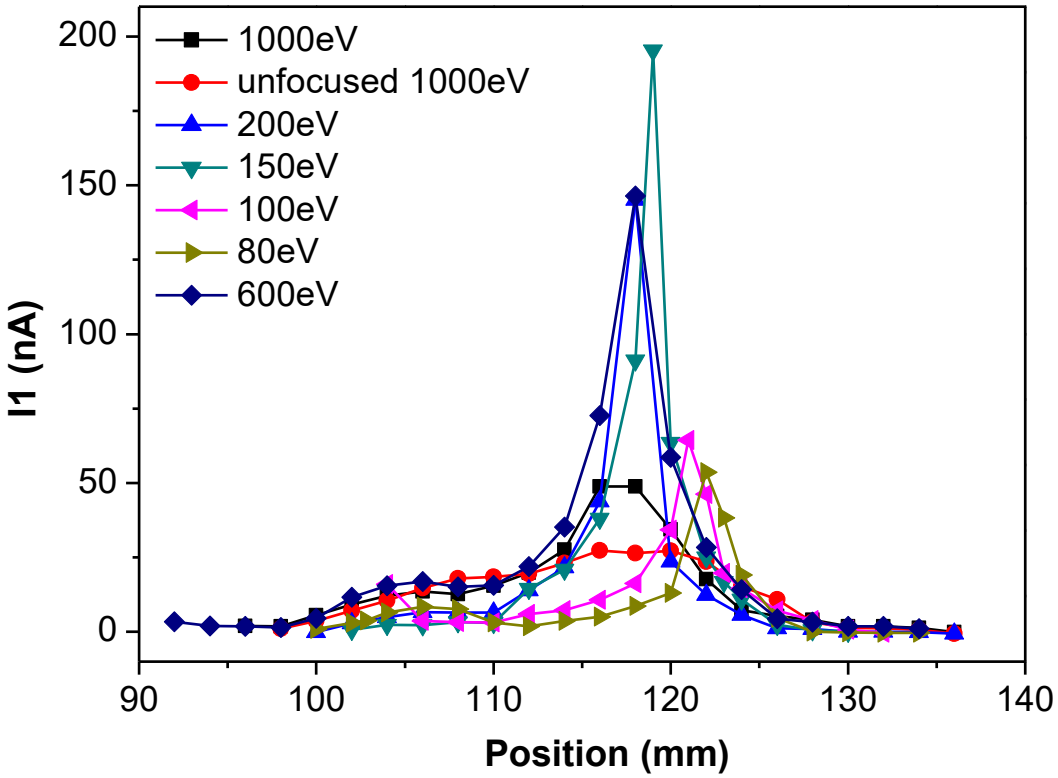

Figure 4-8 Beam profile of I1 on the wire 1.

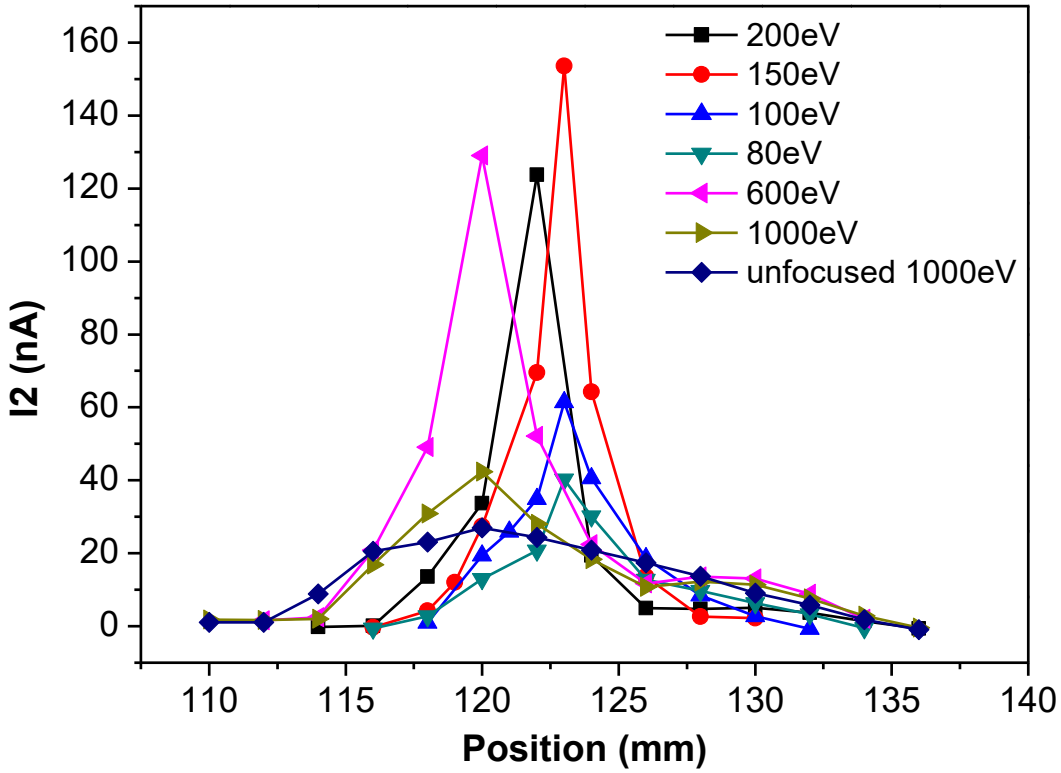

Figure 4-9 beam profile of I2 on the wire 2.

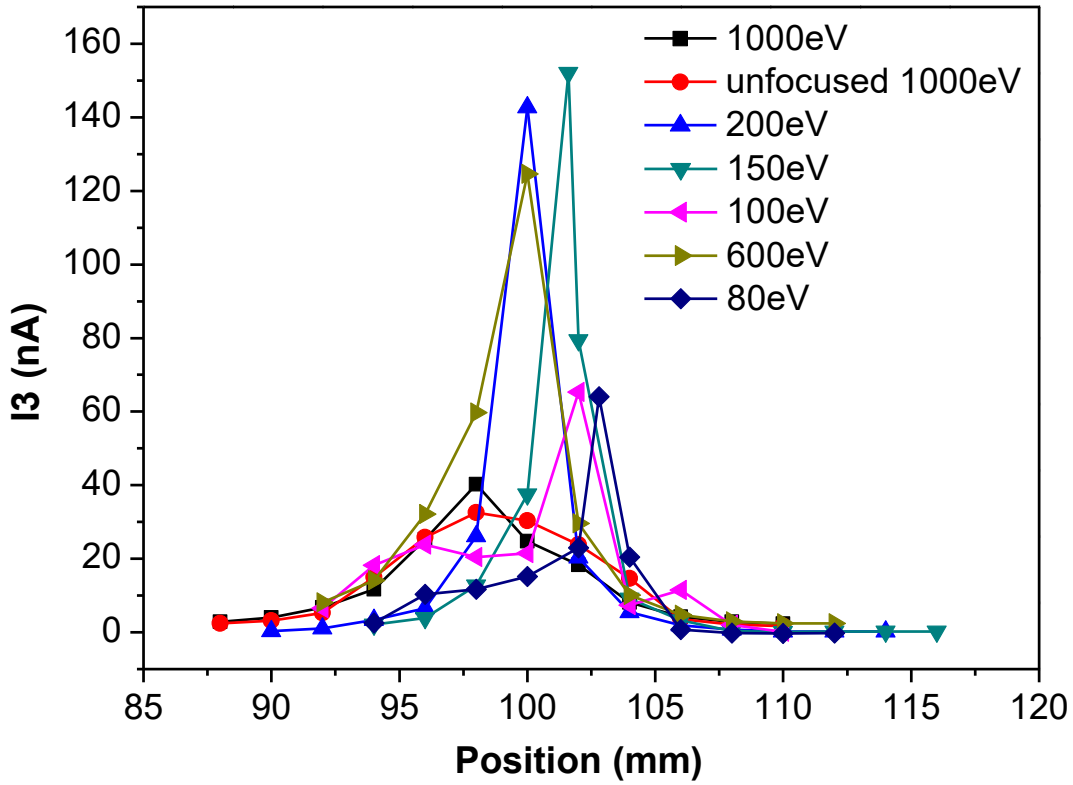

Figure 4-10 Beam profile of I3 on the wire 3.

From all above three figures, the thick black peaks, which stand for the unfocused beam, are used to confirm the Faraday cup aperture. Unfocused beam can go through the whole aperture. So this can be used to make sure the aperture size at the Faraday cup level. The unfocused peak is the widest, lowest compared to other focused peaks. All the focused peaks are inside the unfocused peak. The other obvious phenomenon is that low energy beams are moving. The beam spots below 200 eV begin to shift to one side. The beam with 80 eV is already at the edge of the bottom Faraday cup aperture.

The bottom Faraday cup aperture size and the FWHM of different energy beams for Wire 1, Wire 2 and Wire 3 are shown by **Figure 4-11** to **Figure 4-14.** As FWHM is regarded as the beam size, they clearly prove that all the beam spots are inside the hole of the bottom Faraday cup. The spots started moving from 150 eV, most likely due to earth magnetic fields. At the energy of 80 eV the beam is almost at the edge. Although the beam deflection influences the shape of the beam, it has been used when focusing energy of 100 and 80 eV.

Otherwise, the spots of these two energies will hit the Faraday cup. In order to keep the round shape, the deflection is only used to move the spot into the aperture. It is also shown that the spot size is becoming smaller from 1000 to 150 eV. These results match with the results obtained using the phosphor screen. 150 eV is the energy with the smallest spot; however, the beam spots get bigger below 150 eV.

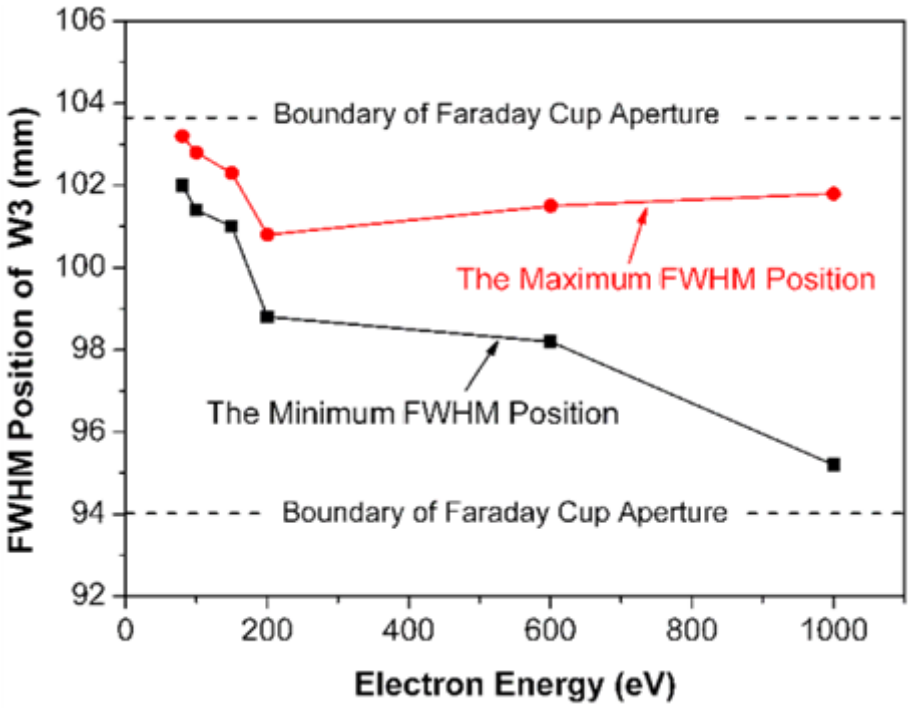

Figure 4-11 The Faraday cup aperture and FWHM positions for Wire 1 at primary electron energies between 80 and 1000 eV.

In conclusion, the beam profile measurement is used to understand the beam of the electron gun and make sure the beam hits on the sample instead of on the Faraday cup in order to reduce the experiment error. All the settings of focus and anode for the gun are suitable to do the secondary electron yield measurement depending on images obtained from the phosphor screen and results achieved from the wire scanner.

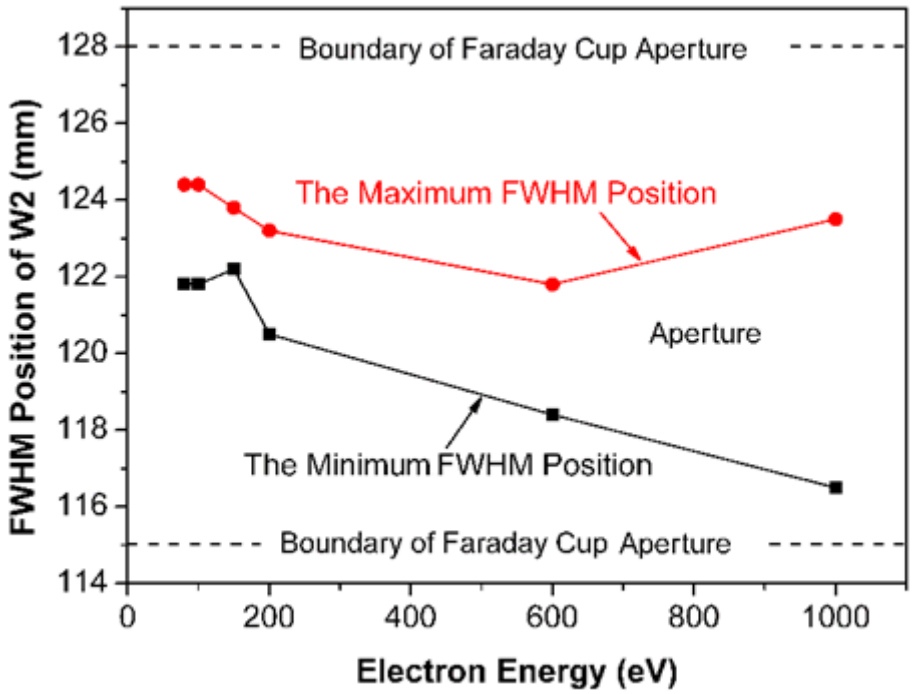

Figure 4-12 The Faraday cup aperture and FWHM positions for Wire 2 at primary electron energies between 80 and 1000 eV.

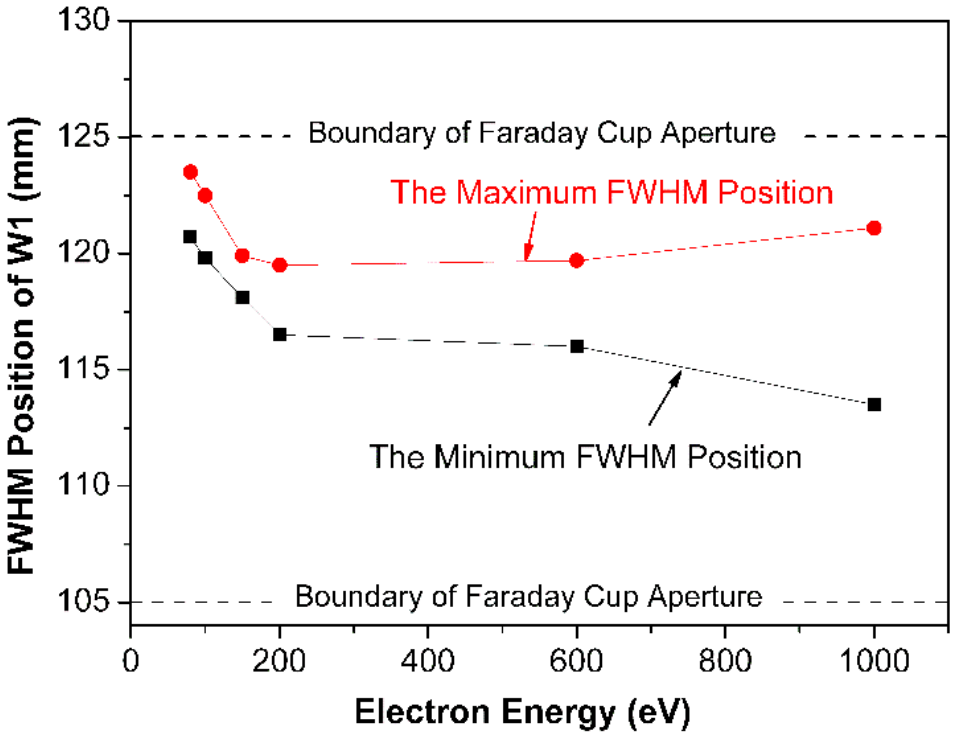

Figure 4-13 The Faraday cup aperture and FWHM positions for Wire 3 at primary electron energies between 80 and 1000 eV.

4.5 Secondary Electron Yield Measurement

The SEY measurements were carried out as a function of primary electron energy from the range 80 to 1000 eV at normal incidence. The total SEY, δ, is defined by Eq.(3-1).

As the SEY is very sensitive to the electron dose, the total electron dose during the SEY measurements, as a function of primary energy, was not allowed to exceed 10^{-6} C·mm^{-2}. The pressure in the test chamber was 2-3×10^{-10} mbar without electron bombardment and 2-5×10^{-9} mbar during electron bombardment. The filament current was 1.36 μA and the diameter of spot was smaller than 10 mm at the target. The Faraday-to-ground current I_F and sample-to-ground current I_S are measured by two current amplifiers (Keithley 6517A and Keithley 6485, accuracy ±0.01%).

4.6 Study of the Biasing Effect

The SEY measurement is a function of primary electron energy and the ratio of secondary electron currents and primary currents. The sample is usually biased to negative voltages in order to repel most secondary electrons, whereas the faraday cup is usually biased to positive voltages in order to capture all secondary electrons emitted from the sample. In this section, the biasing effect will be studied through comparison between bias measurements and non-bias measurements. The sample is battery biased by -18 V. Faraday cup is biased to +20 and +40V, separately by power supply (SM 400-AR-4, Delta elektronika).

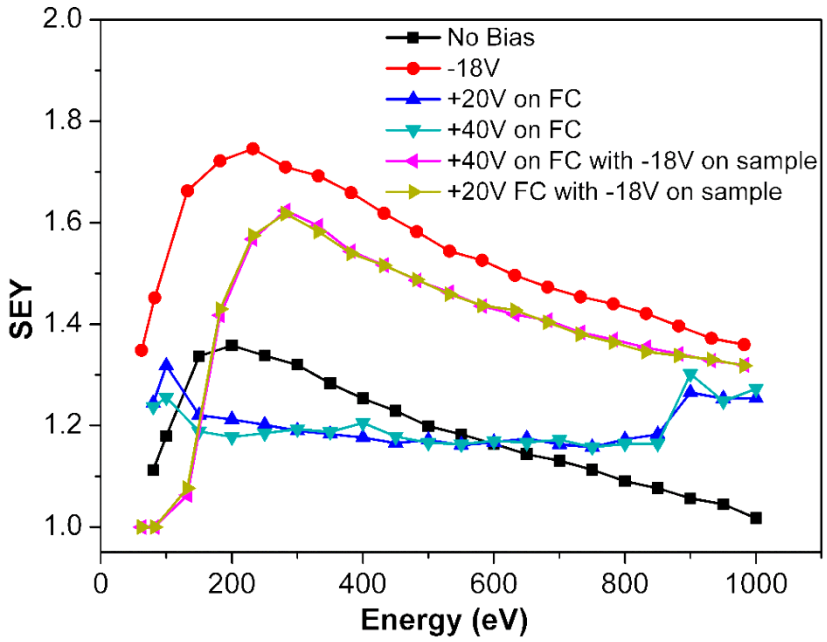

Figure 4-14 The study of biasing effect on copper sample

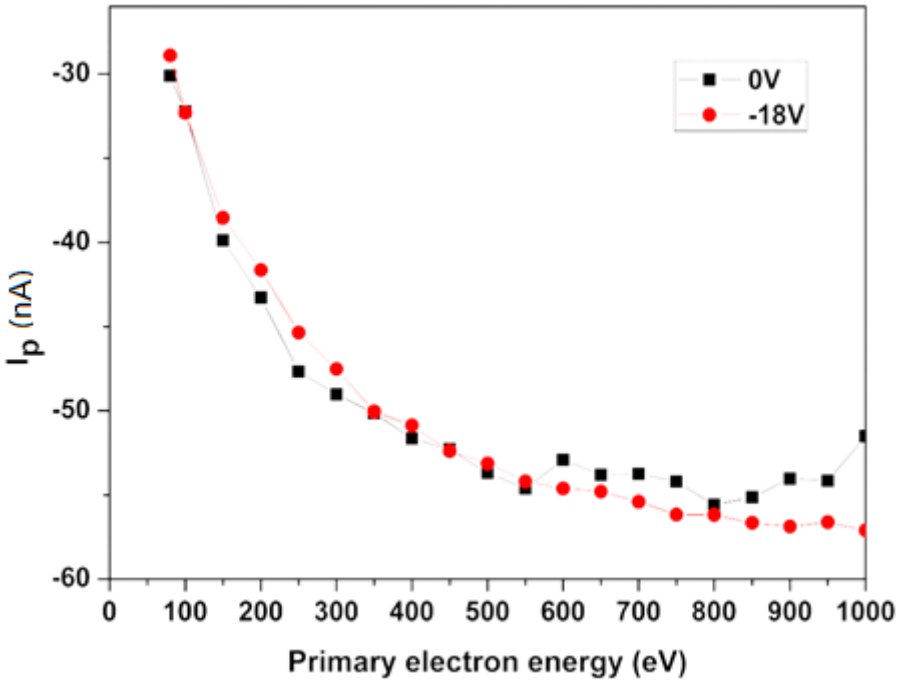

Figure 4-15 Primary electron currents of all energies by different negative bias on Cu sample.

Several experiments studied the biasing effect on a copper sample and the results are shown in **Figure 4-14**. The measured SEY of copper here is only 1.38 without any bias, which is much lower than the reference value (about 2)

[1]. However, after the sample has been biased negative 18 V, the SEY of copper increases to 1.78, which is similar to Cu SEY results. **Figure 4-15** exhibits the total primary electron current of all energy scans without any bias on the sample or -18 V on the sample. The results show the primary electron currents are roughly the same for both non-bias and bias experiments. Comparing the results from **Figure 4-14**, more secondary electrons coming from the sample hit on the Faraday cup with negative voltages on the sample. As a result, for the future SEY measurements, the negative bias will be used on the sample to repel more secondary electrons from the sample to the Faraday cup in order to obtain more accurate results.

The remaining four groups of experiments in **Figure 4-14** illustrate the influence of positive bias on the Faraday cup on secondary electron yield. As a positive potential is put on the Faraday cup, the beam path will deviate if the beam is not in the centre. Then the beam will hit the Faraday cup instead of on the sample. The expected influence of positive bias on the Faraday cup is demonstrated in **Figure 4-14**, the SEY is almost a horizontal line from 1000 to 80 eV with only positive bias on the Faraday cup. So due to deviation of the beam path, at all energies, most electrons hit the Faraday cup and only a part of electrons hit the sample. There is not much difference between +20 and +40 V.

Finally, we put both positive bias on the Faraday cup and negative bias on the sample, and secondary emission went down to almost zero when primary electron energy is lower than 200 eV. From the above beam profile measurements, the beam below 200 eV obviously shifts to the edge. So the positive biases influence the beam shift at low primary energies more than that at high primary energies. Most of low energy beam hits on the Faraday cup. The secondary electron yield at low energies cannot be measured with positive bias of the Faraday cup. However, the SEYs at high primary electron energies

are much lower than that with only negative bias on the sample. So the primary beams at high energies are also influenced by the positive bias and arrive on the Faraday cup instead of the sample. As a result, for the future secondary electron yield measurement, we choose to only bias the sample with negative voltage.

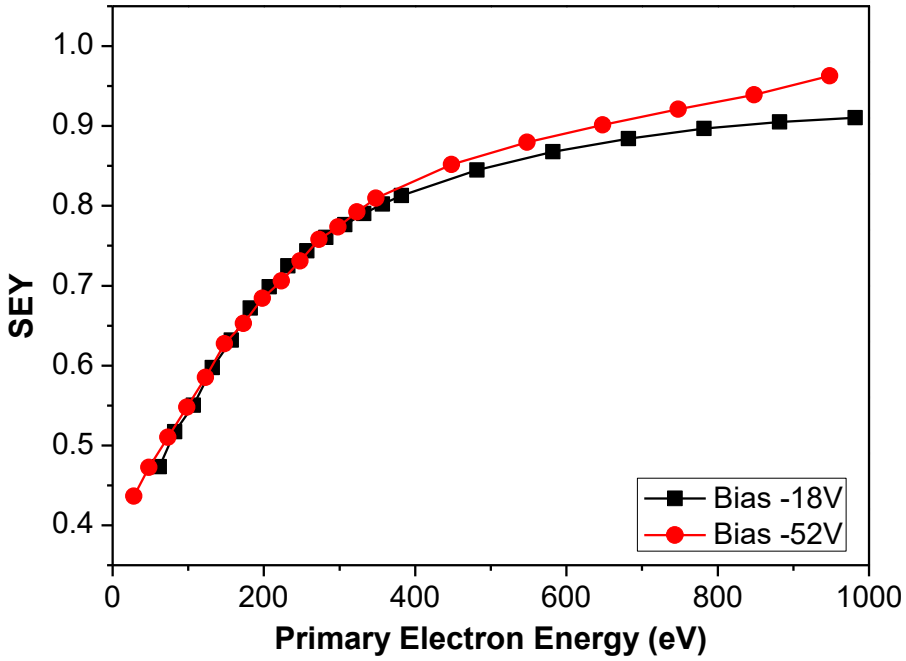

Figure 4-16 The SEY of As-received 50 μm Cu in Air with -18 and -52 V biasing

Another problem we investigated is whether the -18 V bias is above the saturation value to repel all the secondary electrons from the sample. The results shown in **Figure 4-16** are the SEY comparison with the -18 and -52 V on the as-received 50 μm Cu in Air. The SEY with -18 and with -52 V are coincident when the primary electron energy is below 400 eV. The differences of SEYs become bigger at higher energy. However, the maximum value of SEY for normal material is at the low primary electron energy [2]. So in short, a bias of -18 V is above the saturation value and suitable to be used in the future SEY measurements.

4.7 Error Analysis of SEY Measurements

Before starting the SEY measurements, error analysis needs to be calculated

in order to study and evaluate the uncertainties in the SEY measurements. The most important uncertainties in the SEY measurements involve the accuracy of current meters and the error of SEY calculations. The first uncertainty can be easily founded from the hand book of the current meters. In this section, the error analysis of the SEY calculations will be discussed in detail.

In Eq.(4-2), the total SEY is affected by I_F and I_S. The error of I_S (δ_S) is the accuracy of Keithley current meters (±0.01%). However, the error of I_F (δ_F) mainly depends on the fraction of primary electron currents going through the Faraday cup. The primary beam spot fits with Gaussian (normal) Distribution. So the uncertainty of I_F is calculated as below.

A two-dimensional Gaussian function is:

$$f(x,y) = Aexp(-\left(\frac{(x-x_o)^2}{2\sigma_x} + \frac{(y-y_o)^2}{2\sigma_y}\right)) \qquad \text{Eq.(4-3)}$$

Here the coefficient A is the amplitude, x_o,y_o is the centre and σ_x, σ_y are the x and y spreads of the spot.

In order to obtain the fraction of primary electron currents going through the Faraday cup, we integrate the two-dimensional Gaussian function. The dimension of the bottom Faraday cup hole is regarded as the boundary of the integration. The Fractional uncertainty of I_F is the percentage of the beam hitting on the Faraday cup. So the Fractional uncertainty for I_F can be defined and calculated using the following equations:

$$\frac{\Delta I_F}{I_F} = 1 - \frac{\int_{-b}^{b}\int_{-a}^{a} f(x,y)\,dx\,dy}{\int_{-\infty}^{\infty}\int_{-\infty}^{\infty} f(x,y)\,dx\,dy} \qquad \text{Eq.(4-4)}$$

$$= 1 - \frac{A\int_{-b}^{b}\int_{-a}^{a} e^{-\left(\frac{(x-x_o)^2}{2\sigma_x}+\frac{(y-y_o)^2}{2\sigma_y}\right)}\,dx\,dy}{A\int_{-\infty}^{\infty}\int_{-\infty}^{\infty} e^{-\left(\frac{(x-x_o)^2}{2\sigma_x}+\frac{(y-y_o)^2}{2\sigma_y}\right)}\,dx\,dy} \qquad \text{Eq.(4-5)}$$

$$= 1 - \frac{2\pi A\sigma_X\sigma_Y\sqrt{(1-e^{-\frac{a^2}{2\sigma_x^2}})(1-e^{-\frac{b^2}{2\sigma_y^2}})}}{2\pi A\sigma_X\sigma_Y} \quad \text{Eq.(4-6)}$$

$$= 1 - \sqrt{(1-e^{-\frac{a^2}{2\sigma_x^2}})(1-e^{-\frac{b^2}{2\sigma_y^2}})} \quad \text{Eq.(4-7)}$$

The Gaussian functions of Wire 1 and Wire 2 are chosen to calculate the volume of primary electron passing through the Faraday cup. The centre point (X_O, Y_O) are set as the origin coordinates (0,0). For each wire scan, the beam profile for different energies is fitted by the Gaussian function using Origin software (Origin Pro 8.6). (a, –a) and (b, -b) represent to the beam spot boundary measured by wire 1 and wire 2, separately. σ_X and σ_Y are the width of the distribution at different energy for wire 1 and wire 2, respectively. All the parameters are determined by fitting with Gaussian function from the Origin software. In **Table 4-1**, it shows all the parameters involved in the I_F uncertainty calculations.

Table 4-1 The beam spot boundary and distribution width at different energies for both wire 1 and wire 2

Energy (eV)	Beam spot boundary for W1	Beam spot boundary for W2	Distribution width of W1	Distribution width of W2	Fractional uncertainty of I_F
1000	(19,-19)	(12,-12)	8.78	7.09	17%
600	(21,-21)	(11,-11)	4.06	3.20	0.2%
200	(12,-12)	(8,-8)	2.30	2.26	0.1%
150	(11,-11)	(6,-6)	1.46	1.55	0.03%
100	(11,-11)	(5,-5)	3.2	4.11	28%
80	(12,-12)	(7,-7)	2.6	4.68	18%

Based on SEY equation, the uncertainty of SEY is composed of the uncertainty of I_F *and* I_S. So we obtain the following relation:

$$\sigma_\delta = \sqrt{(\frac{\partial\delta}{\partial I_F})^2(\Delta I_F)^2 + (\frac{\partial\delta}{\partial I_S})^2(\Delta I_S)^2} \quad \text{Eq.(4-8)}$$

Therefore,

$$\frac{\Delta\delta}{\delta} = \frac{I_S}{|I_S+I_F|}\sqrt{(\frac{\Delta I_F}{I_F})^2 + (\frac{\Delta I_S}{I_S})^2} \quad \text{Eq.(4-9)}$$

When $I_F >> I_S$, it is easy to get:

$$\frac{\Delta\delta}{\delta} \approx 0, \quad \text{Eq.(4-10)}$$

Otherwise,

$$\frac{\Delta\delta}{\delta} \approx \sqrt{(\frac{\Delta I_F}{I_F})^2 + (\frac{\Delta I_S}{I_S})^2} \quad \text{Eq.(4-11)}$$

So if all the data are taken into Eq (4-11), then we can obtain the total error for the SEY measurements.

In the conclusion, the error of the SEY measurements is calculated by the accuracy of the SEY measurements and was estimated to be within 1% for primary electron energies between 80 and 800 eV and about 6% for primary electron energies above 800 eV.

4.8 Conclusions

The SEY measurement setup has been designed and built by myself. It consist of three chambers, which are load lock chamber, SEY measurement chamber and surface treatment and analysis chamber. In order to understand the beam size of the primary electron, the beam profile of the Kimball electron gun has been studied by two ways, which are phosphor screen method and wire scanner method. The aim of this measurement is to make sure that the beam spot can go through the holes at the top and bottom of the Faraday cup. The diameters of the spots vary between 3 and 6 cm, which means the beam can pass through the top and bottom holes of Faraday cup. Biasing effect on the

sample has been studied in order to repel most secondary electron to the Faraday cup. A bias of -18 V on sample hold has been used in the future SEY measurement. Finally, error analysis has been calculated to evaluate the uncertainties in the SEY measurements. It was estimated to be with 1% for primary electron energies between 80 and 800 eV and about 6% for above 800 eV.

References

[1] V. Baglin, J.Bojko, O. Gröbner, B. Henrist, N. Hilleret, C. Scheuerlein, EPAC 2000, Vienna, Austria, 2000, pp. 217-221.

[2] A. Shih, J. Yater, C. Hor, R. Abrams, Applied Surface Science, 111 (1997) 251-258.

Chapter 5. Transition Metals and Their Coatings

NEGs have been used in the vacuum systems of synchrotrons, particle accelerators and colliders to achieve extremely high vacuum, where vacuum conductance is low. Appropriate, NEG materials usually display properties, such as a good adhesion to the substrate, a low activation temperature, a high oxygen solubility, a high hydrogen diffusion, a large pumping speed and a low PEY (photon electron yield) and SEY [1, 2]. NEG films are usually composed of a mixture of Ti, Zr, V and Hf transitional metals. SEY values of 0.9 and 1.1 from the atomically cleaned Ti and Zr surfaces, respectively, have been reported in the literature [3]. But oxide contamination layers are formed if the surfaces are exposed to air and as a result the SEY of vacuum component metal surfaces are generally higher than the SEY of the corresponding atomically clean metals [4]. However, the SEY of air-exposed metals can be reduced by different surface treatments such as electron conditioning and in-situ vacuum bakeouts [5].

The aim of this chapter was to study the SEYs of the transition metals (Ti, Zr, V and Hf) (bulk samples and their coating on stainless steel substrates) as well as their alloys coatings on Silicon and stainless steel. Electron beam exposure (conditioning) and thermal treatment will be studied on each samples. XPS analysis also will be measured before and after each type of sample treatment to determine surface chemical composition of the surface. The SEM will be studied to show the sample morphology and XRD analysis will be used to calculate the crystalline size of bulk transition metals. All the samples produced, studied and reported in this chapter are summarized in **Table 5-1**.

All the samples were studied following the procedure as described below:

1. Loading a new sample and pumping it overnight, then transferring to the SEY measurement chamber;
2. Pumping for half hour;
3. Measuring SEY as a function of primary electron energy, $\delta(E)$;
4. Transfer sample to analysis chamber;
5. Providing the XPS analysis;
6. Applying one of the treatments;
    a. electron conditioning with a flood electron gun to study the dose (or electron scrubbing) effect,
    b. heat to study the bakeout effect or
7. Providing the XPS analysis;
8. Transfer sample to the SEY measurement chamber;
9. Repeating Steps 3-8.

Table 5-1 Samples and applied characterization techniques

Sample	Metal	Substrate	XPS	E-conditioning	Heating
Bulk	Ti	Sample plate	Yes	Yes	Yes
	Zr	Glued on the 306L SS	Yes	Yes	-
	V	Glued on the 306L SS	Yes	Yes	-
	Hf	Glued on the 306L SS	Yes	Yes	-
Coatings	Ti	306L SS	Yes	Yes	Yes
	Zr	306L SS	Yes	Yes	Yes
	V	306L SS	Yes	Yes	Yes
	Hf	306L SS	Yes	Yes	Yes
	Ti-Zr-V	Si	Yes	Yes	-
	Ti-Zr-V	306L SS	Yes	Yes	Yes

5.1 Bulk Transition metals

Figure 5-1 showed the SEM for bulk Ti, Zr, V and Hf, respectively. It showed clearly that all the surfaces are roughly flat, but there were some cracks on the surfaces, which could be seen from the high resolution SEM pictures.

In **Figure 5-2,** the SEYs of bulk Ti are plotted as a function of primary electron energy showing reduction of SEY with an electron dose. The SEY values exhibit the same trend in behavior *viz.* initial rising with energy at low primary electron energy to a maximum value δ_{max} at a few hundred electron volts followed by a steady decline. The initial drop in the SEY with electron dose is larger than subsequent decreases. The δ_{max} of as-received Ti was 2.30 but it dropped to 1.93, 1.50, 1.30, 1.19 after doses of 1.7×10^{-4}, 4.5×10^{-4}, 2.7×10^{-3}, and 7.9×10^{-3} $C\cdot mm^{-2}$, respectively. The primary electron energy corresponding (E_{max}) to δ_{max} of Ti moves to lower primary electron energy after electron bombardments from 257 to 232 eV.

The SEY of bulk Zr, V and Hf as a function of primary electron energy demonstrate similar tendencies to Ti and their reduction with electron doses is shown in **Figure 5-3**. The δ_{max} of as-received Zr, V and Hf were 2.31, 1.72 and 2.45, respectively. In all these cases E_{max} also moves to lower value after electron bombardments: E_{max} for as-received Zr, V and Hf is at 282, 232 and 332 eV. After a dose of 6.4×10^{-3} $C\cdot mm^{-2}$, δ_{max} of Zr drops to 1.27. δ_{max} for V and Hf drop to 1.48 and 1.40 after doses of 1.3×10^{-3} and 5.2×10^{-3} $C\cdot mm^{-2}$, respectively. E_{max} of Zr, V and Hf is shifted to 257, 207 and 307 eV.

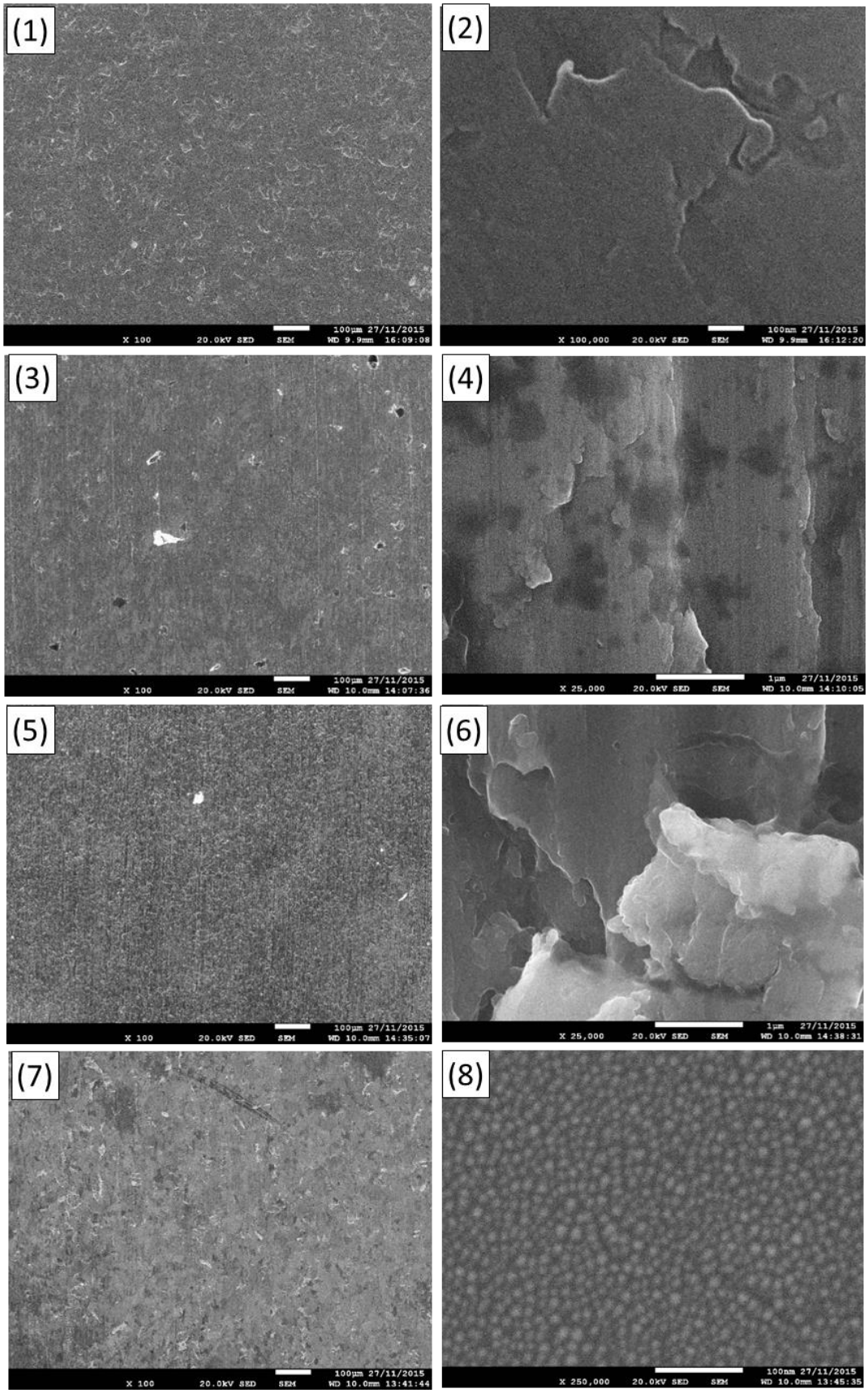

Figure 5-1 SEM pictures for bulk (1) Ti, (3) Zr, (5) V and (7) Hf and region SEM pictures for bulk (2) Ti, (4) Zr, (6) V and (8) Hf

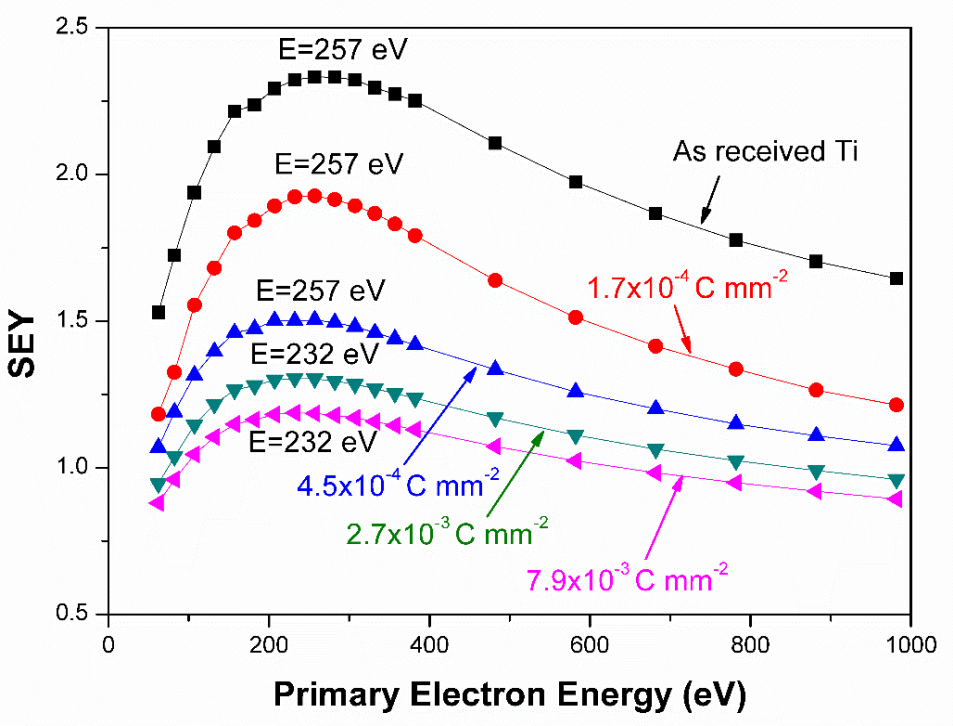

Figure 5-2 Reduction of δ(E) after conditioning with various electron doses for bulk Ti.

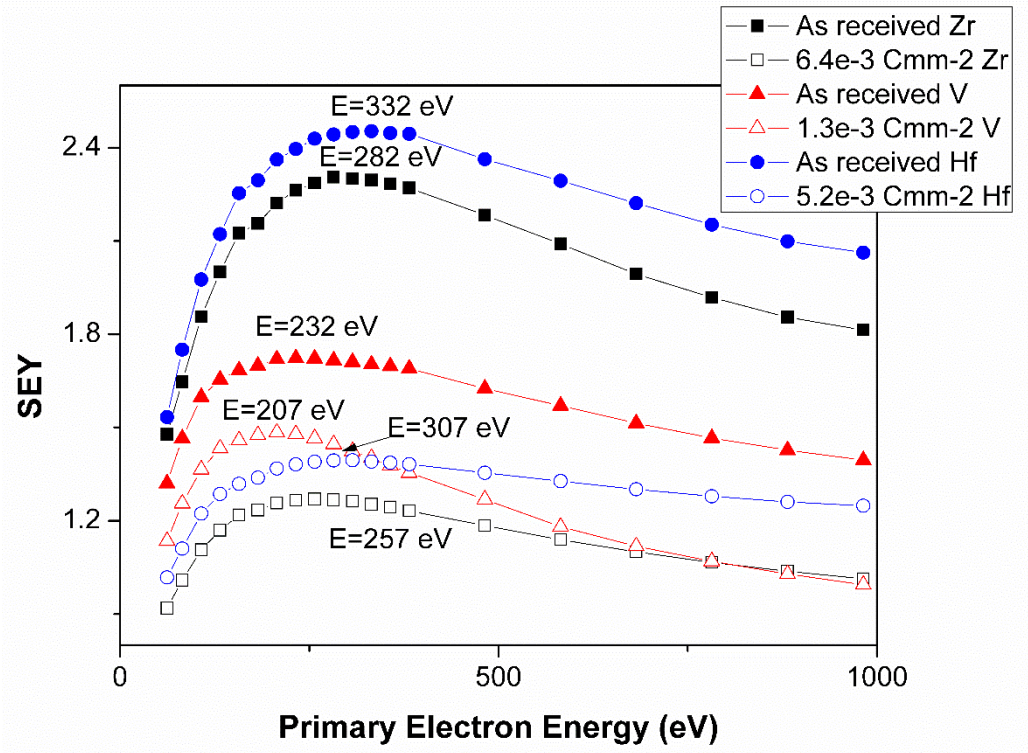

Figure 5-3 Reduction of δ(E) after conditioning with electrons for Zr, V and Hf.

5.1.2 The XPS spectra of bulk transition metals after electron bombardment

As the SEY of a material depends on the chemical elements adsorbed on its surface, chemistry analysis is required to understand the evolution of the SEY during the process of electron conditioning [5]. XPS analysis was carried out on bulk Ti, Zr, V and Hf samples, see **Figure 5-4**.

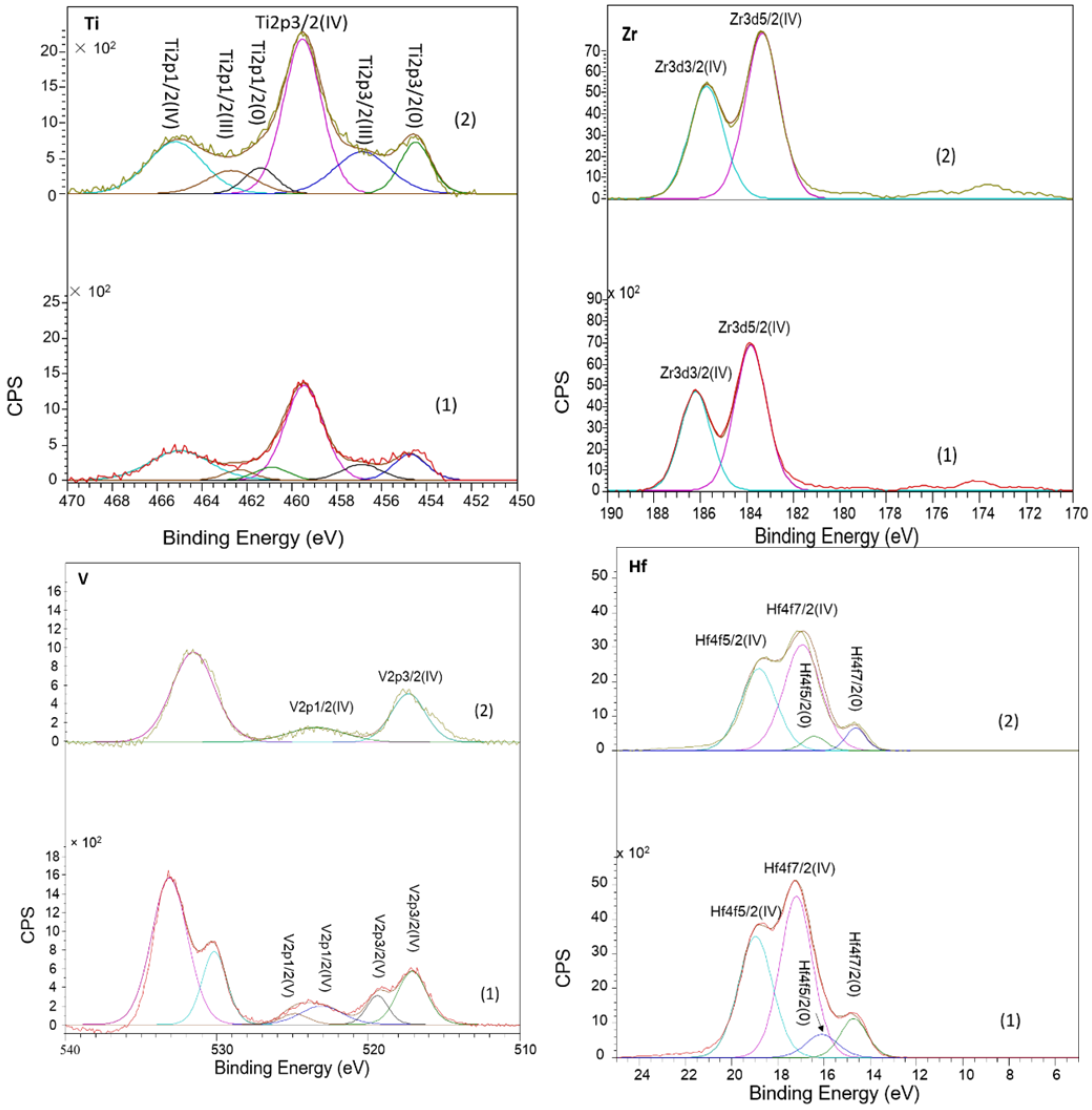

Figure 5-4 The XPS spectra of bulk Ti, Zr, V and Hf (1) as-received, (2) after electron bombardment

Figure 5-4 shows the XPS region spectra of Ti, Zr, V and Hf peak of as-received and electron bombarded bulk Ti, Zr, V and Hf, separately. Ti2p peak is a doublet

due to split spin-orbit components. The Ti2p3/2 peak positions of as-received bulk Ti are at the binding energy of 454.7 eV (Ti(0)), 456.9 eV (Ti(III)) and 459.2 eV (Ti(IV)) which indicates that the surface of as-received bulk Ti is in the state of mixture of metal Ti, Ti_2O_3 and TiO_2. The ratio of Ti(0), Ti(III) and Ti(IV) is shown in **Table 5-2**. After electron bombardment, the Ti2p3/2(IV) decreases from 70.5 to 59.9% and the Ti2p3/2(III) increase from 12.4 to 26.4%, which means the oxidized TiO_2 on the surface, has changed into Ti_2O_3 [6].

The spectra of Zr3d of bulk Zr is shown in **Figure 5-4** for both as-received and electron bombardment. Zr3d peak is a well-resolved doublet due to spin-orbital effects. The Zr3d5/2 peak and Zr3d3/2 peak positions of as-received bulk Zr are at the binding energy of 186.2 eV (Zr(IV)) and 183.8eV (Zr(IV)), respectively. After an electron bombardment dose of 6.3×10^{-3} $C\cdot mm^{-2}$, the Zr3d5/2 and Zr3d3/2 peaks keep the same positions, which suggests that both as-received and electron bombarded Zr on stainless steel are ZrO_2.

The spectra of V2p of bulk V and Hf4f of bulk Hf are shown in **Figure 5-4** for both as-received and electron bombardment, respectively. The surface of as-received bulk V is composed of VO_2 and V_2O_5. So the V2p3/2 peak of bulk V is at the binding energy of 517.2 eV (V2p3/2(IV) and 519.4 eV (V2p3/2(V)) and the V2p1/2 peak of bulk V are at the binding energy of 523.1 eV (V2p3/2(IV) and 524.9 eV (V2p3/2(V)). The ratio of V2p3/2(IV)) and V2p3/2 (V) are 71.1% and 28.9% as shown in **Table 5-2**.After electron bombardment, the V2p3/2 and V2p1/2 peak shift to 517.3 and 523.4 eV, respectively, which indicate that only VO_2 exists on the surface.

The surface of as-received Hf consist of metal Hf and HfO_2. Peaks in the Hf4f region have an asymmetric peak shape. The Hf4f7/2 peak of bulk Hf are at the binding energy of 14.7 eV (Hf4f7/2(0)) and 17.1 eV (Hf4f7/2(IV)) and the Hf4f5/2 peak of bulk Hf are at the binding energy of 16.1 eV (Hf4f5/2(0)) and 19.0 eV (Hf4f5/2(IV)). The ratio of Hf4f7/2(0)) and Hf4f5/2 (IV) are 16.6 and 83.4% in

Table 5-2. After electron bombardment, the positions of Hf4f7/2 and hf4f5/2 stay the same. So the metal Hf and HfO_2 still exist on the surface. However, the ratio of Hf4f7/2(0)) and Hf4f5/2 (IV) has changed to 10.4 and 89.6%.

From **Figure 5-4** and **Table 5-2**, it is clearly shown that the peaks of Ti and V have been shifted to lower positions. The composition of Ti2p3/2 (IV) reduced from 77.0% to 68.2% and the composition of the Ti2p3/2 (III) and Ti2p3/2(0) increase to 22.1% and 9.2, respectively, after electron bombardment. The mixture of Ti and Ti_2O_3 increase and TiO_2 reduced. Similarly, after electron bombardment, only VO_2 exists on the surface and V_2O_5 disappear. These means that oxygen is slightly reduced by long electron bombardment on the surface. The electron bombardment breaks the metal and oxygen bonds into low SEY defective suboxide [5]. However, ZrO_2 still keeps the same on the bulk Zr surface. The concentration of oxygen on the Hf surface is a bit more than that of as-received bulk Hf.

Table 5-2 The concentration of bulk Ti, Zr, V and Hf after electron bombardment

bulk Ti	Ti2p3/2(0) 454.7 eV	Ti2p3/2(III) 456.9 eV	Ti2p3/2(IV) 459.2 eV
As-recieved	17.1%	12.4%	70.5%
Electron bombarmdent	18.2%	26.4%	59.9%
Bulk Zr	Zr3d5/2(IV) 183.8 eV		
As-received	100%		
After electron bombardment	100%		
Bulk V	V2p3/2(IV) 517.2 eV		V2p3/2(V) 519.4 eV
As-received	71.1%		28.9%
After electron bombardment	100%		
Bulk Hf	Hf4f7/2(0) 14.7 eV		Hf4f7/2(IV) 17.1 eV
As-received	16.6%		83.4%
After electron bombardment	10.4%		89.6%

The XPS spectra of carbon were investigated for bulk Ti, Zr, V and Hf (**Figure 5-5**). The C1s peak for as-received bulk Ti is at the binding energy of 285.0 eV, which is attributed to C-C and C-H, and 288.8 eV which is ascribed to C=O. Electron bombardment to a dose of 7.9×10^{-3} C·mm^{-2} increases the C1s peak at 284.9 eV associated with graphitic carbon. The intensity of carbon peak increases, which is believed to be a consequence of the growth of a thin graphitic film on the surface. Also the C=O peak at 288.8 eV disappears and only small C-O peak remains. The carbon peaks for Zr, V and Hf show a similar performance after electron bombardment. The peaks related to the graphitic carbon increase. The SEYs after electron bombardments reduce due to the increasing the graphic carbon layer on the surfaces [7].

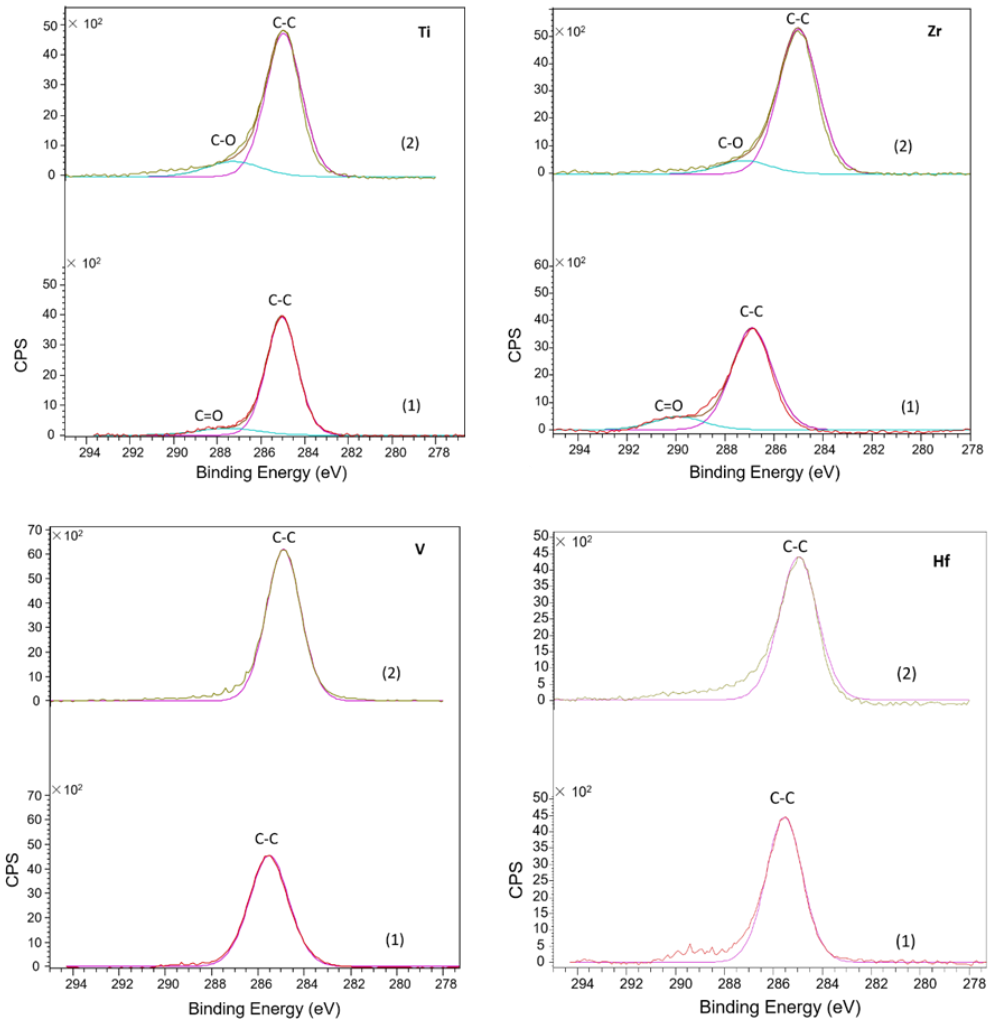

Figure 5-5 The carbon spectra of bulk Ti, Zr, V and Hf (1) as-received, (2) after electron bombardment

5.1.3 The SEY of bulk Ti after thermal treatment

Figure 5-6 shows the SEY of bulk Ti as a function of primary electron energy varied with the heating treatment. After heating to 350 ^{0}C for 2.5 hours, the SEY of bulk Ti has dropped to 1.21 from 2.30.

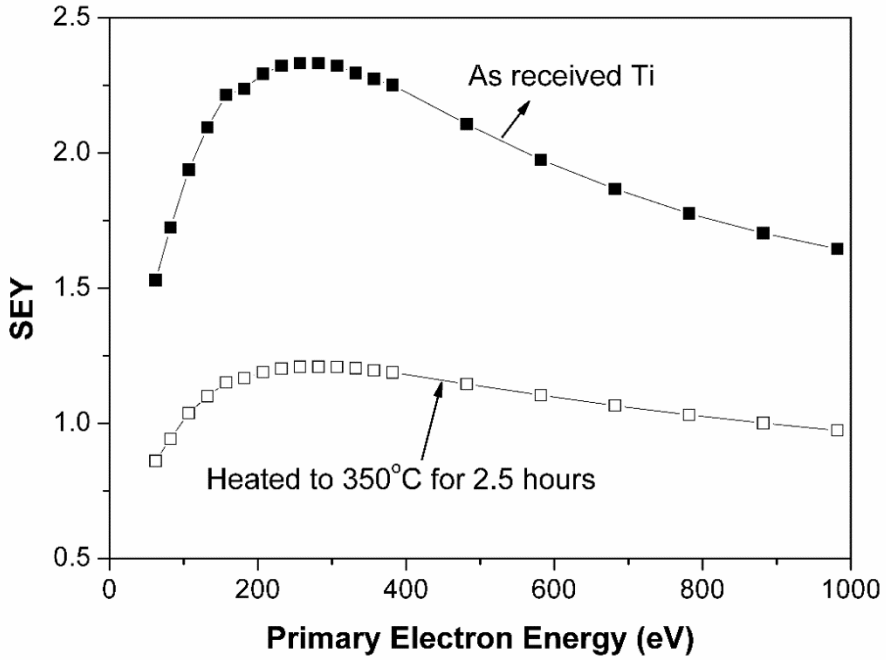

Figure 5-6 Reduction of δ(E) after thermal treatment.

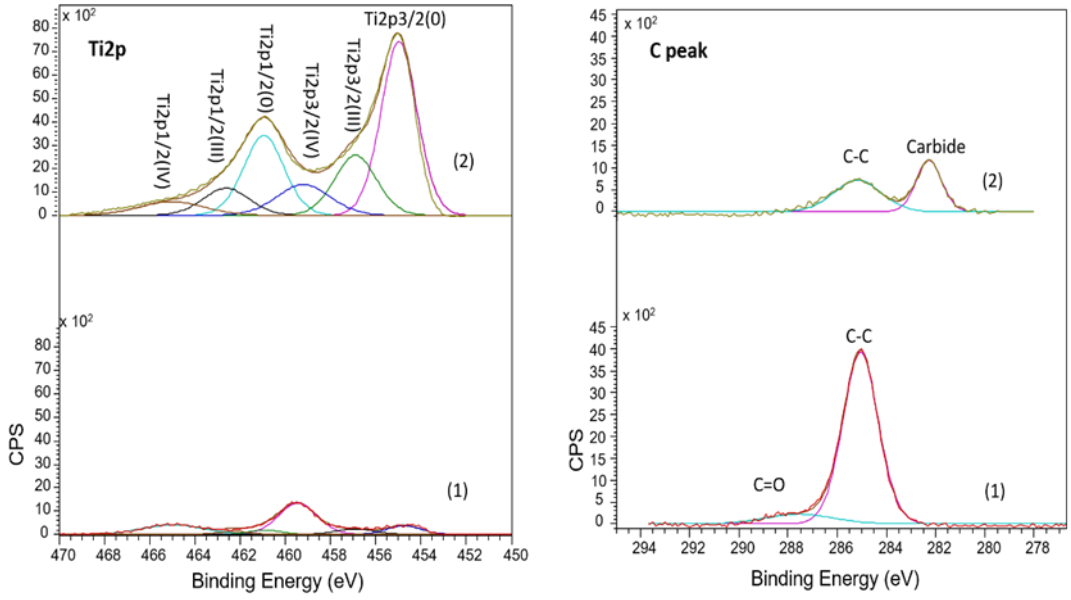

Figure 5-7 The XPS spectrum of Ti2p of bulk Ti (1) as-received, (2) after heating to 350 ºC for 2.5 hours and the carbon spectrum of bulk Ti (1)as-received, (2) after heating to 350 ºC for 2.5 hours

Table 5-3 The concentration of Ti2p3/2 of bulk Ti

bulk Ti	Ti2p3/2(0) 454.7 eV	Ti2p3/2(III) 456.9 eV	Ti2p3/2(IV) 459.2 eV
As-recieved	17.1%	12.4%	70.5%
Heated to 350 ^{o}Cfor 2.5 hours	59.8%	24.4%	15.8%

Figure 5-7 shows the the XPS spectra of Ti2p and carbon of as-received and heated bulk Ti. The XPS analysis also showed that both the as-received and heated surface consisted of a mixture of two different state of oxide (TiO_2 and Ti_2O_3) and metal Ti. Compared with the as-received sample, $Ti2p_{3/2}$ and $Ti2p_{1/2}$ peaks with all the states have increased in intensity and the peaks all broadened with an overall shift towards the lower binding energy, after heating treatments. **Table 5-3** shows the concentration of Ti2p3/2 of as-received and heated bulk Ti. It is clearly shown that the Ti2p3/2(0) increases to almost 60% and Ti2p3/2(IV) reduced greatly to 15.8% from 70.5%. The reason is that after thermal treatment, oxygen has been diffused into the bulk and the oxide states on the surface reduce. So the SEY of bulk Ti reduces from 2.30 to 1.21 after heating to 350 ^{0}C for 2.5 hours due to reducing the surface contaminations.

The XPS spectrum of carbon shows there is a low-energy shoulder at 282.3 eV which is assigned to Ti carbide in addition to the graphitic carbon peak at 285.1 eV after heating. The C=O peak has been disappeared compared the as-received sample. The annealed surface has a lower SEY, indicating a more conducting surface. This result supports the conclusion obtained from the XPS analysis that metallic peak increases and the oxide state reduces. Additionally, some carbide and graphitic carbon formed on the surface contribute to an overall low SEY [8].

5.1.4 XRD analysis of bulk transition metals

The XRD analysis of bulk Ti, Zr, V and Hf is presented from **Figure 5-8** to **Figure 5-11**, respectively. The strongest peak with lowest 2-theta angle has been

chosen for each sample to calculate the crystal size using the Scherrer equation (Equation 3-4 in Chapter 3). The crystalline size for Ti (002) is 57.4 nm. Then the crystalline size for Zr (002), V (110) and Hf (101) is 32.3, 43.9 and 56.1 nm, respectively.

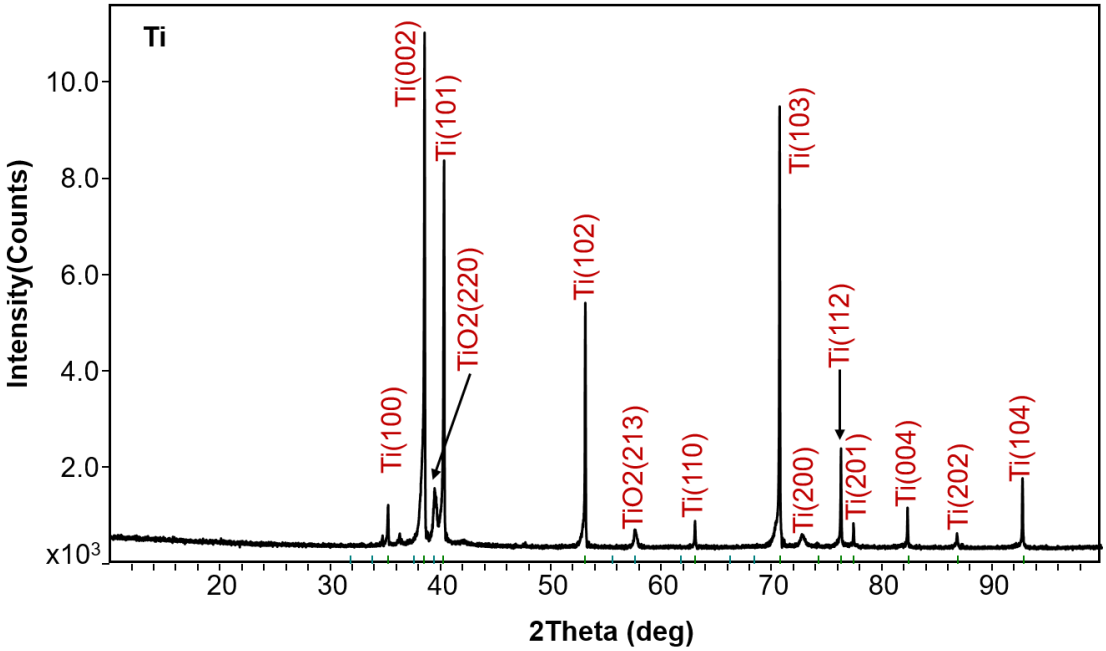

Figure 5-8 XRD analysis of bulk Ti

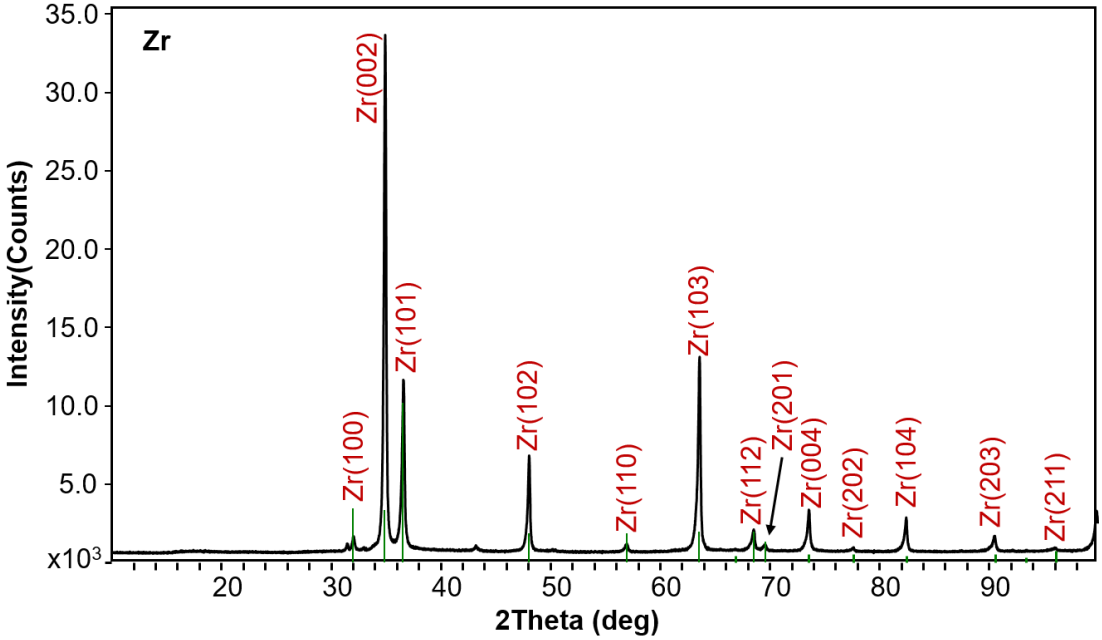

Figure 5-9 XRD analysis of bulk Zr

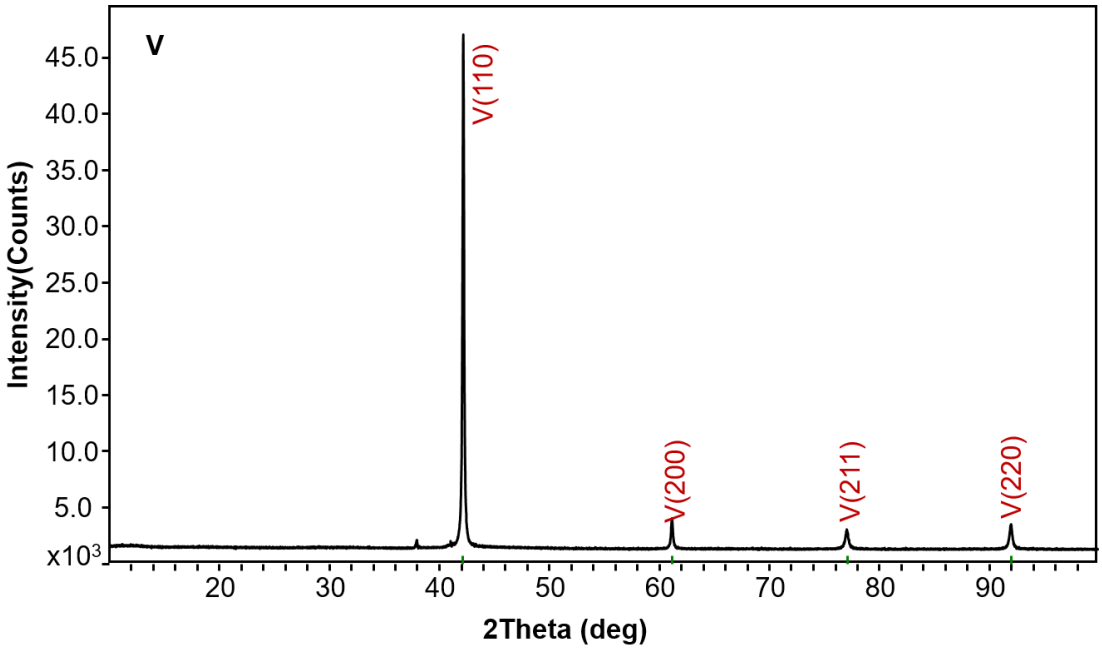

Figure 5-10 XRD analysis of bulk V

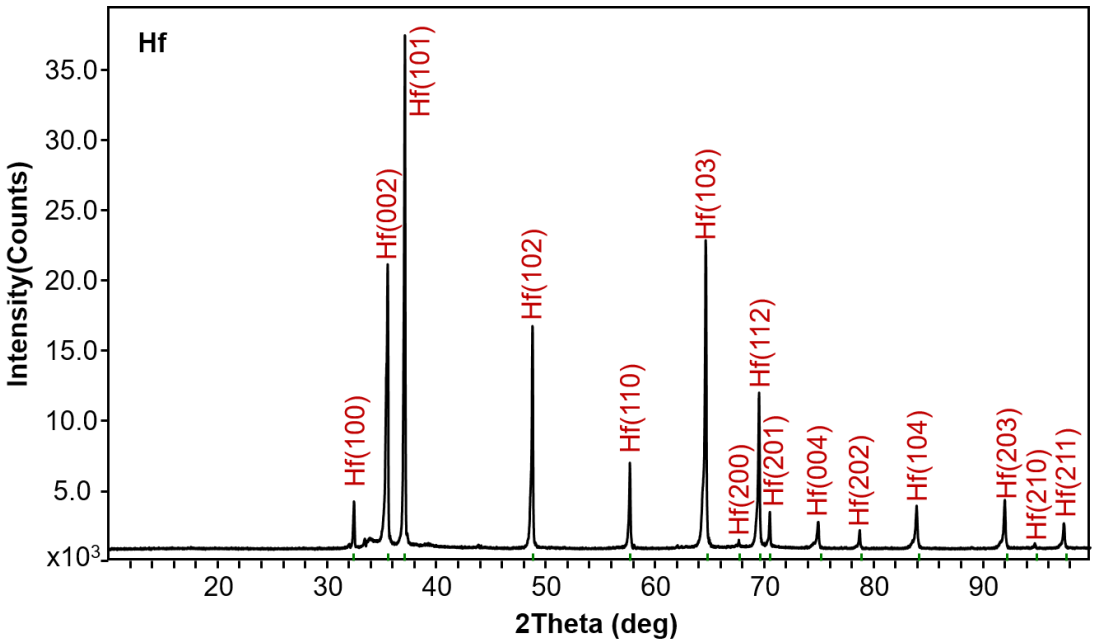

Figure 5-11 XRD analysis of bulk Hf

5.2 Thin film transition metal on stainless steel

Thin films of transition metal (Ti, Zr, V and Hf) were deposited using magnetron

sputtering with pulsed DC power supply. The films were directly deposited at nominal thickness of 1 micron on an Omicron type stainless steel sample holder. The SEM micrographs of the films are shown in **Figure 5-12**. It can be seen that all the surfaces of films are flat, however, from high resolution SEM pictures, it also shows cracks on the surface.

5.2.1 The SEY of Thin film transition metal on stainless steel

Figure 5-13 shows the SEY of thin films of Ti, Zr, V and Hf on the stainless steel as a function of primary electron energy for both before and after electron beam conditioning. The δ_{max} seems to correlate with the elemental atomic number Z where Hf with highest atomic number value yields the highest δ_{max}. However, as in the case of the transition bulk metals the vanadium δ_{max} has the lowest value. Similarly, the bulk samples have the same the trend. The SEY of Hf is the largest but that of V is the lowest.

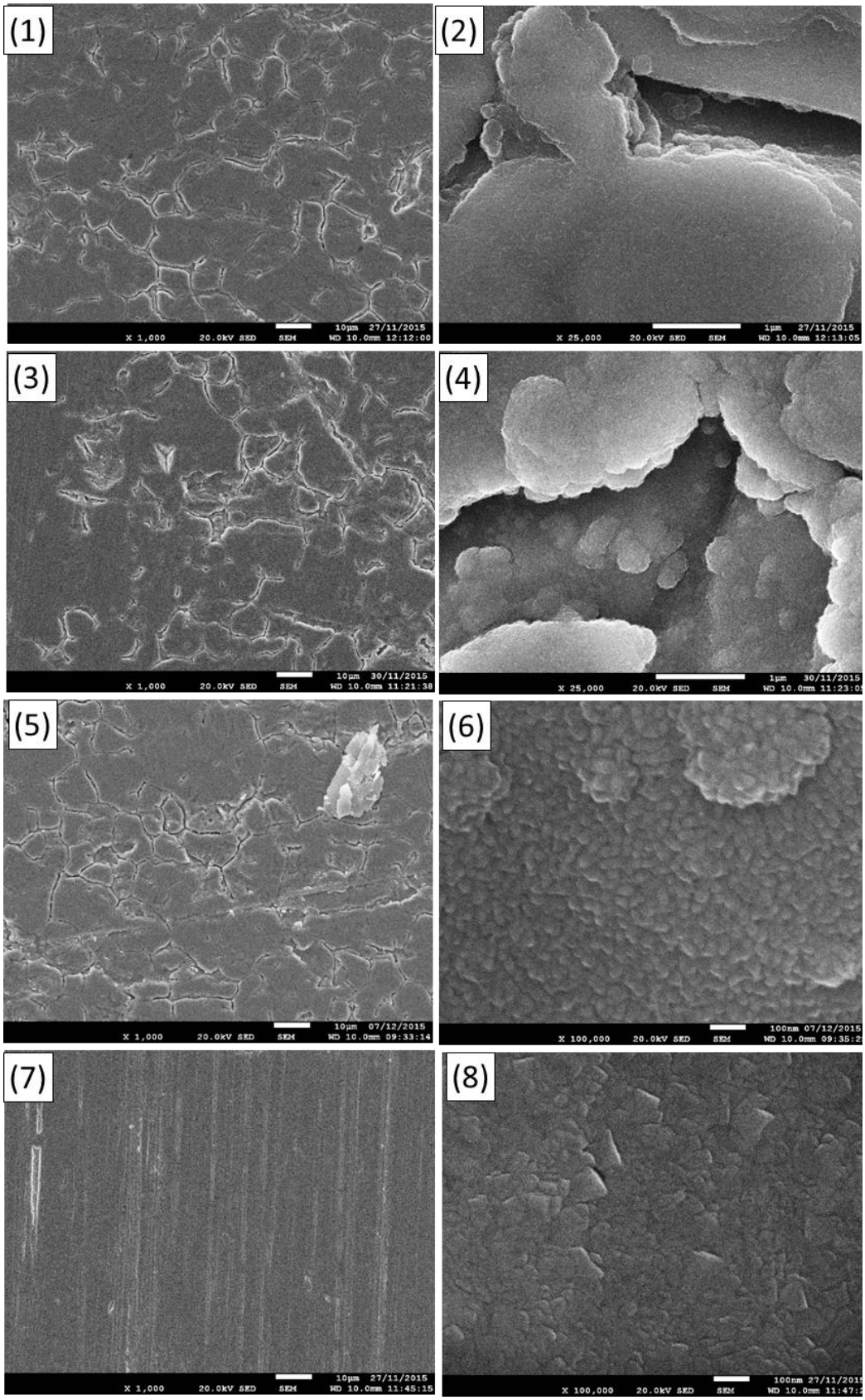

Figure 5-12 SEM pictures for thin films of (1) Ti, (3) Zr, (5) V and (7) Hf deposited on SS sample and region SEM pictures for thin films of (2) Ti, (4) Zr, (6) V and (8) Hf deposited on SS sample.

In the case of Ti, Zr and Hf the SEY remained above 1 for all the range of chosen energies, gradually increasing as a function of increasing primary electron energy, maximizing at (δ_{max}) and then decreasing gradually at a lower rate. For Vanadium, the SEY increases with increasing primary energy and up to 150 eV (Ep), the SEY remained below 1. The rate of increase stayed constant up to 230 eV and then reduced considerably. Within the chosen primary electron energy range δ did not reach the maximum value. Electron conditioning resulted in much reduced SEY but the variation of δ as a function of primary electron energy stayed almost the same for all transition metal coatings, which have the same trend as the bulk samples.

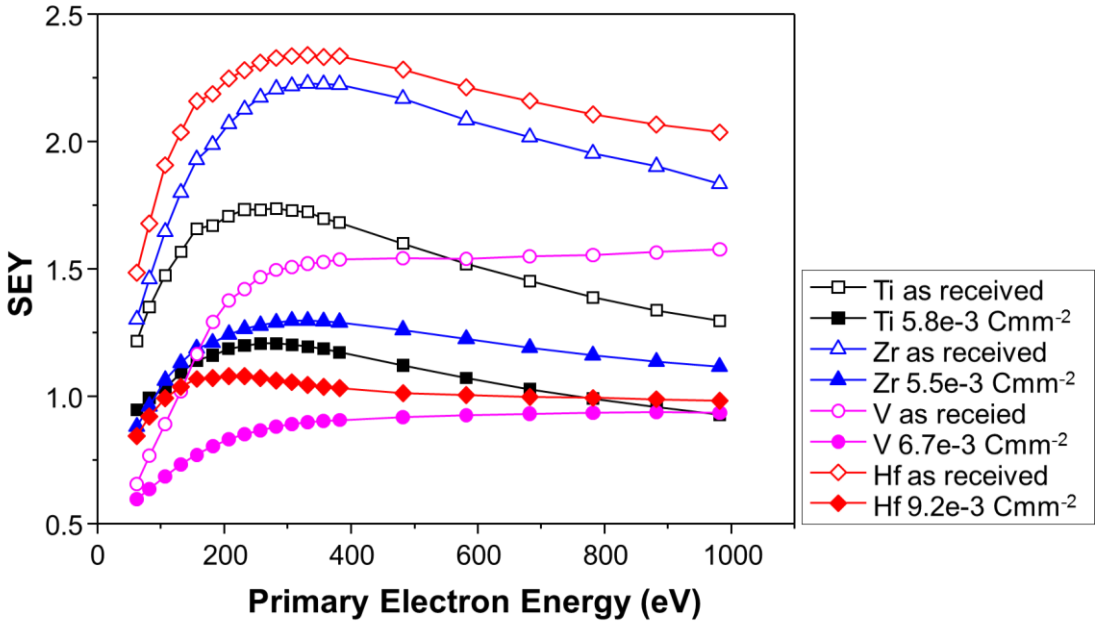

Figure 5-13 Reduction of δ(E) after conditioning with various electron doses for Ti, Zr, V and Hf coatings on stainless steel substrates.

Figure 5-14 shows the SEY of thin film of Ti, Zr, V and Hf on the stainless steel as a function of primary electron energy for both before and after thermal treatments. It can be seen that after thermal treatment δ as a function of primary electron energy was reduced considerably for all the transition metals and stayed about or below 1 for Ti, Zr and V over the full range of primary energy. The SEY increased with increasing primary energy up around 200 eV and then

reduced considerably to flatten off before decreasing gradually. Compared to the bulk Ti, after heating, the SEY of bulk Ti increased with increasing primary energy up around 250 eV and then decreased gradually. The SEY of heated bulk Ti is about 1.2, which is slightly higher than thin film. In the case of Hf, although δ decreased considerably over the entire range of primary electron energy, its value stayed above 1 for primary energy larger than 100 eV.

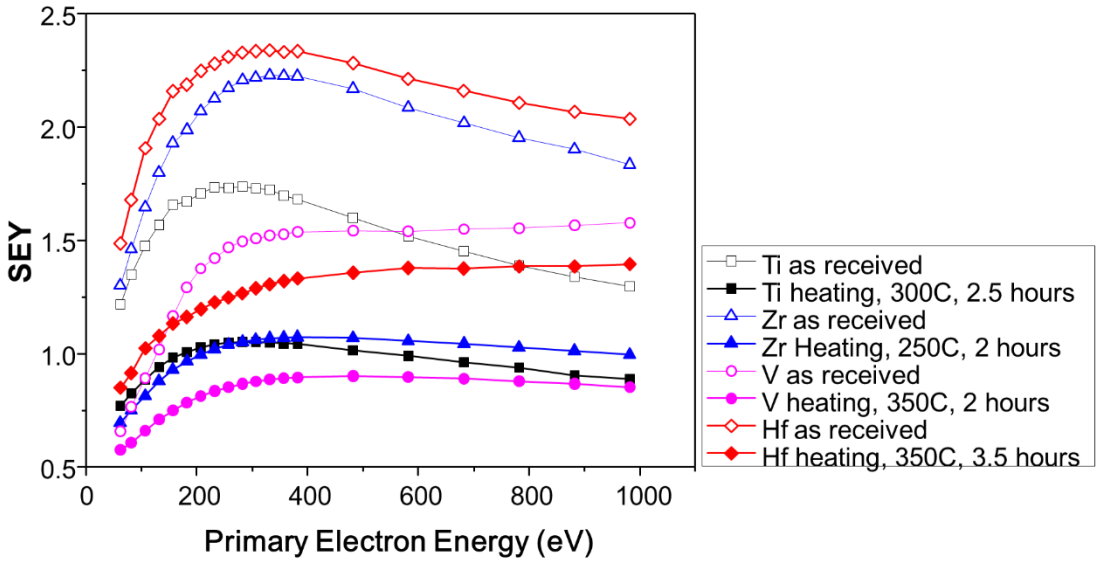

Figure 5-14 Reduction of δ(E) after thermal treatment of Ti, Zr, V and Hf coatings on stainless steel substrates.

5.2.2 XPS of transition metal films on the stainless Steel

Figure 5-15 shows the XPS spectra of Ti2p peak of Ti on the stainless steel. In **Figure 5-15**(1), the Ti2p3/2 and Ti2p1/2 positions are at three different binding energies, which indicate there are three different states of Ti on the surface. The Ti2p3/2 peak positions of as-received Ti coating are at the binding energy of 454.9 eV (Ti(0)), 457.4 eV (Ti(III)) and 459.4 eV (Ti(IV)) [6] and the Ti2p3/2 peak are at the binding energy of 461.1 eV (Ti(0)), 462.3 eV (Ti(III)) and 465.1 eV (Ti(IV)). This means that the surface of as-received Ti coating on the stainless steel is in the state of mixture of metal Ti, Ti_2O_3 and TiO_2. The ratio of Ti(0), Ti(III) and Ti(V) is shown in **Table 5-5 The concentration of Zr, V and Hf on the** for as-received, electron bombarded, and heated Ti thin film on the

stainless steel, separately. After electron bombardment, the Ti2p3/2(IV) decreases from 77.0% to 68.2% and the Ti2p3/2(III) increase from 17.8% to 22.1%, which means a part of oxidized TiO_2 on the surface has transferred into Ti_2O_3. Also, the Ti2p3/2(0) increase from 5.2% to 9.2%. After heating treatments, the Ti2p3/2(0) increases to 65.8% and Ti2p3/2(IV) reduced extremely to 7.8%.

Compared to the bulk Ti, the surface of as-received Ti coating is more oxidized. The concentrations of Ti2p3/2(IV) and Ti2p3/2(III) is higher than those of bulk Ti. After electron bombardments, the concentration of Ti2p3/2(IV) for both bulk Ti and Ti coating has been reduced. However, the concentration of Ti2p3/2(III) for both Ti and Ti coating been increased. This means that after continual electron bombardment, oxidized surfaces convert to suboxides. Thermal treatment removed the adsorbed gases and oxidation layer on the surface of both bulk Ti and Ti coating.

In **Figure 5-16**, the shifts of C peaks of Ti on the stainless steel are apparent after electron bombardments and thermal treatment. The C peak of the as-received Ti on the stainless steel is at the binding energy of 287.5 eV, which is attributed to C=O and at the binding energy of 285.1eV, which is related to C-C and C-H. After electron bombardment, the position of C1s peak is shifted to 286.6 eV (C-O) and 284.8 (C-C), respectively. After thermal treatment, in addition to the graphitic carbon peak at 284.9 eV, there is a low-energy shoulder at 282.4 eV which is assigned to Ti carbide.

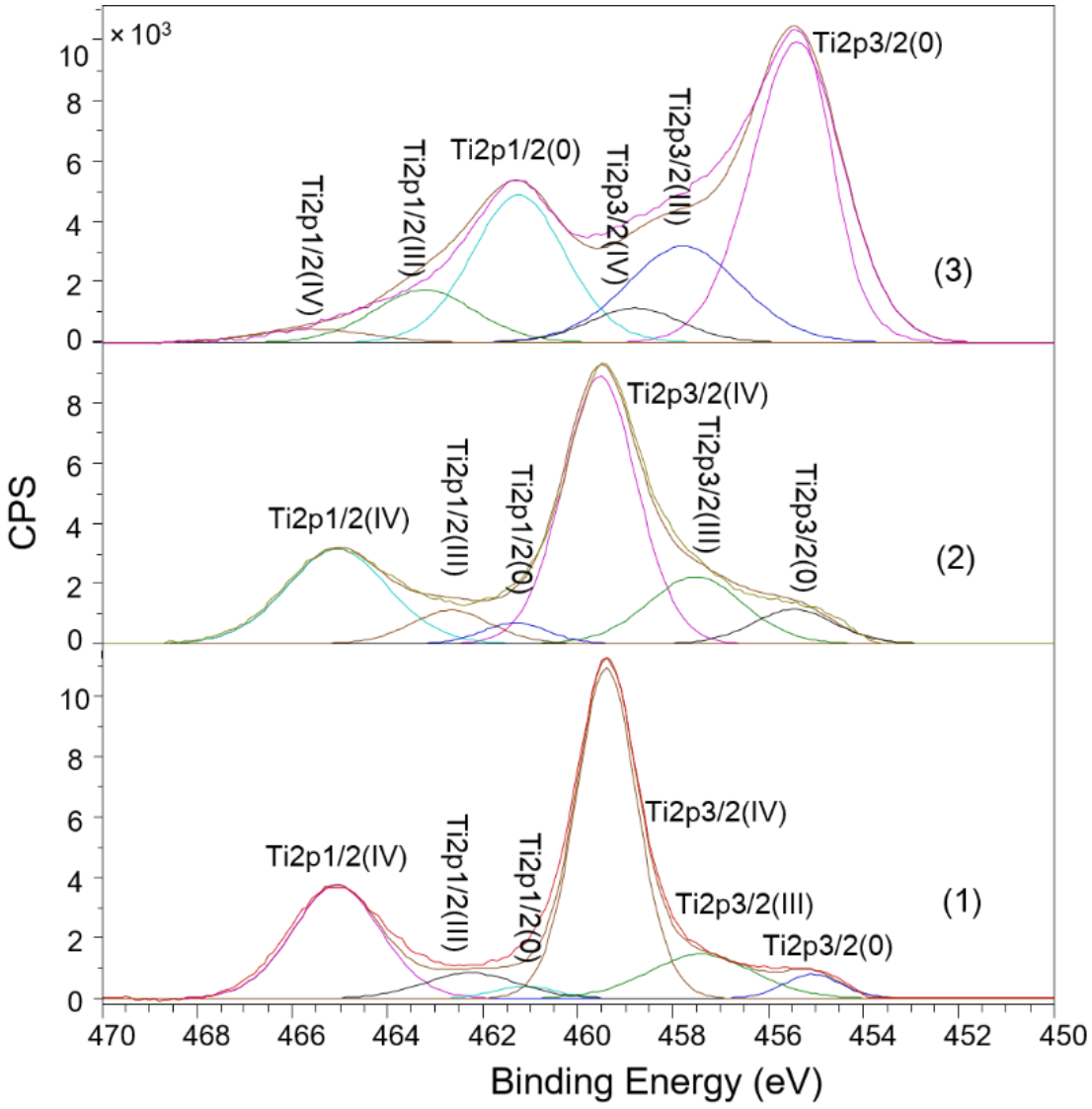

Figure 5-15 The XPS spectra of Ti2p peak on Ti on the SS (1) as-received, (2) after electron bombardment, (3) after heating to 350 ^{0}C for 2.5 hours

Table 5-4 The concentration of Ti2p3/2 of Ti on the SS

Ti on the SS	Ti2p3/2(0) 454.9 eV	Ti2p3/2(III) 457.4 eV	Ti2p3/2(IV) 459.4 eV
As-recieved	5.2%	17.8%	77.0%
Electron bombarmdent	9.2%	22.1%	68.2%
Heated to 350 ^{o}C for 2.5 hours	65.8%	26.4%	7.8%

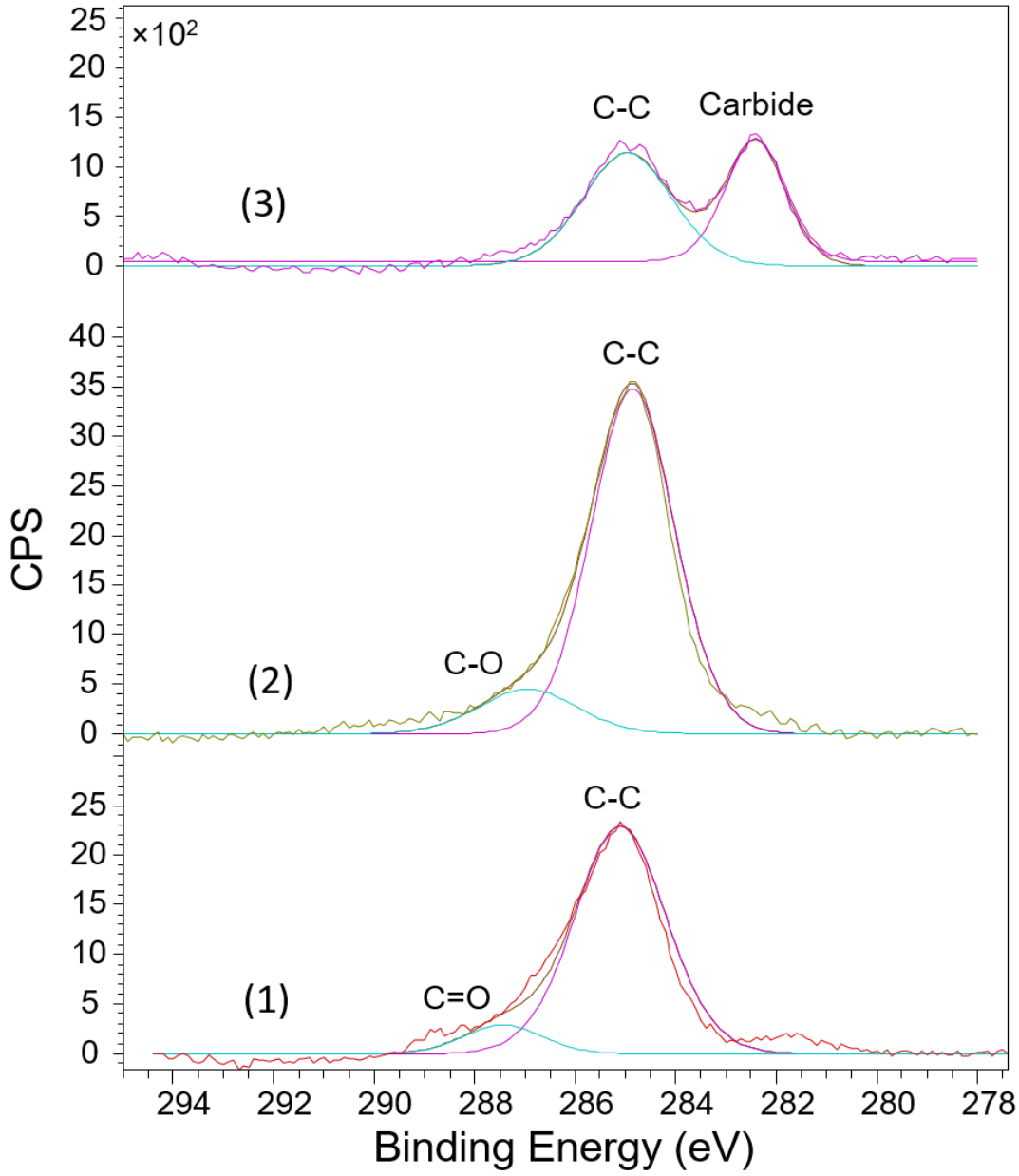

Figure 5-16 The C peak of XPS spectra of Ti on the SS (1) as-received, (2) after electron bombardment, (3) after heating treatment

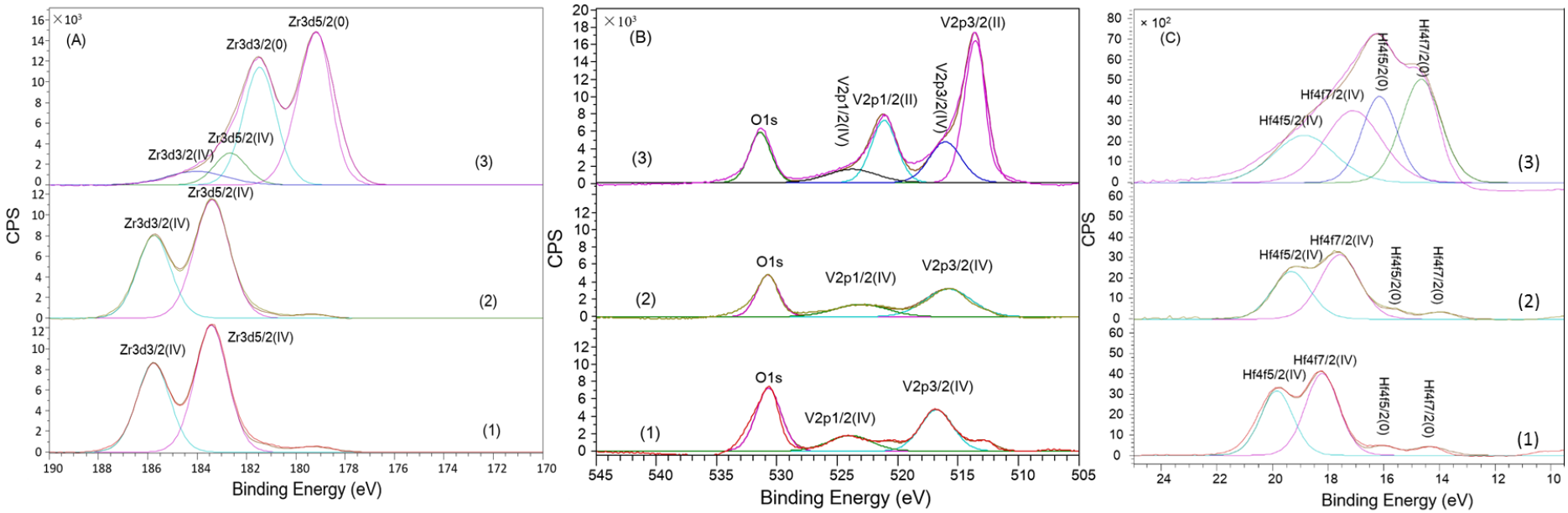

Figure 5-17 The spectra of Zr3d of Zr on the stainless steel (A) (1) as-received, (2) After electron bombardment, (3) After thermal treatment, V2p of V on the SS (B) (1) as-received, (2) After electron bombardment, (3) After thermal treatment and Hf4f of Hf on the stainless steel (C) (1)) as-received, (2) After electron bombardment, (3) After thermal treatment.

Table 5-5 The concentration of Zr, V and Hf on the stainless steel

Zr on the stainless steel	Zr3d5/2(0) 179.2 eV	Zr3d5/2(IV) 183.4 V
As-received		100%
After electron bombardment		100%
Heated to 250 ^{o}C for 2 hours	84.6%	15.4%
V on the stainless steel	V2p3/2(II) 512.4 eV	V2p3/2(IV) 516.0 eV
As-received		100%
After electron bombardment		100%
Heated to 350 ^{o}C for 2 hours	78.0%	22.0%
Hf on the stainless steel	Hf4f7/2(0) 14.7 eV	Hf4f7/2(IV) 18.3 eV
As-received		100%
After electron bombardment		100%
Heated to 350 ^{o}C for 3.5 hours	72.6%	27.4%

The XPS spectra of Zr peak for Zr on the stainless steel are shown in **Figure 5-17** (A) for as-received, electron bombardment and thermal treatment, respectively. The Zr3d5/2 peak of as-received Zr on the stainless steel are at the binding energy of 183.4 eV (Zr(IV) and Zr3d3/2 peak are at the binding energy of 185.8 eV (Zr(IV). Thus the Zr on the surface is at ZrO_2 oxide state for the as received thin film, and remains in the same oxide state even after electron bombardment. After heating treatments, the chemical state of Zr on the surface is one mixed stoichiometry ZrO_2 and sub stoichiometry oxide states with small percentage of metal Zr. The concentration of Zr3d5/2(0) at the binding energy of 179.2eV increase to 84.6% and Zr3d5/2(IV) reduced extremely to 15.6%, which indicate most of ZrO_2 has transferred to metal Zr.

The spectra of V2p of V and Hf4f of Hf on the stainless steel are shown in **Figure 5-17** (B) and (C) for both as-received, electron bombardment and thermal treatment, respectively. The surface of as-received V on the stainless steel is composed by VO_2. The V2p3/2 peak of V on the stainless steel is at the binding energy of 516.8 eV (V2p3/2(III)) and the V2p5/2 peak of V on the SS is at the binding energy of 524.0 eV (V2p1/2(IV)). After electron bombardment, the position of V2p3/2 and V2p5/2 peak does not change, which indicates that VO_2 still exists on the surface. After thermal treatment, The V2p3/2 peaks are at the binding energy of 513.6 eV (V2p3/2(0)), 516.4 eV (V2p3/2(IV)) and the

V2p1/2 peaks are at the binding energy of 521.0 eV (V2p1/2(0) and 524.1 eV (V2p1/2(IV)). The ratio of V2p3/2(0)) and V2p3/2 (III) are 78.0% and 22.0%, respectively. So the surface has a mixture of VO and VO_2. The surface of as-received Hf on the stainless steel is HfO_2. The Hf4f7/2 peak of Hf on the stainless steel is at the binding energy of 16.8 eV (Hf4f7/2(IV)) and the Hf4f5/2 peak of bulk Hf is at the binding energy of 18.3 eV (Hf4f5/2(IV)). After electron bombardment, the positions of Hf4f7/2 and Hf4f5/2 remain the same. So the HfO_2 still exists on the surface. After heating, the HfO_2 is still on the surface but it has dropped to 50% on the surface and metal Hf appears on the surface.

5.4 Non-evaporable getters

In this section, The SEYs of TiZrV coatings on the stainless steel and Si are studied and compared as a function of electron doses. The SEY of TiZrV coatings on the SS are also studied as a function of thermal treatments.

5.4.1 Ti-Zr-V coating on the stainless steel

Figure 5-18 shows the SEYs of the Ti-Zr-V on the stainless steel before and after thermal activation and further prolonged electron conditionings. The sample has been heated first and then conditioned by electron. The δ_{max} of the as-received Ti-Zr-V on the stainless steel is 1.82, then after heating to 250 ^{0}C for 2 hours and 300 ^{0}C for 1 hour it is reduced to 1.41 and 1.34, respectively. After prolonged electron conditioning of 5.3×10^{-3} C·mm^{-2}, δ_{max} dropped gradually to 1.10. **Figure 5-19** represents the high resolution SEM micrograph of Ti-Zr-V thin film deposited on stainless steel. The surface of Ti-Zr-V on stainless steel is roughly flat, however, from the cross section SEM graphs, it can be seen that the film is grown with columnar structure.

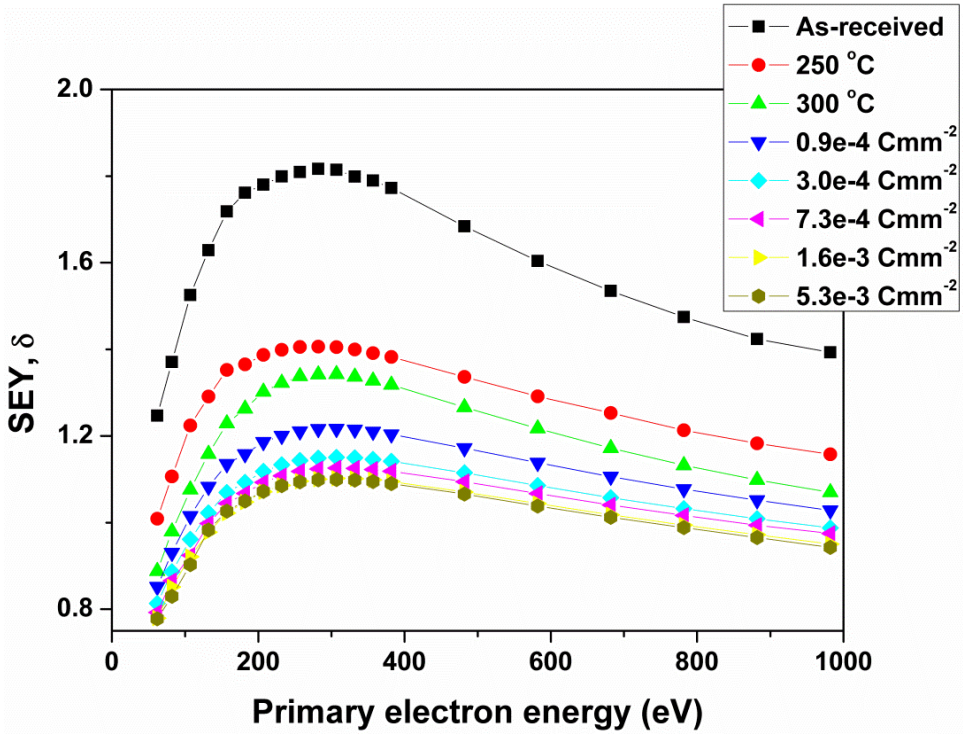

Figure 5-18 Reduction of δ(E) for Ti-Zr-V coating on the stainless steel substrate after thermal treatments and electron conditioning.

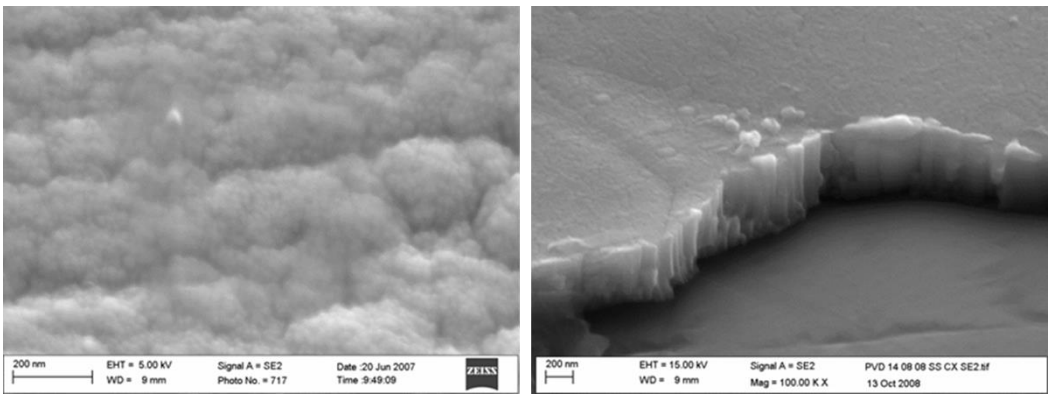

Figure 5-19 High resolution SEM micrograph of Ti-Zr-V thin film on stainless steel

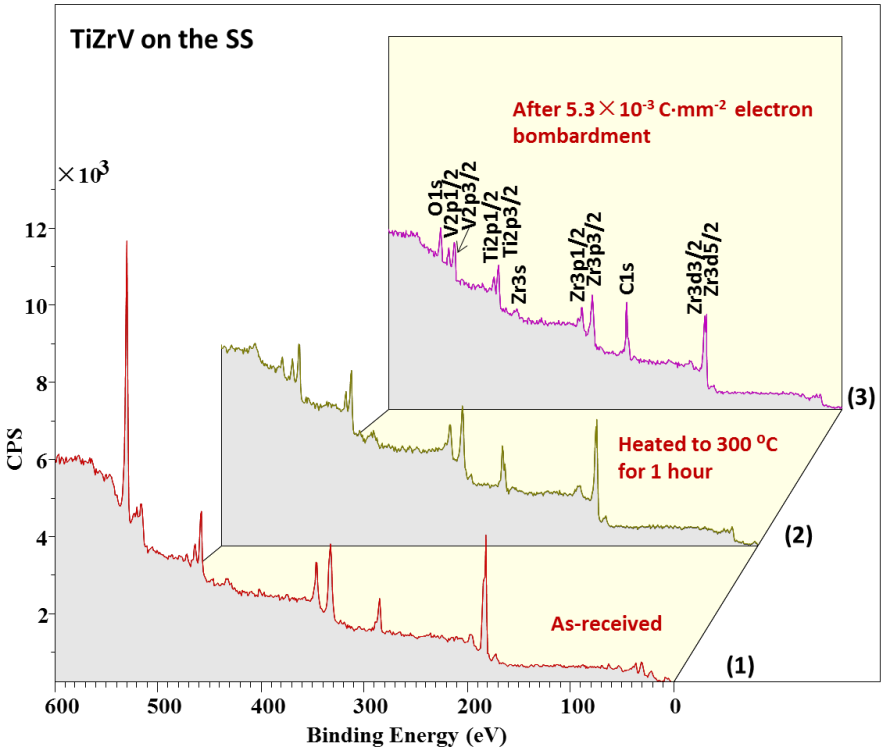

Figure 5-20 The XPS wide spectra of Ti-Zr-V on the stainless steel (1) as-received, (2) after thermal treatment to 300 ºC for 1 hour, (3) after an electron dose of 5.3×10^{-3} C·mm^{-2}

Figure 5-20 shows the surface chemical changes of Ti-Zr-V thin film deposited on stainless steel after thermal treatment and electron conditioning compared to as-received Ti-Zr-V thin film. It can be seen that the surface composition of the as deposited Ti-Zr-V samples consists of oxide of Ti, Zr and V as well as carbon-containing species as a consequence of air-exposure. The peak positions of Ti2p, Zr3d and V2p lines correspond to Ti in TiO_2, Zr in ZrO_2 and V in V_2O_5 bonding states. After heating to 300 ^{0}C, the surface oxides are reduced greatly and the oxygen is dissolved in the material bulk [1]. After further prolonged electron conditionings of 5.3×10^{-3} C·mm^{-2}, the carbon peak increases further.

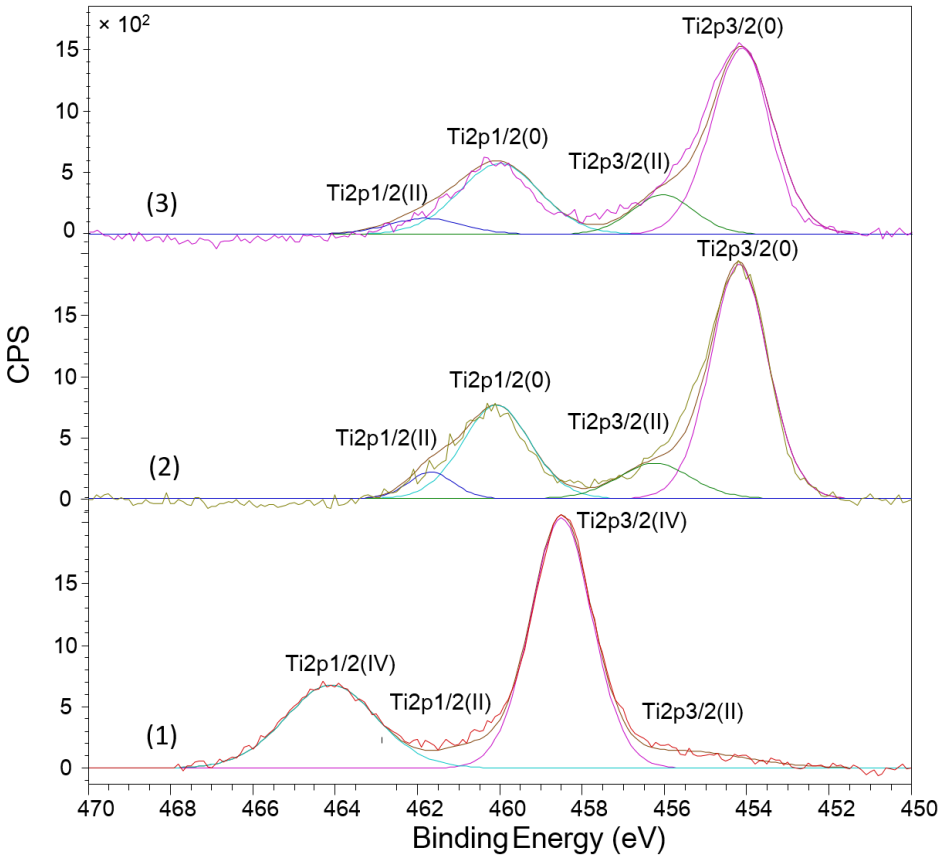

Figure 5-21 The Ti peak of Ti-Zr-V XPS spectra on the Stainless steel (1) as-received, (2) after thermal treatment to 300 °C for 1 hour, (3) an electron dose of 5.3×10^{-3} C·mm^{-2}

The region Ti2p spectra are shown in **Figure 5-21** for the as-received Ti-Zr-V surface, for thermally treated at 300 °C and subsequent conditioned at an electron dose of 5.3×10^{-3} C·mm^{-2}. The TiO_2 oxide state of as-received Ti-Zr-V on the stainless steel is located by the positions of Ti 2p3/2 and Ti 2p1/2 peaks at 458.5 and 464.2 eV, respectively. The ratio of Ti2p3/2(IV) and Ti2p1/2(0) is 87.7% and 13.3% shown in **Table 5-6**. After annealing at 300 °C, oxide state turns to metal state and the positions of Ti 2p3/2 and Ti 2p1/2 peaks are shift to low binding energy, 454.1 and 460.1 eV, respectively. It indicates that the Ti in the oxide state was transformed to Ti-Ti bonding states and almost fully activated after thermal treatment. But a small amount of sub-oxides (Ti(II)) still remains on the surface at the binding energy of 456.3 and 461.7 eV, respectively. The ratio of Ti2p3/2(II) and Ti2p1/2(0) is 84.0 and 16.0%. After electron conditioning, the positions of Ti 2p stayed the same.

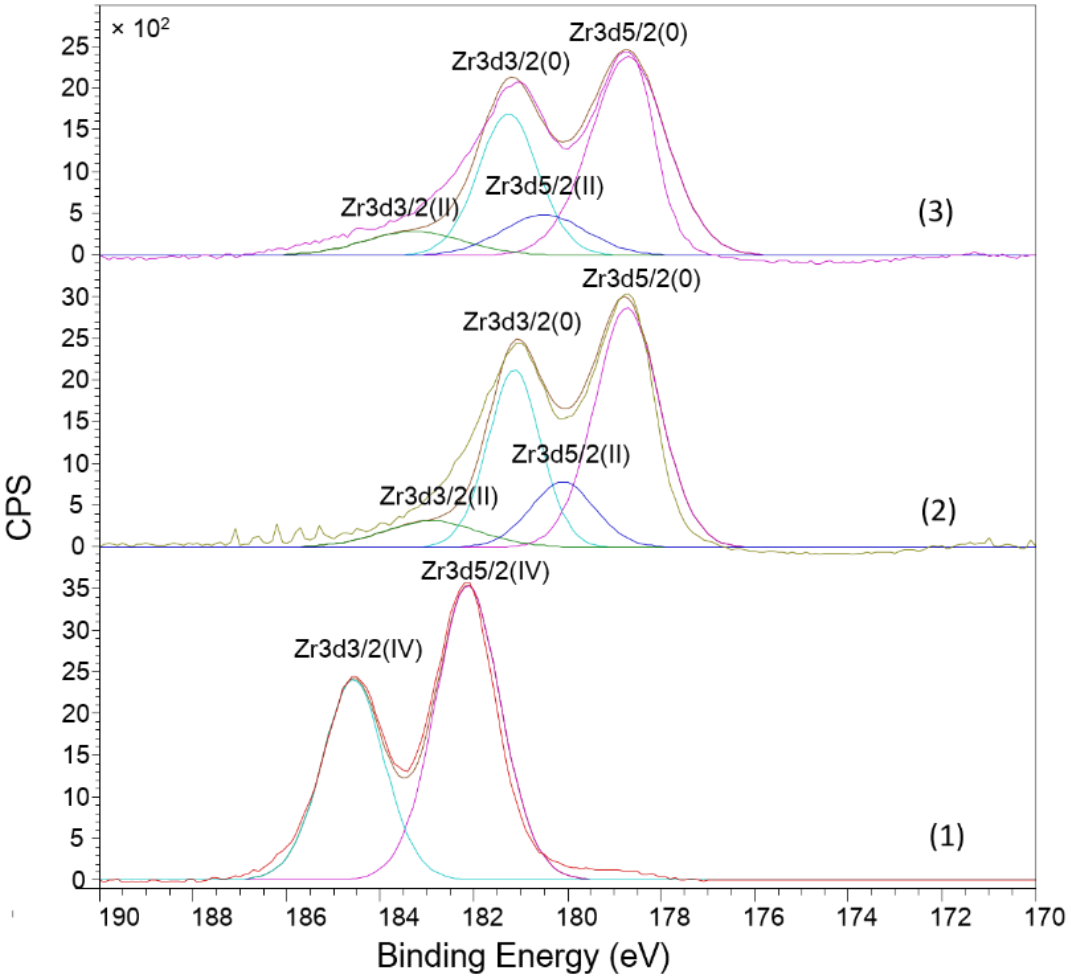

Figure 5-22 The Zr peak of Ti-Zr-V XPS spectra on the stainless steel (1) as-received, (2) after thermal treatment to 300 °C for 1 hour, (3) an electron dose of 5.3×10^{-3} C·mm^{-2}

In **Figure 5-22**, the region spectra of Zr 3d are shown for the as deposited Ti-Zr-V on the stainless steel, for thermal treated at temperatures indicated and for that conditioned by electron bombardment at 500 eV at a dose of 5.3×10^{-3} C·mm^{-2}. In the case of the as-deposited film, the ZrO_2 oxide state is evidenced by positions of the Zr 3d5/2 and Zr 3d3/2 peaks located at 182.0 and 184.5 eV, respectively. After thermal treatment at 300 ^{0}C, a mixture of metalic Zr and ZrO appear on the surface which means Zr has only been partially activated. The positions of Zr 3d5/2(II) and Zr 3d5/2(0) is at the binding energy of 180.0 eV and 178.3 eV and the positions of Zr 3d3/2(II) and Zr 3d3/2(0) is at the binding energy of 181.0 eV and 183.0 eV, After an electron dose of 5.3×10^{-3} C·mm^{-2}, the positions of Zr 3d doublet stays the same. The ratio of Zr 3d5/2 of different oxide state is shown in **Table 5-6**.

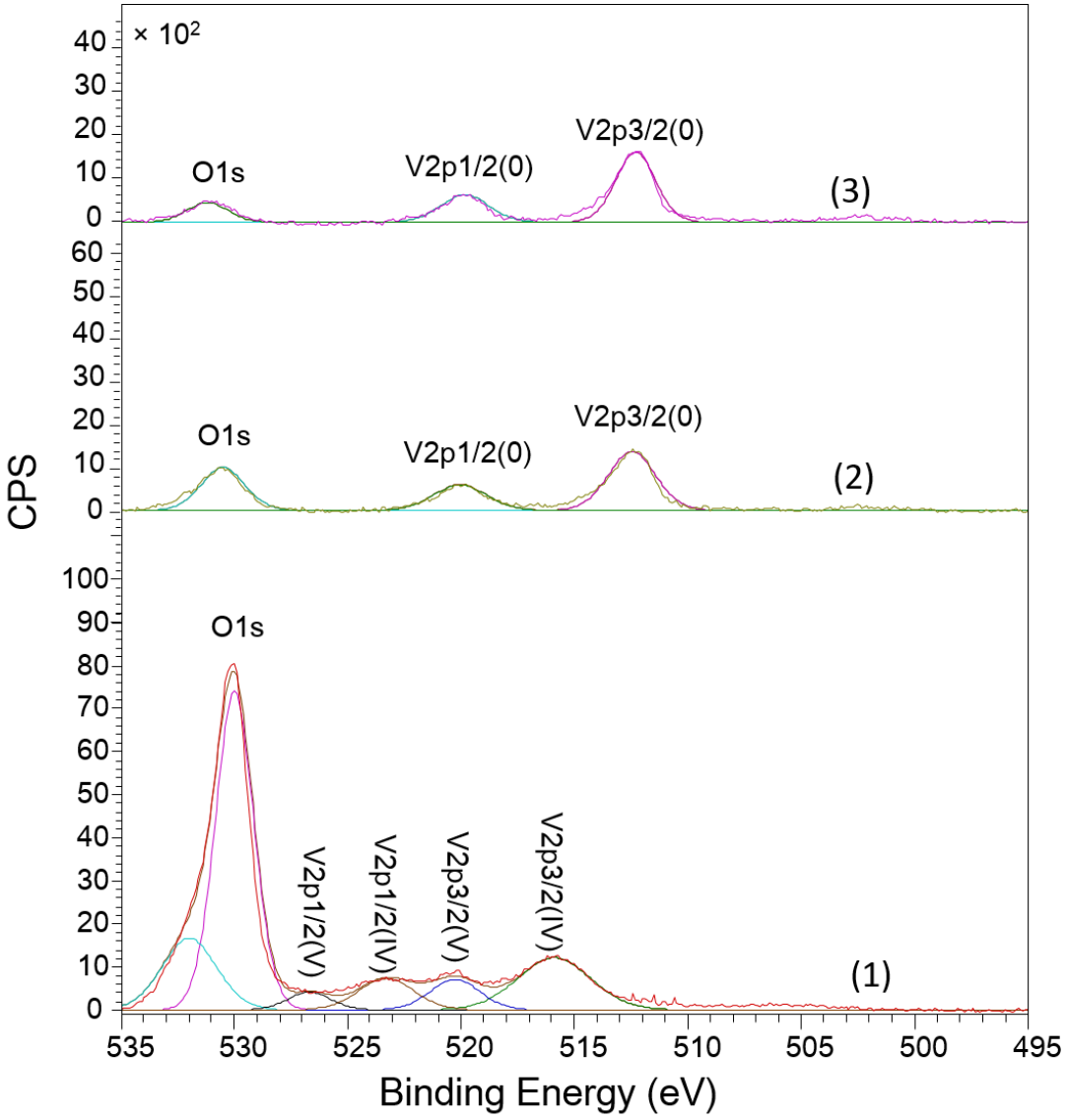

Figure 5-23 The V peak of Ti-Zr-V XPS spectra on the Stainless steel (1) as-received, (2) after thermal treatment to 300 °C for 1, (3) an electron dose of 5.3×10^{-3} C·mm^{-2}

Similarly as Zr 3d spectra, **Figure 5-23** displays the V 2p spectra for the as deposited Ti-Zr-V on stainless steel, for that of annealed at temperatures indicated and for that conditioned by electron at a dose of 5.3×10^{-3} C·mm^{-2}. There is a mixture of VO_2 and V_2O_5 on the as deposited surface. The V 2p3/2 and V 2p1/2 peaks are in their VO_2 state at the position of 516.0 and 522.1 eV, respectively. The V 2p3/2 and V 2p1/2 peaks are in their V_2O_5 state at the position of 520.0 and 526.8 eV respectively. The proportions of V associated with each type of vanadium oxide (V_2O_5 and VO_2) are 71.4% and 28.6%, respectively, shown in **Table 5-6**. After thermal treatment, the V component in TiZrV has been fully activated and the V 2p3/2 and 2p1/2 peaks are shifted to

512.2 and 520.2 eV, respectively. Even after electron conditioning, the V 2p peaks stay the same.

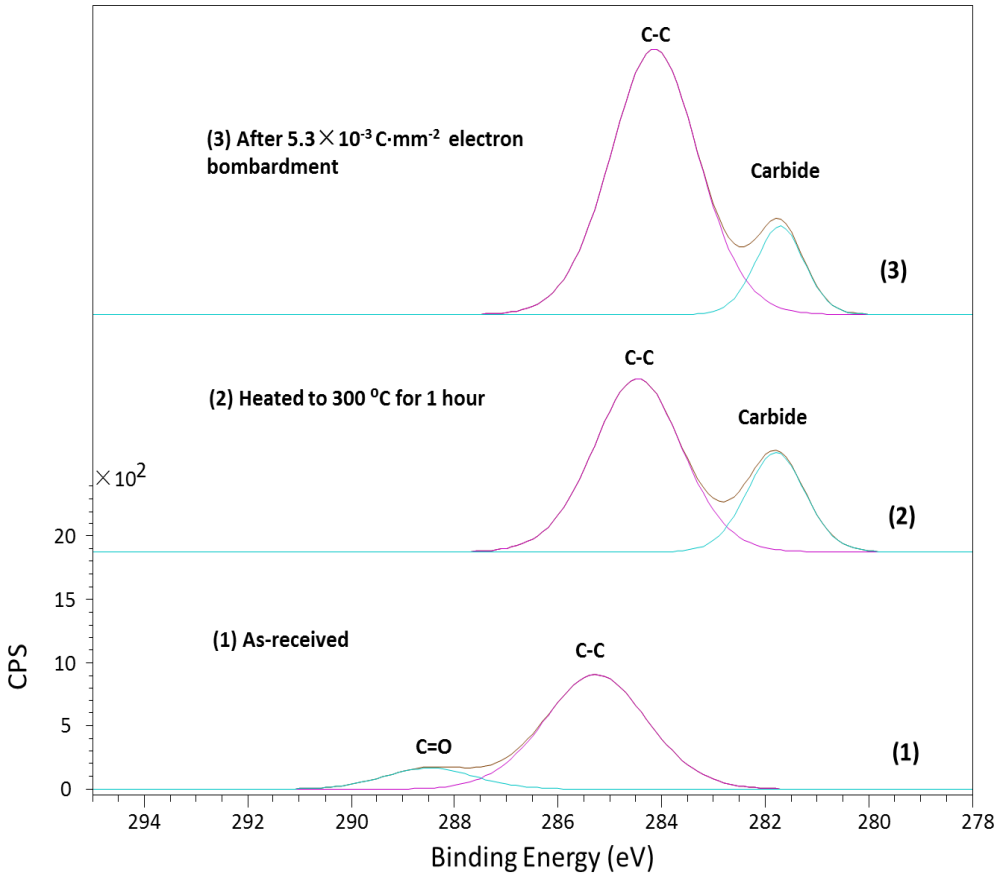

Figure 5-24 The C peak of Ti-Zr-V XPS spectra on the Stainless steel (1) as-received, (2) after thermal treatment to 300 °C for 1 hour, (3) an electron dose of 5.3×10^{-3} C·mm^{-2}

The region XPS of carbon peak obtained for the Ti-Zr-V on the stainless steel during the thermal treatment and electron conditioning are shown in **Figure 5-24**. The C1s peak of the as-received Ti-Zr-V can be deconvoluted into two separate peaks, with the main peak at BE of 285.2 eV, which can be attributed to C atoms in C-C and C-H bonds and a weak component at 288.6 eV ascribed to C=O bonds which can be decomposed into weakly hydro-carbon and into a graphitic component at 284.3 eV. The 281.6 eV BE peak is a typical metal carbide state, which is always present after a fully successful activation [9]. Then after long further electron conditioning, the area under the graphitic carbon peak increases. The intensity of carbide and the other metal peaks decreases as the graphite carbon layer forms on the surface. But the position of C1s peak stays the same.

Table 5-6 The concentration of Ti-Zr-V on the stainless steel

TiZrV on the SS	As-received	Heated to 300 °C for 1 hour	Electron bombardment
Ti 2p3/2			
Ti2p3/2(0) 454.1 eV		84.0%	82.4%
Ti2p3/2(II) 456.3 eV	12.3%	16%	17.6%
Ti2p3/2(IV) 458.5 eV	87.7%		
Zr 3d5/2			
Zr3d5/2(0) 178.3 V		78.6%	81.4%
Zr3d5/2(II) 180.0 eV		21.4%	18.6%
Zr3d5/2(IV) 182.0 eV	100%		
V2p3/2			
V2p3/2(0) 512.2 eV		100%	100%
V2p3/2(IV) 516.0 eV	28.6%		
V2p3/2(V) 520.0 eV	71.4%		

5.4.2 Ti-Zr-V on Si

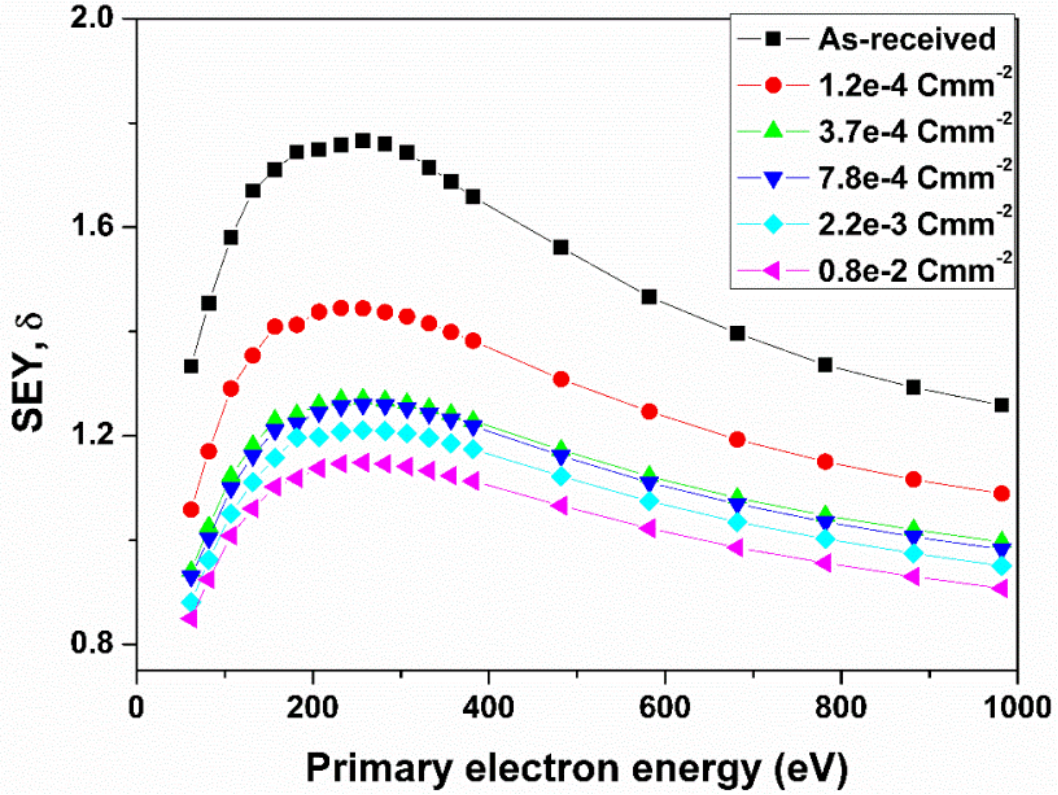

Figure 5-25 Reduction of δ(E) after conditioning with various electron doses for Ti-Zr-V on Si substrate.

In **Figure 5-25**, the SEYs of as deposited Ti-Zr-V on Silicon are plotted as a function of primary electron energy showing variation with electron dose. The δ_{max} of as-received Ti-Zr-V on Silicon is 1.77 and it is reduced gradually after

prolonged electron conditioning. It drops to 1.45, 1.27, 1.26, 1.21, 1.15 with the continuous electron bombardments of 1.2×10^{-4} C mm^{-2}, 3.7×10^{-4} C mm^{-2}, 7.8×10^{-4} C mm^{-2}, 2.2×10^{-3} C mm^{-2}, and 0.8×10^{-2} C mm^{-2}, respectively. Similarly to Ti-Zr-V on the stainless steel, the influence of electron conditioning in the reduction SEY is more obvious by the initial electron dose than the following electron doses.

Figure 5-26 represents the surface chemical composition of thin film deposited on silicon for the as deposited and subsequent electron conditioning. It reveals that in both cases the surface composition consists of C1s, O1s, Ti2p, Zr3p, Zr3d and V2p peaks. The elemental region spectra of Ti-Zr-V coatings as a function of electron bombardments are shown from **Figure 5-27** to **Figure 5-30.** The bonding energies of $Ti2p_{3/2}$ peak are at 458.8 (Ti2p3/2(IV)) which exhibits the presence of TiO_2 on the as deposited Ti-Zr-V surface. The bonding energies of $Zr3d_{5/2}$ peak are at 182.4 ($Zr3d_{5/2}$ (IV) which exhibits the presence of ZrO_2 on the as deposited Ti-Zr-V surface. Furthermore the vanadium at the surface is composed of a mixture of V_2O_5 and V_2O_3. After prolonged electron bombardment, the Ti2p, Zr3d and V2p peaks stay the same. But the concentration of the two oxide states for each element has changed slightly as shown in

Table 5-7. After electron bombardment, the V2p3/2(IV) increases from 21.8% to 30.9% and the V2p3/2(III) decreases from 78.2 to 69.1%, which means the proportion of oxidized V_2O_3 on the surface has transformed into VO_2. The as-received C1s peak could be deconvoluted into C-H at 285.0 eV, and C=O double bond at 289.0 eV. After an electron bombardment dose of 0.8×10^{-2} $C\cdot mm^{-2}$, the main C1s peak is shifted to 284.4 eV which is related to C-C bonds (graphitic carbon). Also CO single bond is still left on the surface at 286.4 eV but the height is much lower than the graphitic carbon.

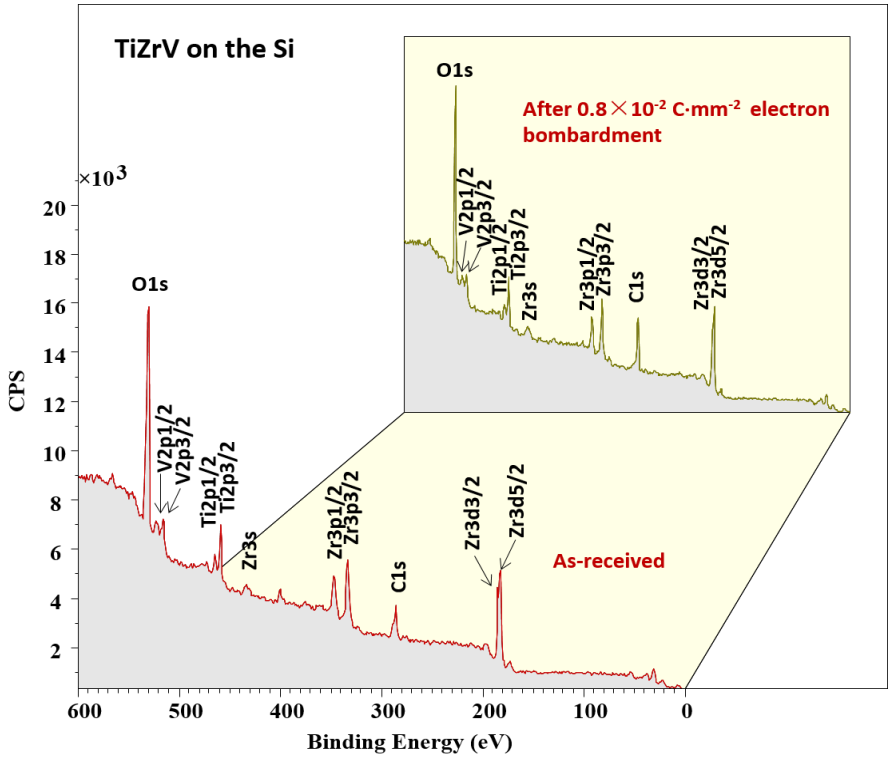

Figure 5-26 The XPS spectra of as-received and electron bombarded Ti-Zr-V on silicon

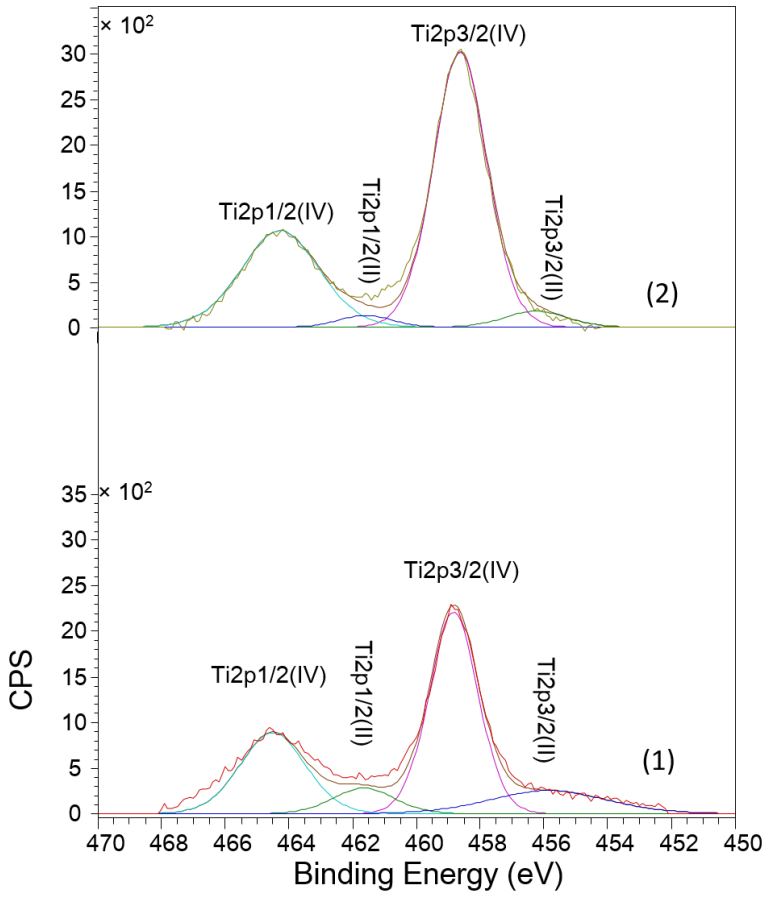

Figure 5-27 The Ti2p peak of as-received and electron conditioned Ti-Zr-V XPS spectra on silicon

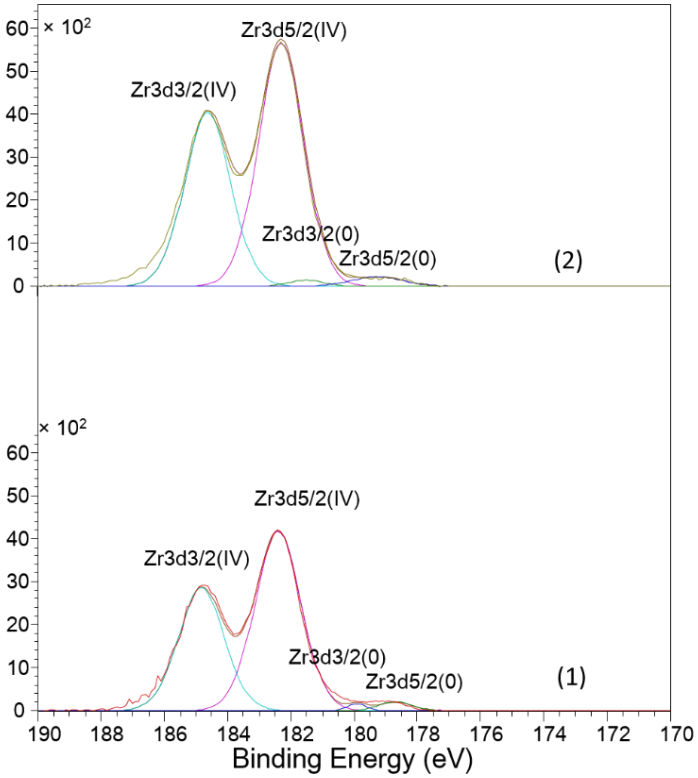

Figure 5-28 The Zr3d peak of as-received and electron conditioned Ti-Zr-V XPS spectra on silicon

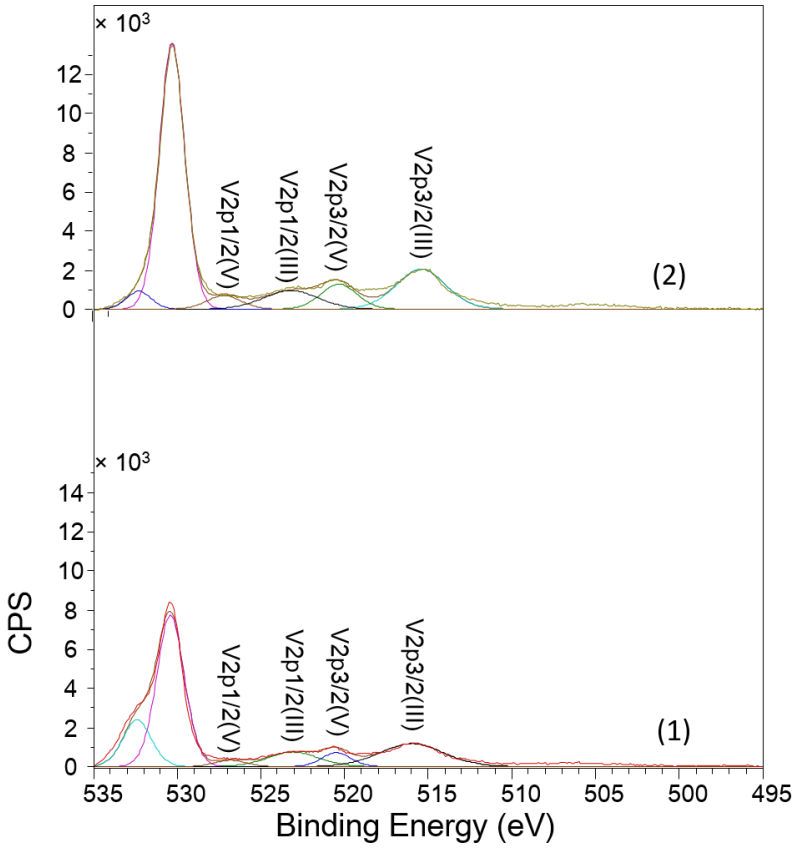

Figure 5-29 The V2p peak of as-received and electron conditioned Ti-Zr-V XPS spectra on silicon

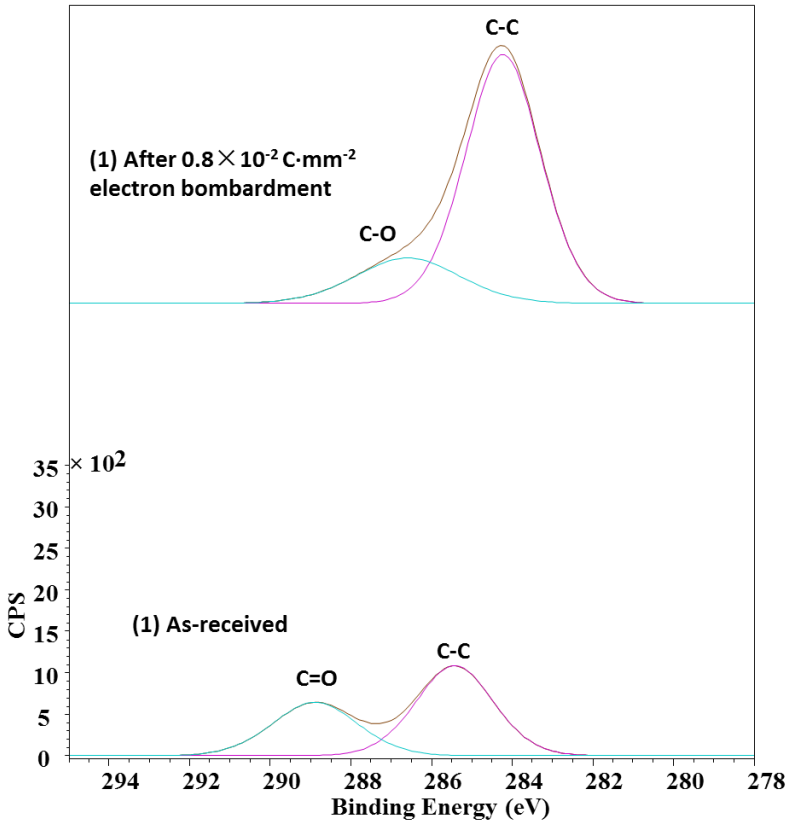

Figure 5-30 The C1s peak of as-received and electron conditioned Ti-Zr-V XPS spectra on silicon

Table 5-7 The concentration of Ti-Zr-V on Si

TiZrV on Si	As-received	Electron bombardment
Ti 2p3/2		
Ti2p3/2(IV) 458.8 eV	100%	100%
Zr 3d5/2		
Zr3d5/2(IV) 182.4 eV	96.5%	95.6%
V2p3/2		
V2p3/2(III) 515.9 eV	78.2%	69.1%
V2p3/2(V) 520.5 eV	21.8%	30.9%

5.5 Discussion

Secondary electron emission is a surface process which is influenced by slight modifications of a material's outer layers [10]. These factors include the surface topography, surface composition and surface chemistry/contamination (oxidation layers and adsorbed gases) and cleaning process. So it is important to actually measure the yield of the material itself, but not the yield from the contaminants on the surface.

Water vapour and other contaminations on the surface lower the surface barrier

for escaping secondary electrons [11], and then raise the SEY. Surface heating can remove the adsorbed gases and oxidation layers from the surface. The XPS results in this chapter show clearly that metal oxide has been removed and the surface has transformed to the metal state via oxygen diffusing into the bulk. By heating, the oxygen on the surface diffuses into the bulk via the grain boundaries and the surface transforms from an oxide to a metallic state. Hence, an obvious change of SEY is expected. For example, the SEY of the bulk Ti dropped from 2.30 to 1.40 after heating to 350 ^{0}C for 2.5 hours. Also, Over 50% of Ti2p3/2 peaks moved to the direction of metallic Ti to the binding energies of 454.7 eV. Similarly, after 300 ^{0}C heating, the SEY of Ti-Zr-V on the SS drops to 1.34 from 1.82 for as-received sample. All the Ti, Zr and V peaks have moved towards the metal state. Ti element has been almost activated and V peak has been fully activated. However, Zr peak has only been partially activated. The reason may be related to the BCC structure of V and different chemical bonds.

Efforts have been made to understand the effect of electron beam bombardment on Cu, stainless steel and Al at the Standford Linear Accelerator Center (SLAC) [12], at the European Organization for Nuclear Research (CERN)[13] and the Material Science INFN-LNF Laboratory of Frascati (RM) [7] and so on. After further long electron bombardments, carbon content increases due to the electron-induced carbon deposit by cracking the carbon-containing residual gas molecules at the sample surface. The electron conditioning is accompanied by a clear chemical modification and produces a graphite-like layer coating on the surface. The surfaces undergo a graphitization process resulting in a decrease of the SEY value [7]. So for example after further electron conditioning, the δ_{max} of Ti-Zr-V on Si is decreased from 1.77 to 1.15. The graphite-like layer can be produced both on the as-received surface and heated clean surface. After electron bombardment, the SEY of the thermally treated sample is reduced further. For example, the δ_{max} of heated Ti-Zr-V on the stainless steel is 1.34. After an electron dose of 5.3×10^{-3} C·mm^{-2}, it dropped to 1.10. From the XPS spectrum of C, the intensity of graphite-like carbon has been increased (the ratio of $\frac{C_{After\ electron\ bombardment}}{C_{Before\ electron\ bombardment}}$ = 1.38) after electron bombardment.

Some researchers also explain that the reduction of the SEY yield after continual electron bombardment is attributed to conversion of high-SEY oxides to scatter-enhancing suboxides [7, 10]. From the XPS results of Ti on the SS we obtained, the concentration of Ti2p3/2 (IV) after electron bombardment reduced from 77.0% to 68.2% and the concentration of the Ti2p3/2 (III) and Ti2p3/2(0) increase to 22.1% and 9.2%, respectively. This means that oxygen on the surface is slightly reduced by long electron conditioning. The electron bombardment breaks the Ti-O bonds into low SEY defective suboxide [5] and at the same time deposits carbon on the surface by cracking the CO and CO_2. The SEY of semiconducting metal oxides is often lower than that of the parent metals, such as CuO, NbO [4, 5]. Also the surface builds up a predominant graphtic carbon network after electron bombardments. So by combination of these two reasons, the surface SEY is much lower after electron bombardment than that of the as-received.

Besides by modifying the surface chemistry, the SEY also increases with the Z atomic number and density. For example, the SEYs of as-received bulk Ti, Zr, V and Hf are higher than that of as-received Ti, Zr V and Hf coatings on the stainless steel because the density of bulk samples are higher than that of thin films. Also the SEY of as-received V, Ti, Zr, and Hf on the SS is 1.58, 1.74, 2.23 and 2.34. Hf (72, 13.31 g/cm^3) has the largest SEY as it has the largest atomic number and highest density in these four samples.

The SEY of Ti-Zr-V coating is 1.82, which is almost the average of the SEY of the individual metal (1.85). Equation 2-10 represent the theory calculation for secondary electron emission from a material. A (in equation 2-7) is a constant characteristic related to the material property. The fitting based on this equation has shown from **Figure 5-31** to **Figure 5-34**. The purpose for these fittings is to find out the relations between the individual metal and alloys. Then this may explain the reason that the SEY of Ti-Zr-V coating is almost average of the SEY of the individual metal. Although this equation is semi-empirical, the fittings coincide with the measured results quite well. A (127.27) for Ti-Zr-V on the stainless steel is almost the same as the average of A (130.48) for Ti, Zr and V on the stainless steel. A as a constant material characteristic might affect the

SEY value of the materials. So the SEY of Ti-Zr-V coating is almost average of the SEY of the individual metal. The fitting after thermal treatment for Ti, Zr and V thin films and Ti-Zr-V alloys coatings have been described in **Figure 5-35** to **Figure 5-38**. The SEY of Ti-Zr-V on the stainless steel is 1.34, which is higher than the average of the SEY of the individual metal (1.0). Similary, A (74.81) for Ti-Zr-V on the stainless steel is different with the average of A (40.34) for Ti, Zr and V on the stainless steel. The reason of this difference is that the thermal treatment will change the surface concentration. So the A is not the average of that for Ti, Zr, and V.

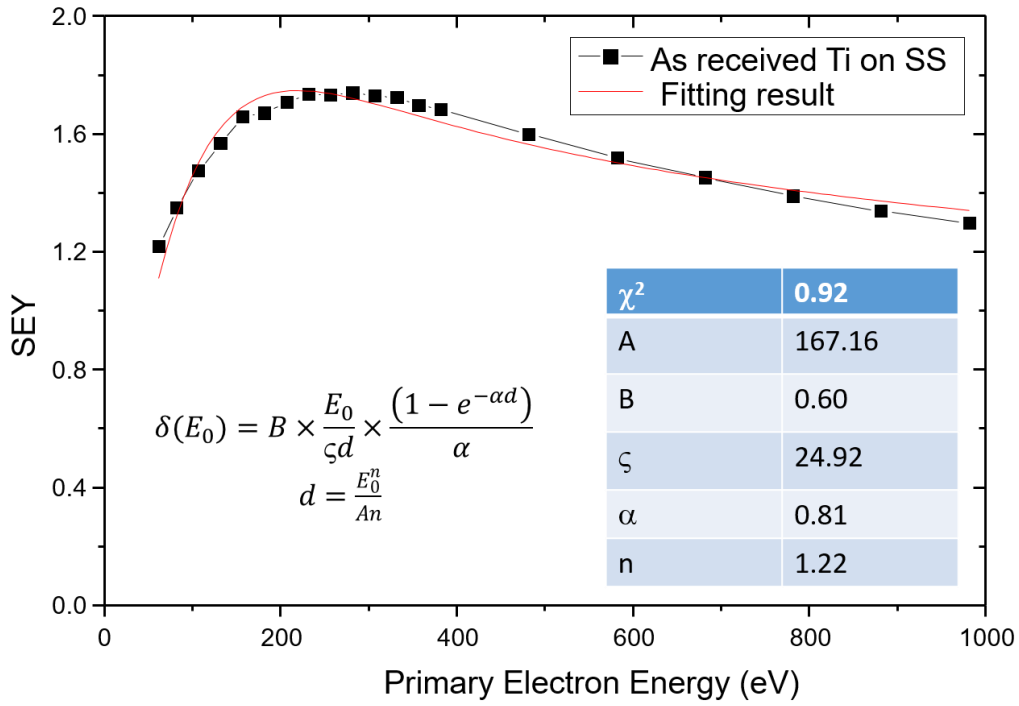

Figure 5-31 The SEY curve and its fitting on as-received Ti on the stainless steel based on the Eq. (2-10)

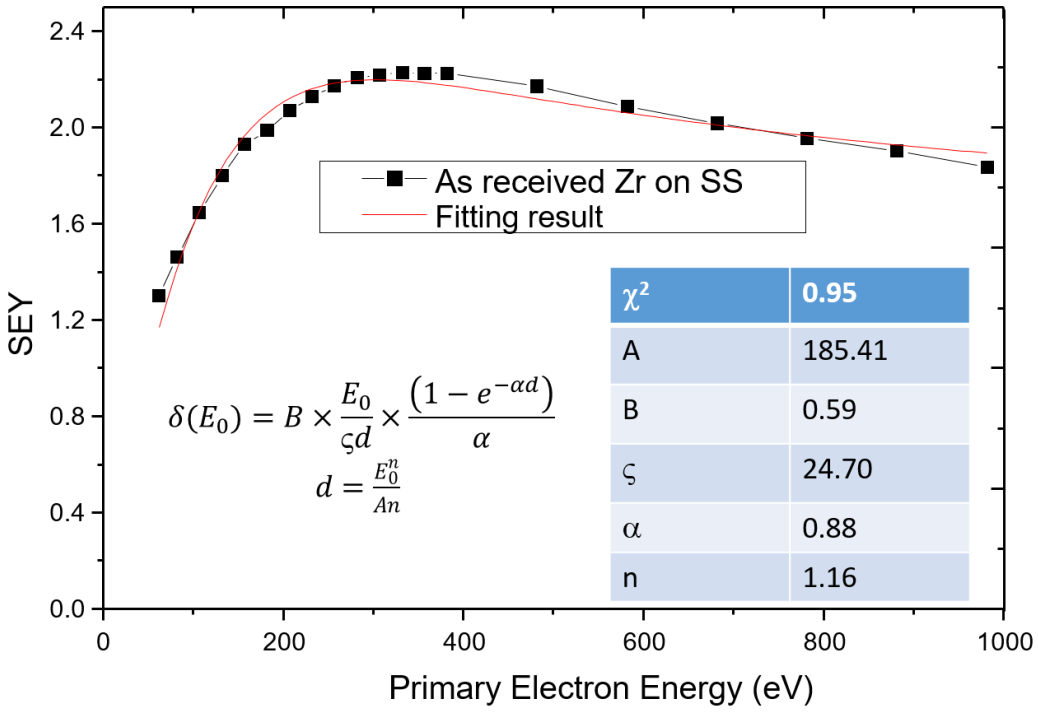

χ^2	0.95
A	185.41
B	0.59
ς	24.70
α	0.88
n	1.16

Figure 5-32 The SEY curve and its fitting on as-received Zr on the stainless steel based on the Eq.(2-10)

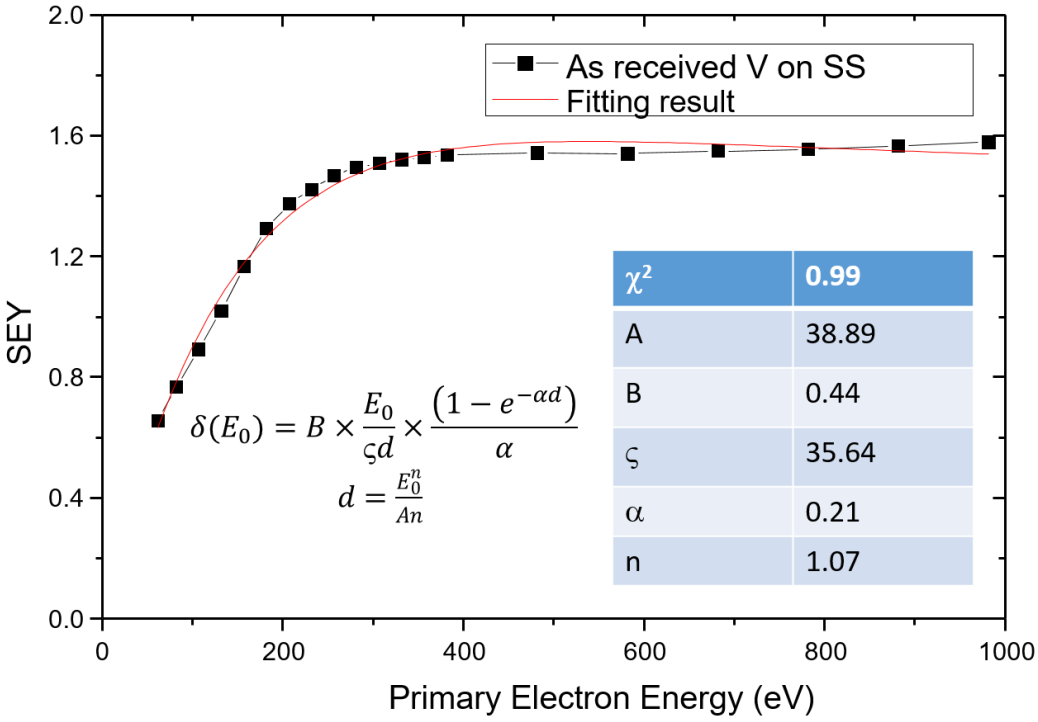

χ^2	0.99
A	38.89
B	0.44
ς	35.64
α	0.21
n	1.07

Figure 5-33 The SEY curve and its fitting on as-received V based on the Eq.(2-10)

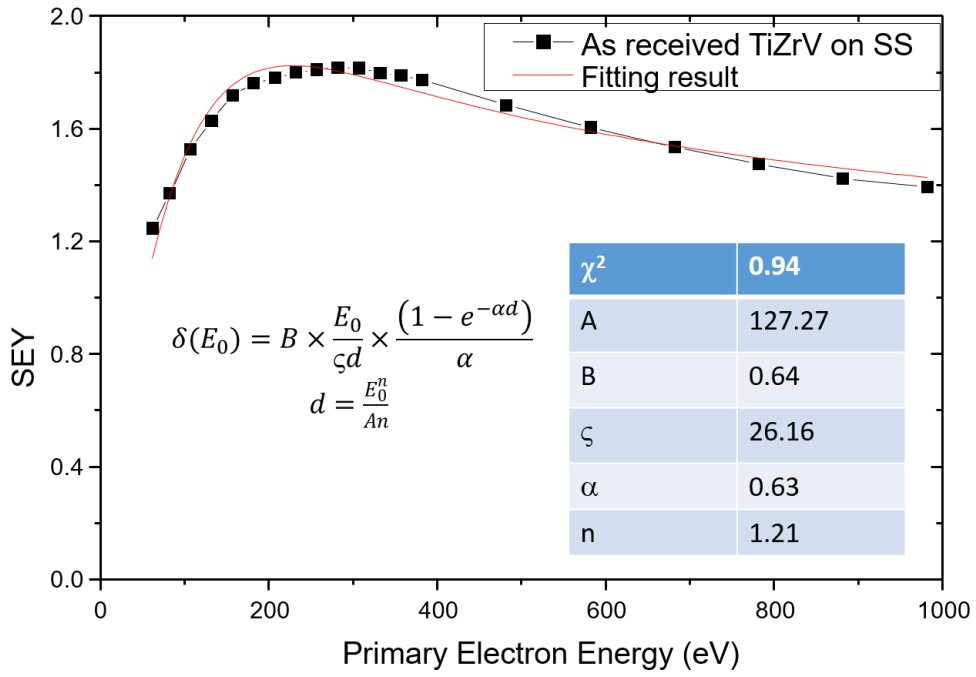

Figure 5-34 The fitting on as-received TiVZr on the stainless steel based on the Eq. (2-10)

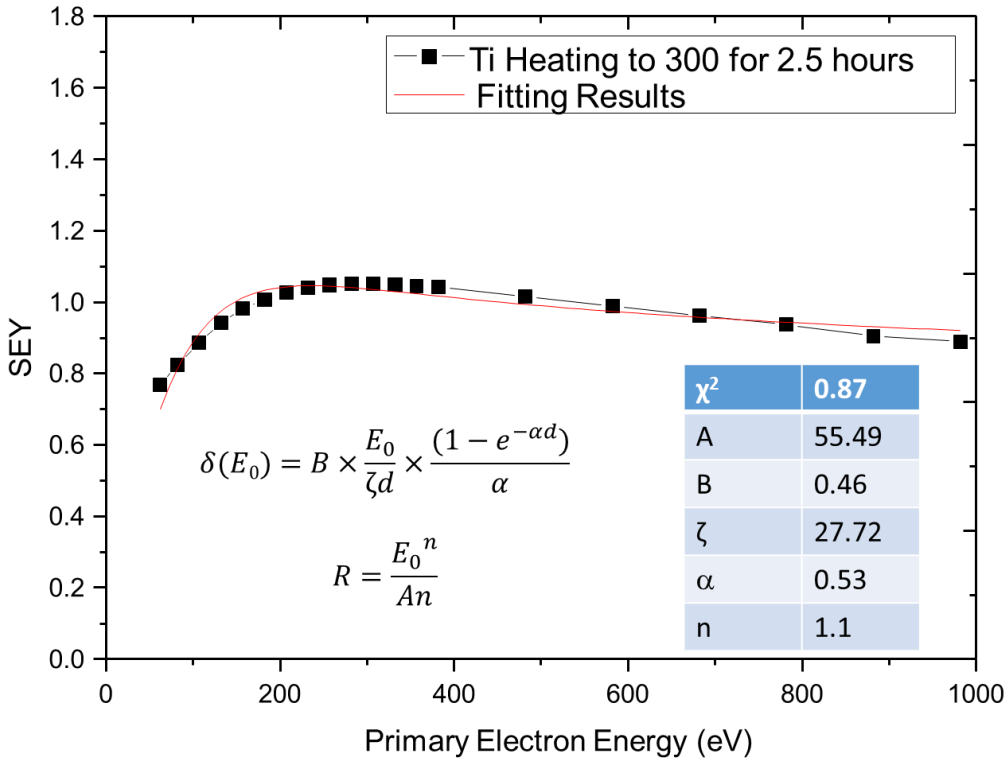

Figure 5-35 The fitting on heated Ti on the stainless steel based on the equation 2-10

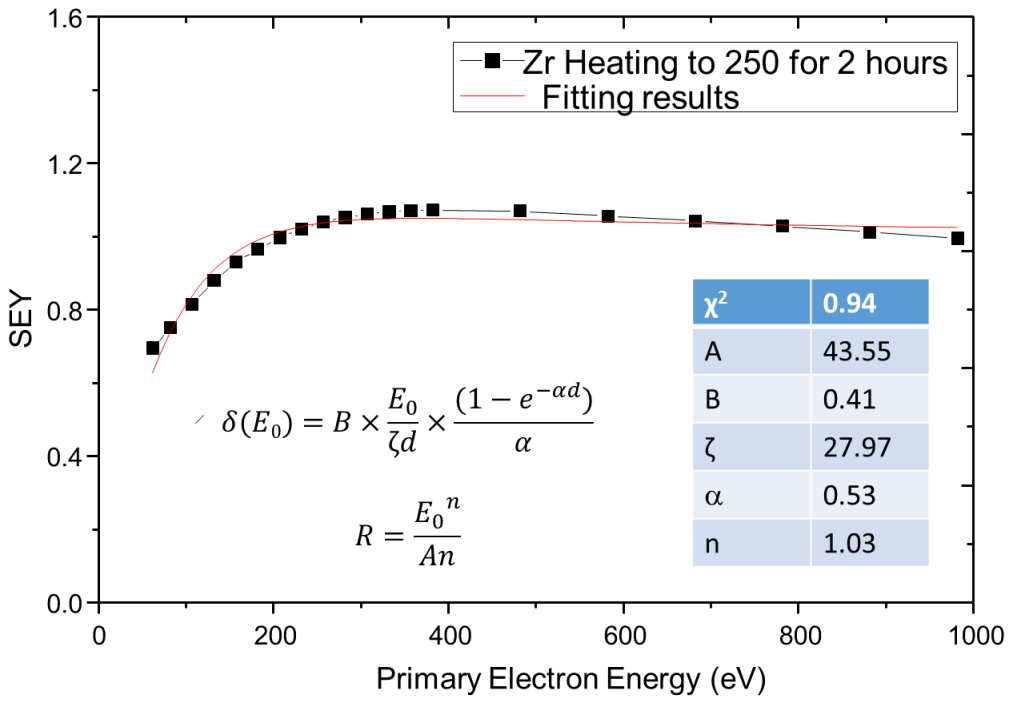

Figure 5-36 The fitting on heated Zr on the stainless steel based on the Eq.(2-10)

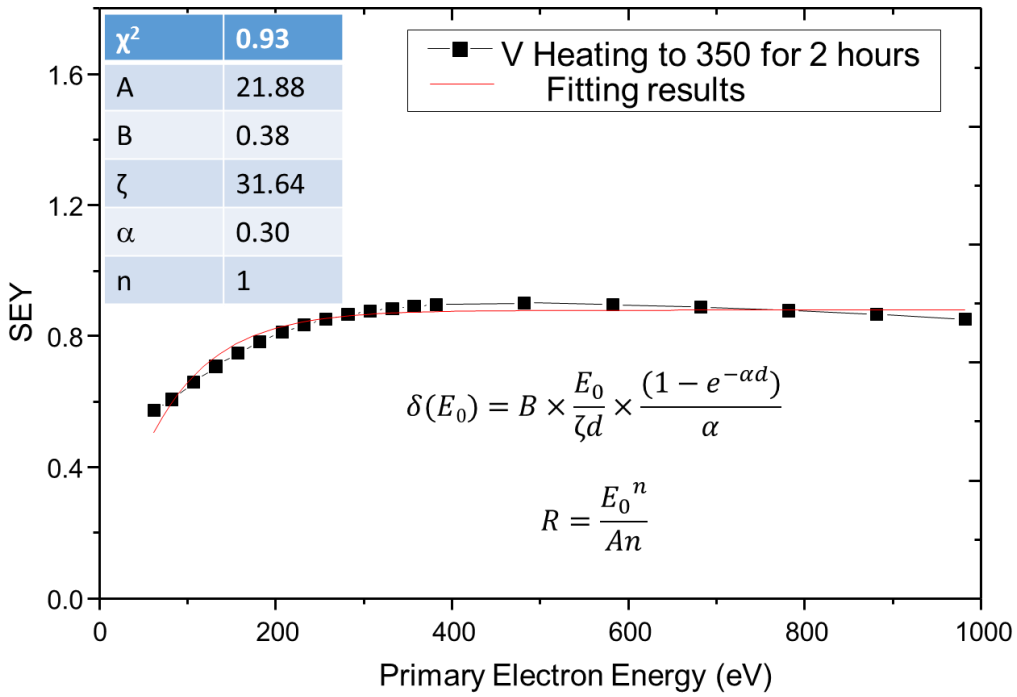

Figure 5-37 The fitting on heated V on the stainless steel based on the equation 2-10

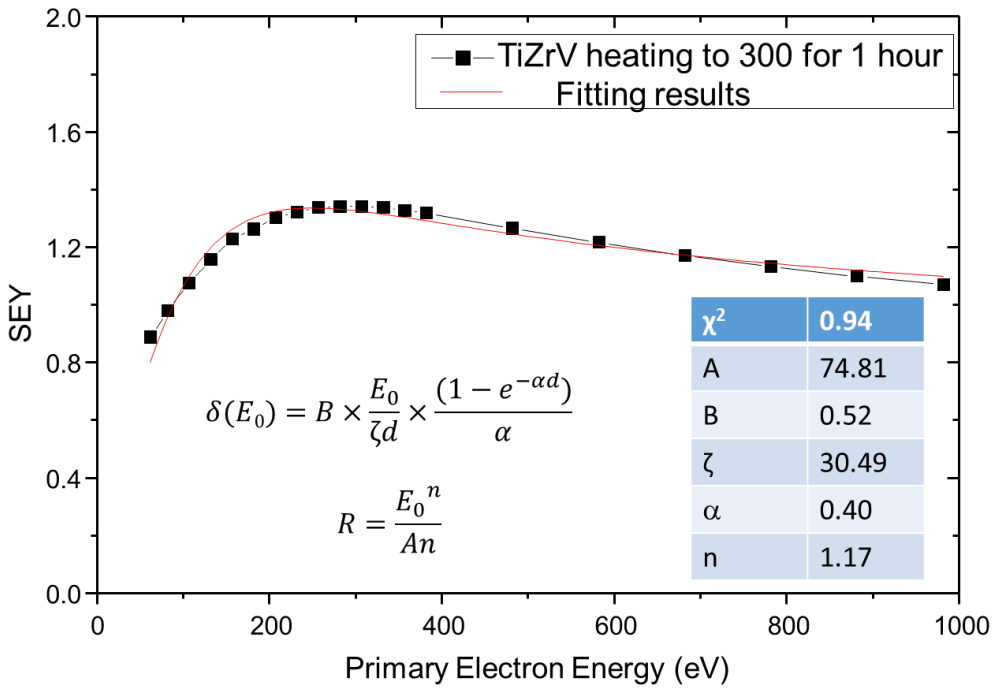

Figure 5-38 The fitting on heated TiZrV on the stainless steel based on the equation 2-10

5.6 Conclusions

In this chapter, SEY of transition metals and their coatings have been studied as a function of electron conditioning and thermal treatment alongside with XPS analysis before and after each treatment. The δ_{max} of as-received bulk Ti, Zr, V and Hf were 2.30, 2.31, 1.72 and 2.45. Because the δ_{max} correlates with the elemental atomic number Z, Hf with highest atomic number value has the highest δ_{max}. However, the δ_{max} of V has the lowest value. After 7.9×10^{-3} C·mm^{-2} for Ti, 6.4×10^{-3} C·mm^{-2}, 1.3×10^{-3} C·mm^{-2} and 5.2×10^{-3} C·mm^{-2}, the δ_{max} decrease to 1.19, 1.27, 1.48 and 1.40. After long electron bombardments, carbon was produced on top of the surface due to the electron-induced carbon deposit by cracking the carbon-containing residual gas molecules. XPS analysis showed that as-receive bulk Ti, Zr, V and Hf were a contaminated oxidized surface. But after electron bombardments, the graphitic carbon increased on the surface for all the bulk transition metals. The SEY reduced after electron bombardment due to the produce of graphitic carbon. The concentration of Ti2p3/2 (IV) for bulk Ti after electron bombardment reduced from 70.5% to 59.9% and the concentration of the Ti2p3/2 (III) and Ti2p3/2(0) increase to 26.4% and 18.2%, respectively. This means that oxygen on the

surface is slightly reduced by long electron conditioning. The reduction of the SEY yield after continual electron bombardment also may be attributed to conversion of high-SEY oxides to scatter-enhancing suboxides. The SEY of bulk Ti after heating to 350 ^{0}C for 2.5 hours has dropped to 1.21. XPS showed that Ti2p3/2 and Ti2p1/2 peaks shifted to lower binding energy with higher intensity. This means that the surface has transferred to the metal state. Oxygen diffused into the bulk after heating via the grain boundaries. Surface heating can remove the absorbed gases and oxidation layers, hence, there is an obvious change of SEY.

The SEY of as-received V, Ti, Zr, and Hf on the SS is 1.58, 1.74, 2.23 and 2.34, separately. Hf (72, 13.31 g/cm^{3}) has the largest SEY as it has the largest atomic number. SEY also increases with density. The SEM graphs of both bulk transition metal and coatings show the surfaces are very flat. However, the SEY of the as-received transition coatings is lower than those of bulk samples because the density of coatings is lower than that of bulk materials. After thermal treatments and electron conditioning, SEY of Ti, Zr, V and Hf decreases, which are similarly with bulk samples. XPS results also showed the absorbed gases and oxidation layer removed from the surface after heating. After electron bombardment, there is a graphitic layer increased on the surface.

TiZrV coatings on the stainless steel and the Si were produced by PVD with same parameters. The SEYs of both samples are almost the same (about 1.80). The SEM graphs showed the surface of both samples are flat and XPS analysis showed that the surfaces are covered by oxidation layer for both samples. TiZrV coating on the stainless steel was heated to 300 ^{0}C firstly and then conditioned to 6.4×10^{-3} C·mm^{-2}, the SEY reduced to 1.34 and 1.10, separately. XPS results demonstrated that the graphic layer could grow on the clean surface and reduced SEY to a lower value. The SEY of TiZrV coating was almost the average of the SEY of the individual metal.

References

[1] Zemek J, Jiricek P. XPS and He II photoelectron yield study of the activation process in Ti–Zr NEG films. Vacuum 2003;71:329-33.

[2] Li C-C, Huang J-L, Lin R-J, Lii D-F. Preparation and characterization of non-evaporable porous Ti–Zr–V getter films. Surface and Coatings Technology 2006;201:3977-81.

[3] Henrist B, Hilleret N, Scheuerlein C, Taborelli M. The secondary electron yield of TiZr and TiZrV non-evaporable getter thin film coatings. Applied Surface Science 2001;172:95-102.

[4] Hilleret N, Scheuerlein C, Taborelli M. The secondary-electron yield of air-exposed metal surfaces. Applied Physics A 2003;76:1085-91.

[5] Le Pimpec F, Kirby RE, King F, Pivi M. Properties of TiN and TiZrV thin film as a remedy against electron cloud. Nuclear Instruments and Methods in Physics Research Section A: Accelerators, Spectrometers, Detectors and Associated Equipment 2005;551:187-99.

[6] Biesinger MC, Payne BP, Grosvenor AP, Lau LWM, Gerson AR, Smart RSC. Resolving surface chemical states in XPS analysis of first row transition metals, oxides and hydroxides: Cr, Mn, Fe, Co and Ni. Applied Surface Science 2011;257:2717-30.

[7] Cimino R, ., Commisso M, ., Grosso DR, Demma T, ., Baglin V, ., Flammini R, ., et al. Nature of the decrease of the secondary-electron yield by electron bombardment and its energy dependence. Physical Review Letters 2012;56:112-8.

[8] Ma Q, Rosenberg R A. Surface study of niobium samples used in superconducting rf cavity production, Particle Accelerator Conference, 2001. Pac 2001. Proceedings of the. IEEE, 2001:1050-1052 vol.2.

[9] Lozano MP, Fraxedas J. XPS analysis of the activation process in non-evaporable getter thin films. Surface and Interface Analysis 2000;30:623-7.

[10] Zameroski ND, Kumar P, Watts C, Svimonishvili T, Gilmore M, Schamiloglu E, et al. Secondary electron yield measurements from materials with application to collectors of high-power microwave devices. IEEE Transactions on Plasma Science 2006;34:642-51.

[11] Halbritter J. ON CHANGES OF SECONDARY EMISSION BY RESONANT TUNNELING VIA ADSORBATES. Le Journal De Physique Colloques 1984;45:C2-315-C2-7.

[12] Kirby RE, King FK. Secondary electron emission yields from PEP-II accelerator materials ☆. Nuclear Instruments & Methods in Physics Research 2001;469:1-12.

Chapter 6. SEY mitigation by laser treatment

In this chapter, the SEY of metal surfaces modified by a nanosecond pulsed laser irradiation will be reported. This laser treatment leads to the formation of highly organised surface microstructures. Laser irradiation can transform highly reflective metals to black or dark coloured metal [1]. An example of blackening by laser treatment is shown in **Figure 6-1** demonstrating two copper samples (a) untreated and (b) laser treated [2].

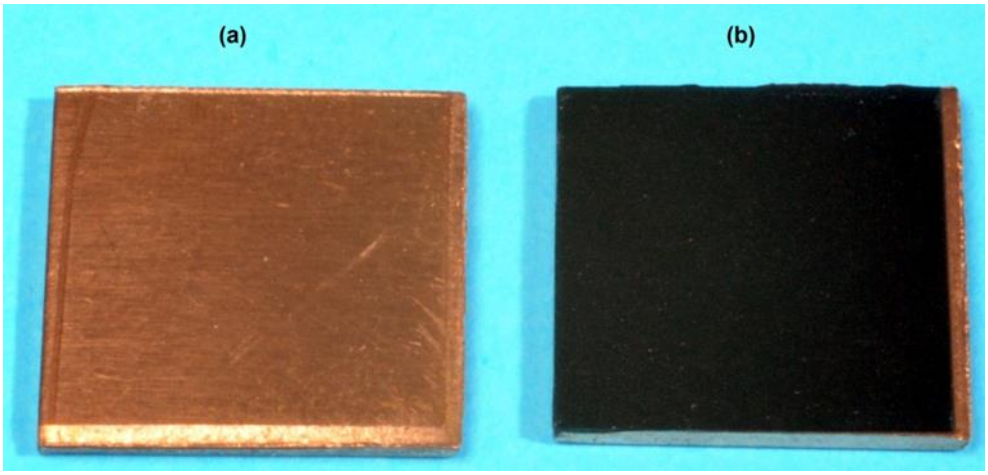

Figure 6-1 . **Copper samples: (a) untreated and (b) laser treated.**

This broadband absorption of electromagnetic radiation is typically around 85-95%, which is ranging from ultraviolet to infrared. This is widely ascribed to the formation and combined actions of surface nano- and micro-structures produced by laser processing of metals. The blackening process was carried out on the surfaces of copper (Cu), aluminum (Al) and 316L stainless steel (SS) plates with a purity of 99.999% and 1 mm thickness. This surface treatment without introducing new material only modifies the microstructure of the surface. Therefore, it is expected that the impact on the wake impedance and wake fields should be less than any other E- cloud mitigation techniques, which is also one of the significant worries in the E-cloud mitigation techniques. Furthermore, it is easy to apply this technique to existing vacuum surfaces with minimum disturbance to the in-situ beam line. This laser blackening treatment changes only the topography, so the materials remain the same. The

blackening process is carried out in an inert gas or air environment at atmospheric pressure, so the actual cost of the mitigation is low in comparison to other techniques such as PVD coating described in Chapter 5, mechanical grooves, electrodes, solenoid fields, etc. The laser treated surface is highly reproducible and provides a very stable surface chemistry. Also the surface is robust and immune to any surface delamination.

Due to the advantages of this new technology, the aim of this chapter is to study the SEYs of different nanosecond pulsed laser treated surfaces on the Cu, Al alloys, 316L stainless steel (SS) as a function of thermal treatment and electron beam bombardment with XPS analysis of the surface chemical composition.

6.1 The influence of electron conditioning to blackened samples

As is well-known, in particle accelerators, the SEY gradually decreases in time with machine operation due to the bombardment of the vacuum chamber walls by synchrotron radiation and multipacting electrons. This decrease, called " the conditioning effect," or "scrubbing", affects the surface chemistry by gradually growing a graphitic–like C-C carbon thin layer [3]. So in this section, the influence of electron conditioning with a flood electron gun at 500 eV energy will be studied on the surface of blackened Cu, SS and Al. The difference of SEY between blackened samples and normal samples will be compared. The changes of Cu surface compositions will be detected by XPS before and after laser surface treated and electron conditioning.

The electron conditioning leads to the reduction of SEY for all samples in the range of irradiated primary electron energy from 80 to 1000 eV, as seen from **Figure 6-2** to **Figure 6-4**. The untreated surfaces all exhibit the same overall SEY behavior *viz.* rising from values obtained with low primary electron energy to a maximum at a few hundred electron volts followed by a steady decline. All treated surfaces also demonstrate the same overall SEY behavior *viz* rising from values obtained with low primary electron energy but stabilization after 500 eV. After 500 eV, most electrons have been absorbed into the bulk instead of coming out from the surface. It also shows that the SEY reduction between the

as-received untreated and treated sample is more significant for low energy primary electrons**.** For example, the SEY of as-received Cu is 1.56, 1.90, 1.41 at 1000, 275 and 80 eV, respectively. The SEY of blackened Cu is 1.08, 1.02 and 0.63 at 1000, 275 and 80 eV, respectively, which means that each SEY reduces 30, 46 and 55% at the corresponding primary electron energy. It is clearly seen that the SEY reduction for laser treated surfaces at low electron energies is much more than that at high electron energies. The electron dose for normal Cu is higher than that for laser treated Cu. However, the SEY of normal Cu is much higher than that of laser treated Cu after electron conditioning. Electron conditioning could produce a graphitic-like carbon layer on the surface in order to reduce the SEY, which has been explain in chapter 6. In this case, the SEY of normal Cu should be higher than that of laser treated Cu due to longer conditioning. However, the SEY of normal Cu is still much higher than that of laser treated Cu. This also explains the importance of this special morphology to the effect of SEY.

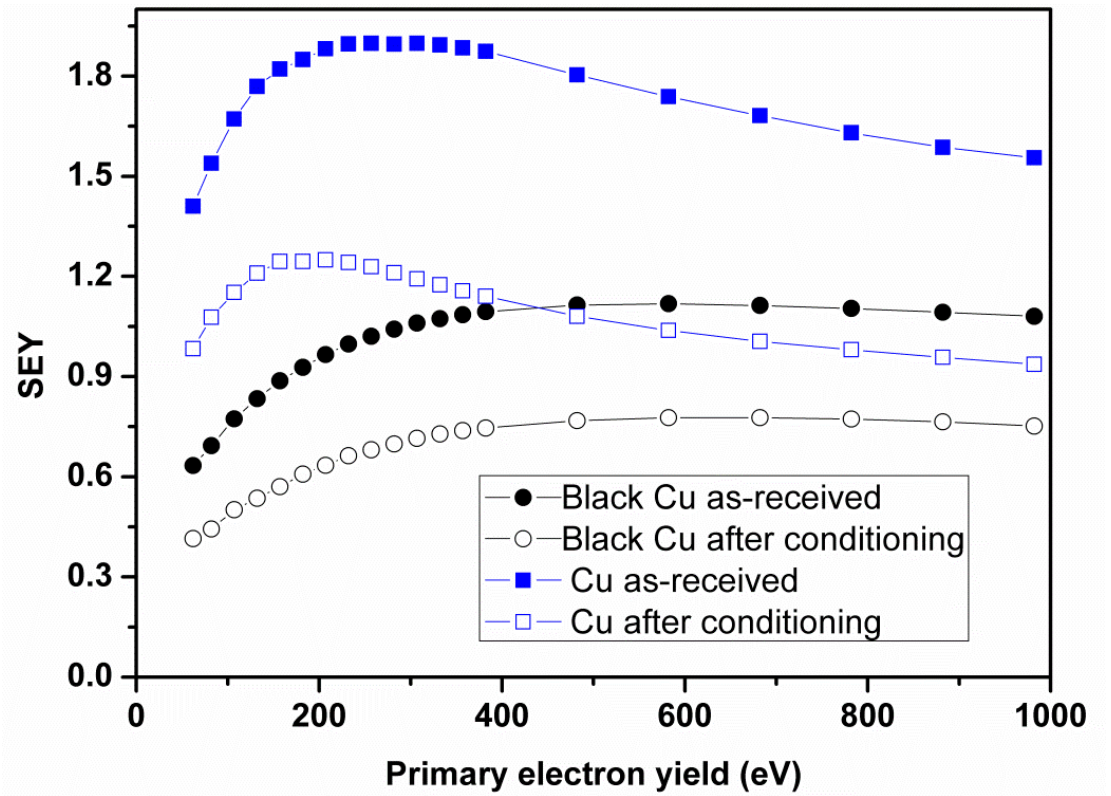

Figure 6-2 SEY for Cu as a function of primary electron energy: Cu for untreated surface, black Cu for laser treated surface, and conditioning for electron bombardment with a dose of 1.0×10^{-2} C·mm^{-2} for Cu and 3.5×10^{-3} C·mm^{-2} for black Cu.

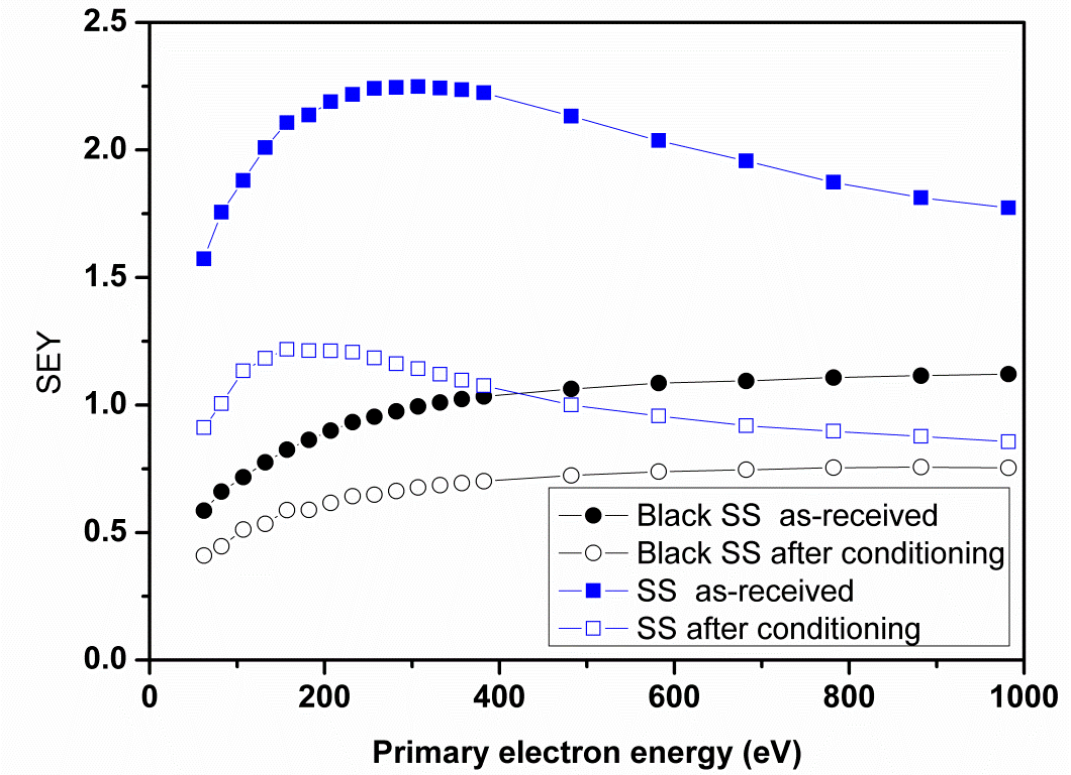

Figure 6-3 SEY for 316L stainless steel as a function of primary electron energy: SS—untreated surface, black SS—laser treated surface, and conditioning—electron bombardment with a dose of 1.7×10^{-2} C·mm^{-2}.

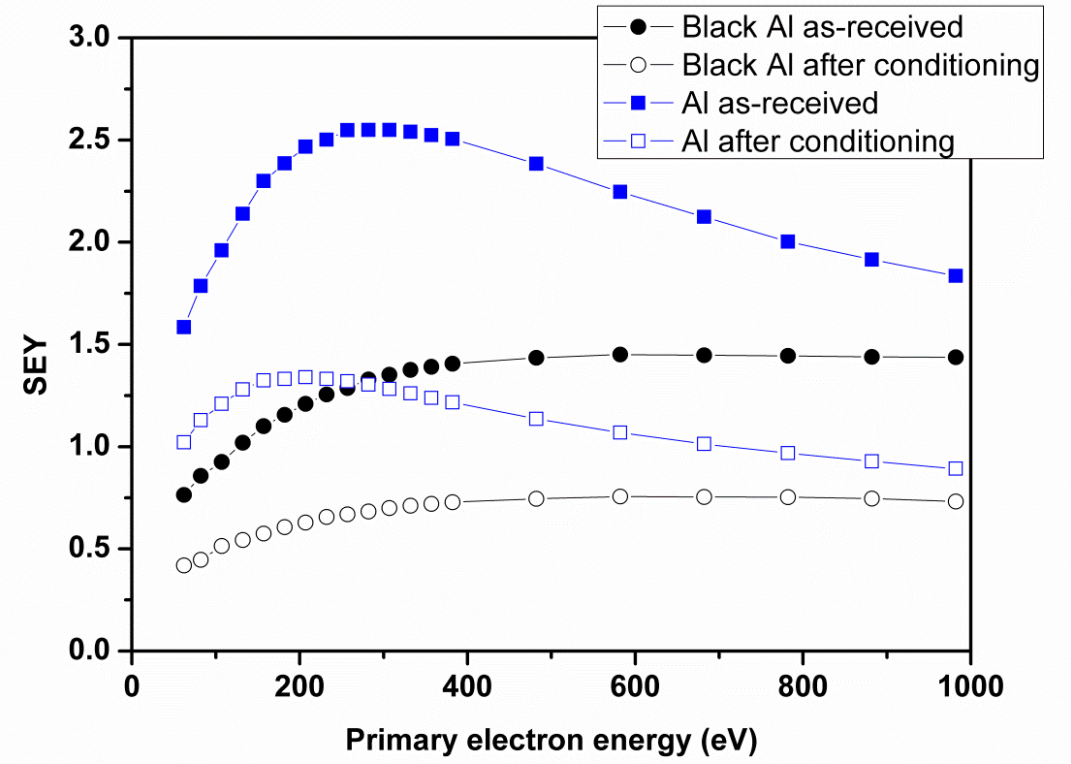

Figure 6-4 SEY for Al as a function of primary electron energy: Al—untreated surface, black Al—laser treated surface, and conditioning—electron bombardment with a dose of 1.5×10^{-2} C·mm^{-2} for Al and 2.0×10^{-2} C·mm^{-2} for black Al.

The dependence of δ_{max} as a function of electron dose for all samples is shown in **Figure 6-5**. All samples show the continuous reduction of SEY with electron dose. It is also obvious that δ_{max} of the as-received laser treated sample is almost a factor of 2 lower than the respective untreated sample. For example, for the laser-treated Cu plate, δ_{max} is 1.05 as compared with δ_{max}=1.85 for untreated sample.

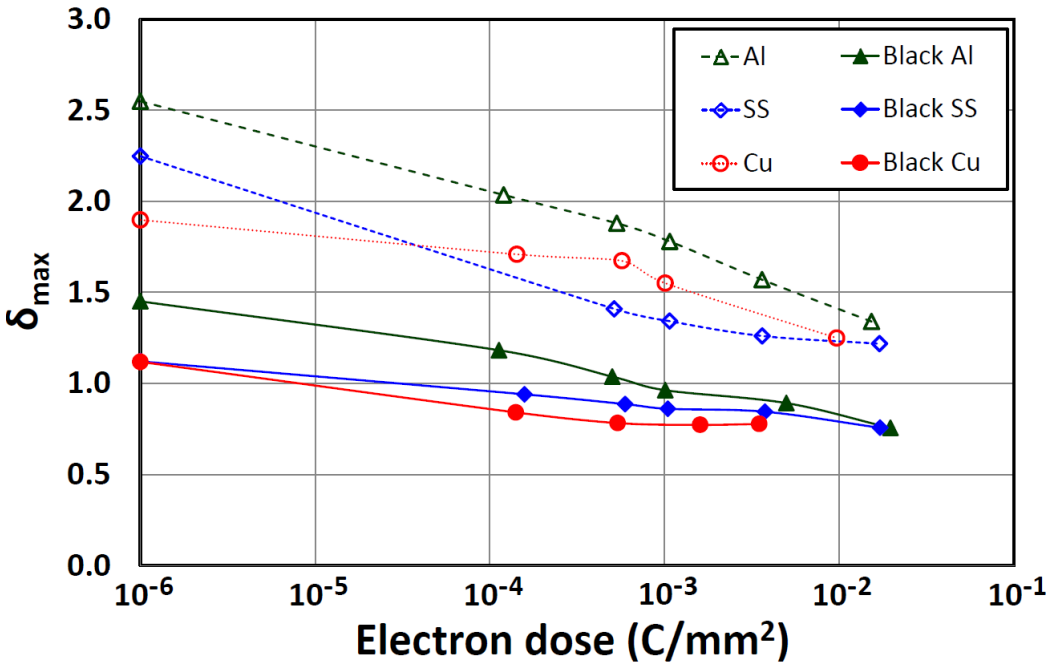

Figure 6-5 δ_{max} as a function of electron dose for Al (untreated surface, black), 306L stainless steel (untreated surface, black) and Cu samples (untreated surface, black).

The results of δ_{max} and E_{max} for all treated and untreated sample before and after electron bombardments are summarised in **Table 6-1.** For Cu plate, the δ_{max} at the primary electron energy E_{max}=600 eV decreases to 0.78 from 1.12 for the laser treated samples after an electron dose of 3.5×10^{-3} C·mm^{-2} as compared to δ_{max}=1.25 (with E_{max}=600 eV) for the untreated sample over the electron dose of 1.0×10^{-2} C mm^{-2}. Similar reduction for SS and Al samples are concluded in this table as well.

The surface changes of the normal Cu and black Cu have also been compared in the **Table 6-2**. It is clearly shown the differences of normal Cu and black Cu before and after electron conditioning by comparing the areas. It is also shown that the compositions of as-received black and normal Cu have the similar chemistry. The oxygen and carbon contaminations are on both laser treated

and normal surfaces. So the low value of δ_{max} for as-received laser sample is mainly due to the surface topography induced by the laser processing.

Table 6-1 The δmax of as-received and conditioned samples

Sample	Initial		After conditioning to Qmax		
	δmax	Emax (eV)	δmax (Qmax)	Emax (eV)	Qmax (C·mm-2)
Black Cu	1.12	600	0.78	600	3.5×10-3
Black SS	1.12	900	0.76	900	1.7×10-2
Black Al	1.45	900	0.76	600	2.0×10-2
Cu	1.90	300	1.25	200	1.0×10-2
SS	2.25	300	1.22	200	1.7×10-2
Al	2.55	300	1.34	200	1.5×10-2

Table 6-2 XPS results of surface composition of (a) as-received and (b) electron beam conditioned Cu samples.

Sample	Condition	Cu2p 933 eV	Cu2p 943 eV	C 285 eV	C 288 eV	O1s 531 eV
		Peak area (a.u.) at bunding evergy				
Cu	(a)	7309	1535	9243	2332	9969
	(b)	19896	0	10037	953	4369
Black Cu	(a)	5968	1903	1919	476	2746
	(b)	12191	0	2359	286	1202
	Peak area ratios (b)/(a)					
Cu		2.72	0	1.09	0.41	0.44
Black Cu		2.04	0	1.23	0.60	0.44

The reduction of SEY as a function of electron dose has been studied and reported by many authors [4-6]. This decrease of this conditioning effect changes the surface chemistry by gradually building a thin layer of graphitic-like C-C carbon [4]. An example of an XPS measurement as-received black Cu is displayed in **Figure 6-6** to show the surface changes by the electron bombardment. Full spectrum reveals not only the Cu spectral features but also the presence of C and O at around 285 and 531 eV, respectively, due to surface contaminants after the prolonged stay in air. The details of the Cu2p and C1s core level spectra are shown in **Figure 6-6.** The Cu2p3/2 peak in the Cu2p spectrum exhibits the metallic and suboxide Cu_2O component at the BE of 932.3 eV, a shoulder at 934.4 eV and a satellite structure at BE ~10 eV higher due to the stoichiometric CuO oxide phase [7]. The C1s spectrum exhibits that

a main structure peak is at the BE of 284.6 eV and a weaker peak located around 288.1 eV. The main structure peak can be ascribed to the presence of C-C and C=O bonds.

After electron irradiation up to a total dose of 3.5×10^{-3} C·mm^{-2}, the XPS spectra of black copper measured is also displayed in **Figure 6-6**. It shows that the intensity of Cu and C peaks increase and the O peak decreases, which means that the reduction of CuO and carbon accumulation. The Cu2p spectrum illustrates that the metallic component at BE of 932.3 eV has gained intensity and is more narrow compared with the as-received surface and the satellite at around BE of 934 eV is reduced. These chemical modifications may depend on the dissociation of Cu –O, C-H and C-O bonds and desorption of O_2 and H_2O under the action of the impinging electrons [6]. The loss of O molecules reduces the oxidation state in the contaminated surface and results in a SEY decrease [6]. In the C spectrum, the C=O peak has been decreased and the intensity of C-C increases dramatically at 284.2 eV. The growth of a carbon layer originates from the dissociation of residual gas molecules existing in the ultrahigh vacuum and the release gases from the hot electron beam filament, typically CO and CO_2. They absorb on the sample surface and are dissociated by the imping electrons. Then the O atoms desorb as O_2 and the C atoms bind to each other to form the graphitic-like organized network [5, 6].

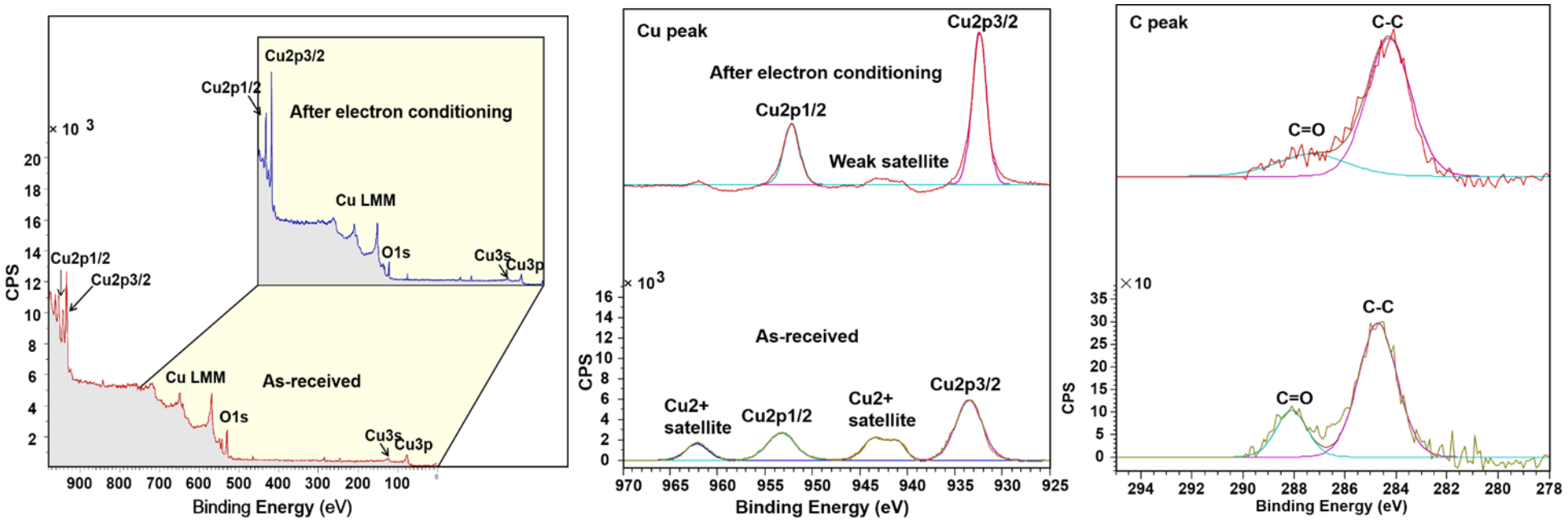

Figure 6-6 Full XPS spectra for treated Cu and its Cu and C peaks before and after 3.5×10^{-3} Cmm^{-2} electron bombardment.

6.2 Laser treated Cu with different hatch distances, pulse lengths and atmospheres

In the first section, the SEY of laser treated surfaces have been first introduced and studied as a function of electron doses. Then in this section, the laser treated Cu will be studied in detail by changing hatch distance, pulse length, atmosphere and beam directions. Three different types of structures will also be introduced. The laser treated parameters for these three types have been introduced in Section 3-1. The surfaces of Cu are modified by a 25 nanosecond pulsed laser, leading to the formation of highly organised surface microstructures. The SEM pictures for these three type of structures are shown from **Figure 6-7** to **Figure 6-9.** The structures of the same type in air or Ar are similar, so the SEM images for different types in air are shown below as examples. **Figure 6-7** shows type I structures in air with different hatch distances. **Figure 6-7(1)** describe that the type I in air with 50 μm hatch distance has a closed square pyramid shaped structure. When the hatch distances get larger, a hollow starts to form the open square based top pyramid (volcano throat like), which can be seen in **Figure 6-7 (2)-(3). Figure 6-8** shows that type II with 50 μm hatch distance in air has a groove structure. **Figure 6-9** shows that the type III with 50 μm hatch distance in air is covered with nano-spherical coral structures on the top of the closed pyramid. The groove depth for type III is about 80 μm. Then in this section, the SEYs of all three type of laser treated Cu are compared as a function of thermal treatment with XPS analysis.

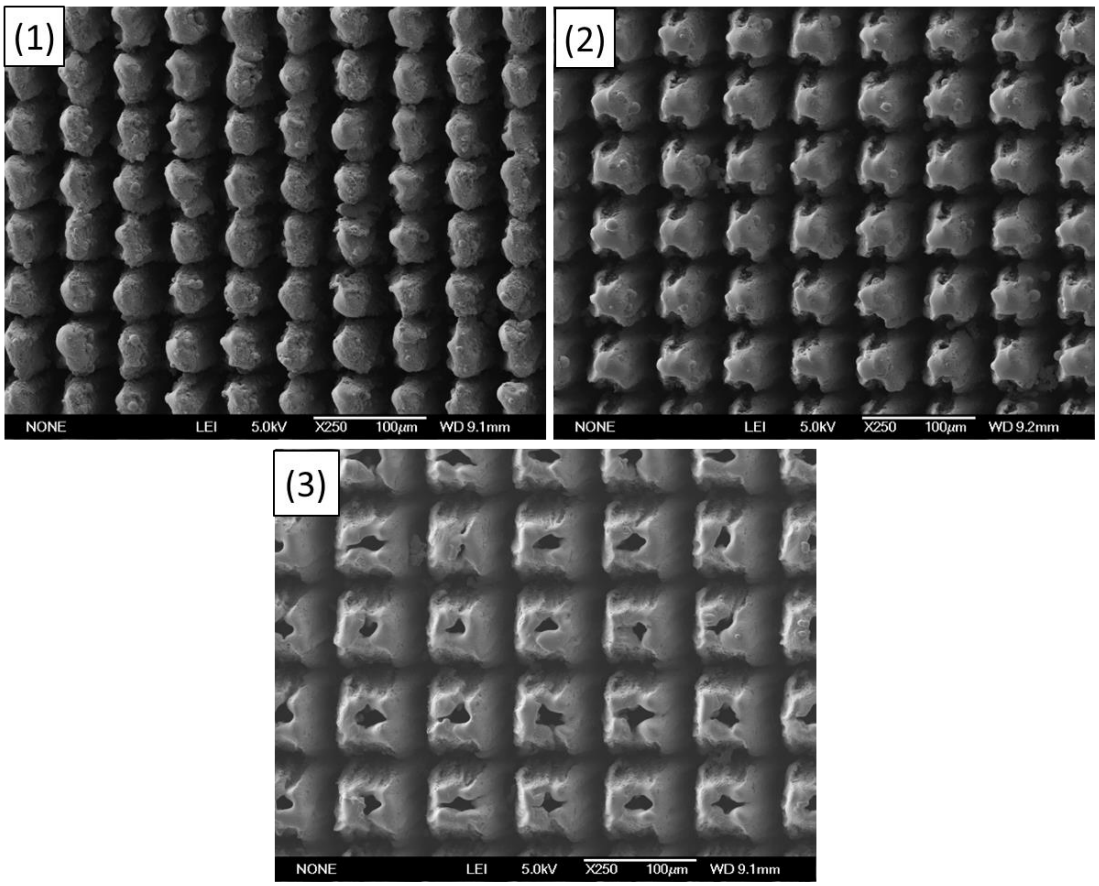

Figure 6-7 Type I structures in Air with different hatch distances (1) 50 μm, (2) 60 μm, (3) 80 μm

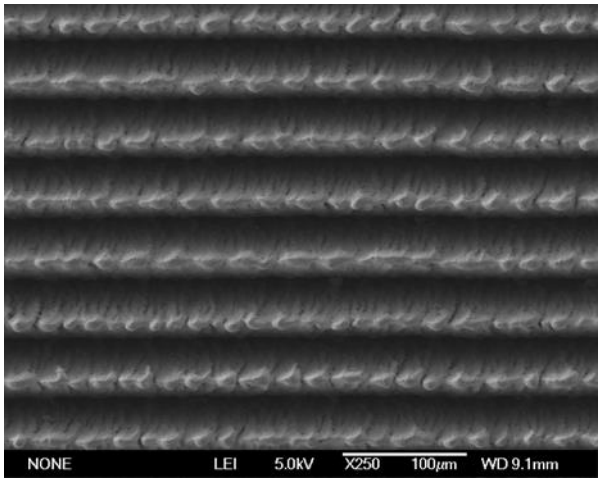

Figure 6-8 Type II structures in Air with 50 μm hatch distances

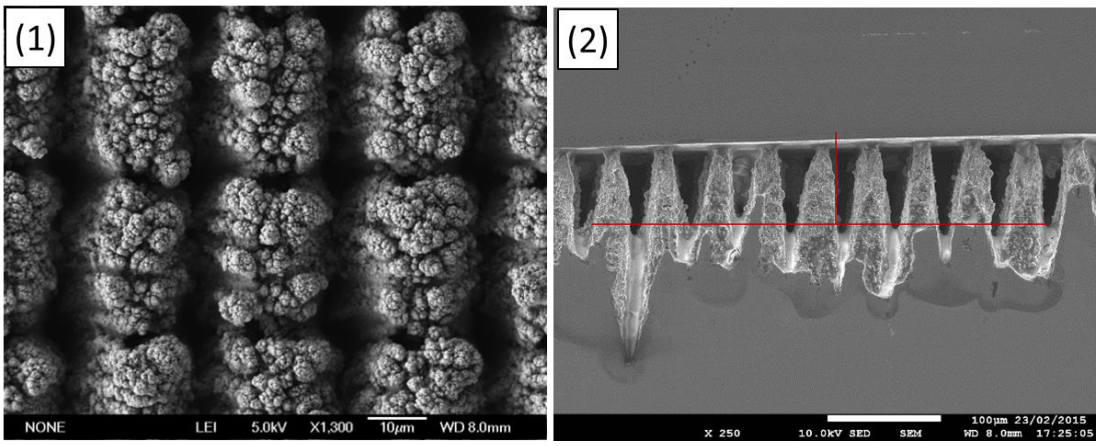

Figure 6-9 Type III surface structures and cross-section in Air with 50 μm hatch distances

6.2.1 Type I laser engineered Cu in Air with different hatch distances

The Type I structure in Air has been described in this section. The surfaces of Cu were laser treated in an air atmosphere at room temperature with different hatch distance, 50, 60 and 80 μm. The SEY of laser treated blackened Cu in Air have been investigated before and after heating to 250 ^{0}C for 2 hours.

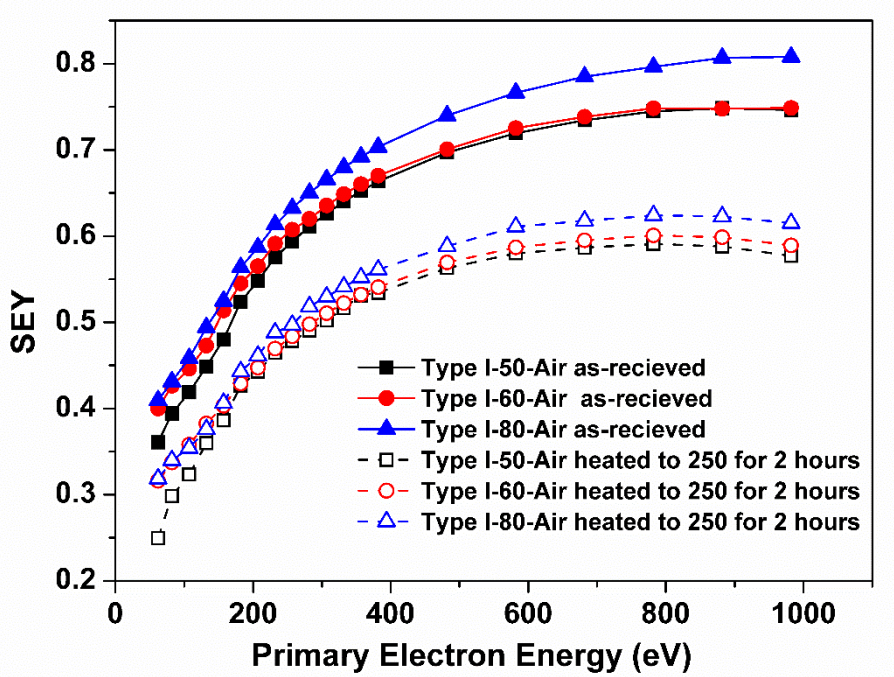

Figure 6-10 SEY of treated Cu in Air with varying microstructure distance as a function of primary electron energy before and after thermal treatment.

The SEY was measured as a function of energy of the primary electrons are shown in **Figure 6-10** for treated Cu in air with 50, 60 and 80 μm microstructure distance, respectively, before and after heating to 250 ^{0}C for 2 hours, for type I

structures. The maximum value of SEY, δ_{max} = max($\delta(E)$), measured at corresponding primary electron enery E_{max} can easily describe the differences of these samples. The δ_{max} of 50, 60 and 80 μm blackened Cu are 0.75, 0.75 and 0.80, respectively, all of which are lower than 1. These as-received SEYs of the blackened Cu are much lower than that of bulk Cu, which is about 2.02, as shown in **Figure 6-11**. The blackened Cu and bulk Cu have the same cleaning procedure before the SEY measurements. However, the special surface topographies of laser treated blackened coppers reduce the secondary electron yield from 2.0 to lower than 1.

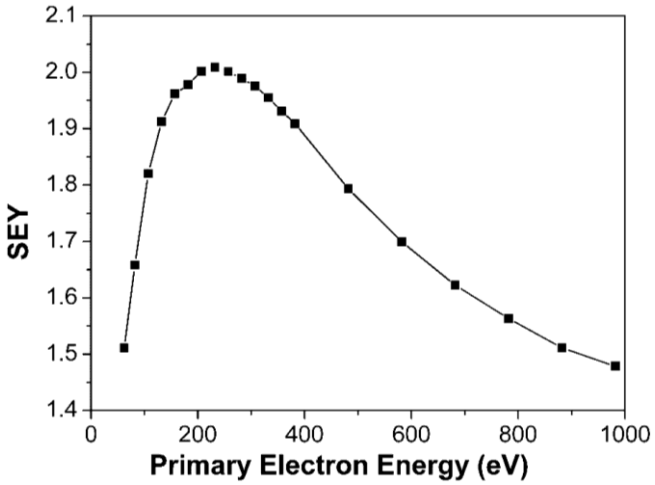

Figure 6-11 SEY of as-received bulk Cu

After heating to 250 ºC for 2 hours, in all cases the δ_{max} drops to 0.59, 0.60, 0.62, separately. The reduction of SEYs by thermal treatments is due to changing the surface composition of these blackened samples. The surface analysis of laser treated samples before and after heating will explain the effects of thermal treatment to SEY, which will be shown in **Figure 6-12** and **Table 6-3**, respectively.

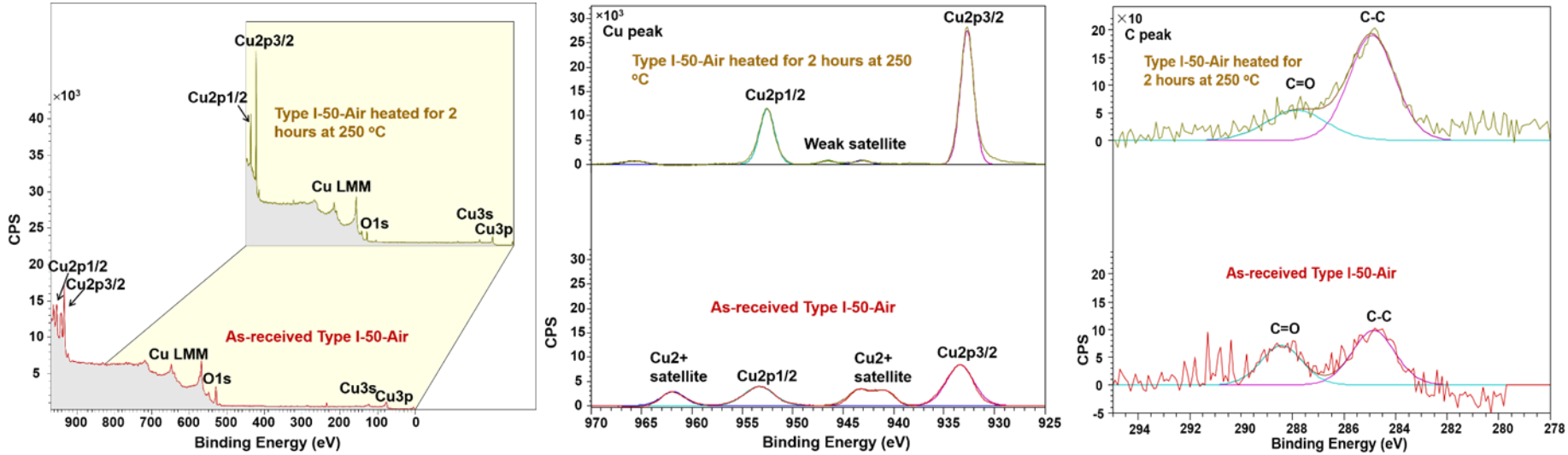

Figure 6-12 Full spectrum XPS for treated Cu and its Cu peak, and C peak in air before and after thermal treatment

The XPS surface characterisation studies were carried out on the laser treated 50 µm blackened Cu in air shown in **Figure 6-12**. Considering the survey spectrum of the as-received treated 50 µm Cu sample in air there is, as expected, a strong O peak. The Cu2p has four characteristic peaks, which indicate the presence of CuO. The CuO is characterized by high intensity shake-up satellites at ~9 eV higher binding energy than the main 2p3/2 and 2p1/2 peaks, which are broader than that of bulk CuO and Cu metal. However, after thermal annealing to 250 ^{0}C for 2 hours, O peaks reduce and a Cu 2p XPS spectrum generally associated with a Cu_2O surface with weak satellite structure to the main peaks was observed (Figure 6-12). Cu3p, Cu3s and Auger peaks become obvious in the spectrum. The as-received C1s peaks are at binding energy of 288.3 and 284.5 eV, which may be attributed to C=O and C=C, respectively. After thermal treatment for 2 hours at 250 ºC, the graphitic carbon peak at 284.5 is still on the surface and the intensity has increased. Compared with C=C, the density of C=O has been reduced. Overall, these observations were attributed to oxygen diffusing into the metal surface and CuO transforms to sub-stoichiometric oxide. The surface compositions of all these black sample before and after thermal treatments are shown in **Table 6-3**. The density of O has been reduced to half for all three samples after thermal treatment.

In a conclusion, after thermal treatments, oxygen reduced on the top of laser treated surfaces and at the same time, CuO transformed to sub-stoichmetric oxide. Compared to the as-received sample, the surface morphology stayed the same, however, the surface compositions were changed. So the reduction of SEYs for these blackened samples by thermal treatments is due to changing the surface composition.

Table 6-3 XPS results of surface composition of (a) as-received and (b) heated black Cu samples in air

Sample	Condition	Cu2p 933 eV	Cu2p 943V	C 285V	C 288 eV	O1s 531 eV
		Peak area (a.u.) at bunding evergy				
50 μm Black Cu	(a)	28493	16362	209	145	6537
	(b)	45709	2903	434	141	3579
60 μm Black Cu	(a)	28488	23482	141	150	6028
	(b)	35997	2731	341	103	3028
80 μm Black Cu	(a)	25367	12659	131	129	5449
	(b)	41147	4043	204	0	2691
		Peak area ratios (b)/(a)				
50 μm Black Cu		*1.60*	*0.18*	*2.08*	*0.97*	*0.55*
60 μm Black Cu		*1.26*	*0.12*	*2.42*	*0.69*	*0.50*
80 μm Black Cu		*1.62*	*0.32*	*1.56*	*0*	*0.49*

6.2.2 Type I laser engineered Cu in Ar with different hatch distances

The surfaces of Cu were laser produced in an argon atmosphere at room temperature with different hatch distance, 50, 60 and 80 μm. The SEYs of laser treated blackened Cu in Ar have been investigated by heating to 250 ^{0}C for 2 hours. The SEY was measured as a function of energy of the primary electrons and is shown in **Figure 6-13** for these three treated blackened Cu in Ar. The δ_{max} of 50, 60 and 80 μm blackened Cu in Ar are 0.79, 0.84 and 0.94, respectively. The surfaces of blackened Cu in Ar and air have the same special morphology, which is the reason for lower the SEY of the as-received surface. After heated to 250 ^{0}C for 2 hours, in all case the δ_{max} drop to 0.68, 0.72, 0.77, respectively. XPS in **Figure 6-14** shows the surface changes of the 50 μm blackened Cu in Ar before and after thermal treatments to 250 ^{0}C for 2 hours.

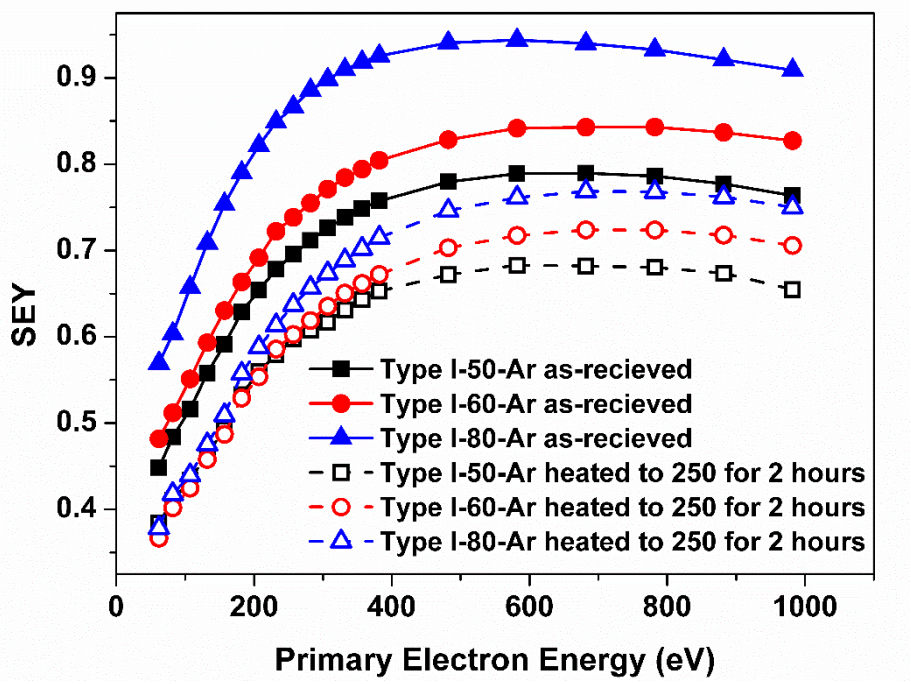

Figure 6-13 SEY of treated Cu in Ar with varying microstructure distance as a function of primary electron energy before and after thermal treatment.

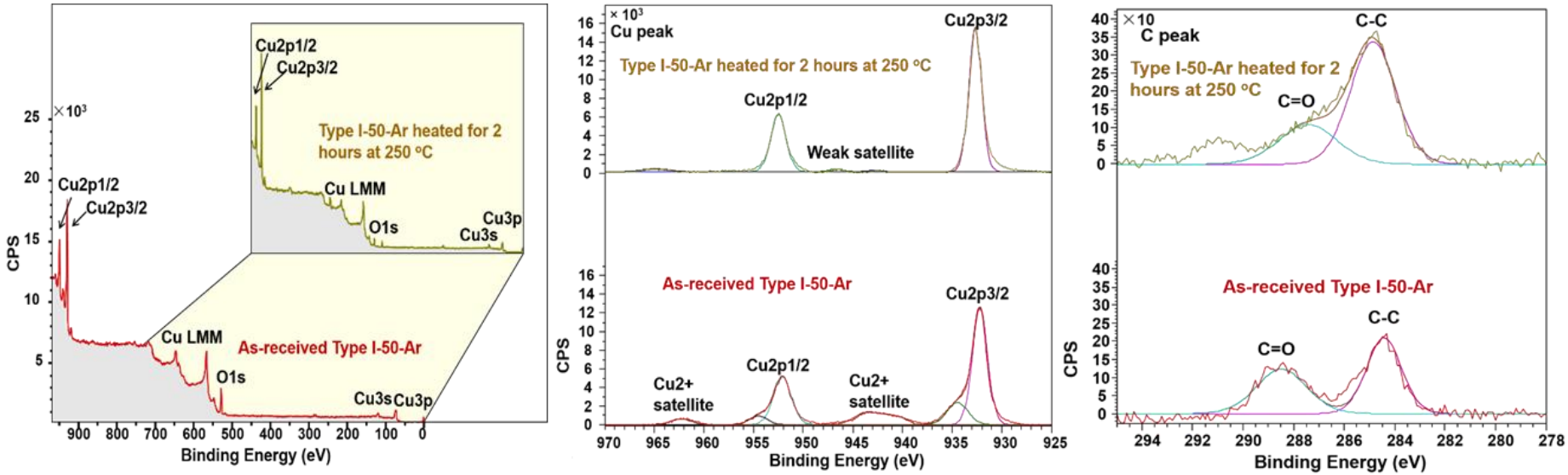

Figure 6-14 Full spectrum XPS for treated Cu and its Cu and C peaks in Ar before and after thermal treatment

The full spectrum of the as-received treated 50 µm blackened Cu samples in Ar shows the presence of CuO on the surface. However, after heating to 250 ^{0}C for 2 hours, O peaks reduce and CuO disappeared. Cu3p, Cu3s and Auger peaks exist in the spectrum. Cu2p3/2 and Cu2p1/2 peaks also have moved to the lower binding energies of 932.6 and 952.5 eV, which are associated with Cu_2O. The as-received C1s peaks are at the binding energy of 288.6 and 284.5 eV, which are attributed to C=O and C=C, respectively. After thermal treatment for 2 hours at 250 ºC, the graphitic carbon peak at the binding energy of 284.8 eV increases on the surface. C1s peak at the binding energy of 288.0 still exists but reduces. Overall, similar to blackening Cu in Air, these observations were attributed to oxygen diffusing into the metal and CuO transforms to sub-stoichiometric oxide. However, the oxygen content on the surface of blackening Cu in Ar is much lower than that on the surface of blackening Cu in Air. The surface compositions of all these black samples before and after thermal treatments are shown in **Table 6-4**.

Comparison of **Table 6-3** and **Table 6-4,** the surface of Type I in air has more O than that in Ar. But the SEY of as-received Type I in air is much lower than that of in Ar. For example, the SEY of as-received Type I with 80 µm hatch distance in air is 0.80, however, the SEY of as-received Type I with 80 µm hatch distance in Ar is 0.94. The surface morphology of Type I in air and Ar is also similar. However, the reduction may be due to differences in the depth of grooves between the two conditions. In the case of laser treatment in air, the surface oxidises from the onset of the first laser pulse which may absorb more in the following received pulses and hence produce deeper structures. So the SEM of a cross-section needs to be done for the future work.

Table 6-4 XPS results of surface composition of (a) as-received and (b) heated black Cu samples in Ar

Sample	Condition	Cu2p 933 eV	Cu2p 943V	C 285V	C 288 eV	O1s
		Peak area (a.u.) at bunding evergy				
50 μm Black Cu	(a)	23969	7204	368.0	312	5301
	(b)	25021	852	773.0	302	2072
60 μm Black Cu	(a)	10938	1642	213	136	2719
	(b)	17120	0	165	69	1534
80 μm Black Cu	(a)	23331	2540	560	346	5202
	(b)	38477	0	383	144	539
		Peak area ratios (b)/(a)				
50 μm Black Cu		*1.04*	*0.12*	*2.10*	*0.97*	*0.39*
60 μm Black Cu		*1.57*	*0*	*0.77*	*0.51*	*0.56*
80 μm Black Cu		*1.65*	*0*	*0.68*	*0.42*	*0.10*

6.2.3 Type II laser engineered Cu in Air and Ar

The results in last section have shown that the structure of 50 μm hatch distance has the lowest SEY. In this section, laser treated grooved Cu with 50 μm hatch distance in Air or Ar are studied. The grooved laser treated Cu in Air or Ar is formed by raster-scanning over the target surface in only one direction. Grooved laser treated Cu samples in Air and Ar are investigated with respect to heating to 250 ^{0}C for 2 hours. These series blackening copper is defined to Type II.

The variation of the SEYs for grooved laser treated Cu samples in Air in **Figure 6-15** and in Ar in **Figure 6-16** are plotted as a function of primary electron energy from 80 eV to 1000 eV. The δ_{max} of the as-received grooved Cu in Air is 0.76 and 0.57 after heating duration for 2 hours at 250 ^{0}C. The δ_{max} of the grooved Cu in Ar is 0.89 for as-received sample and 0.77 for heating at 250 ^{0}C for 2 hours. The SEY of both samples has shown a significant decrease after thermal treatments. However, no visible change in E_{max} (800 eV) is observed before and after the heating.

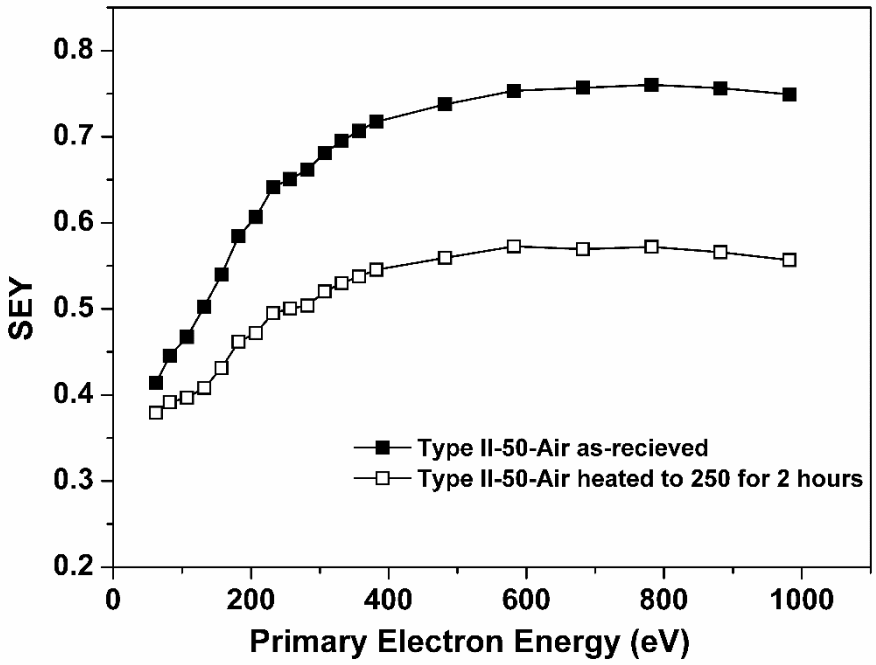

Figure 6-15 SEY of grooved Cu in Air with 50 μm microstructure distance as a function of primary electron energy before and after thermal treatment.

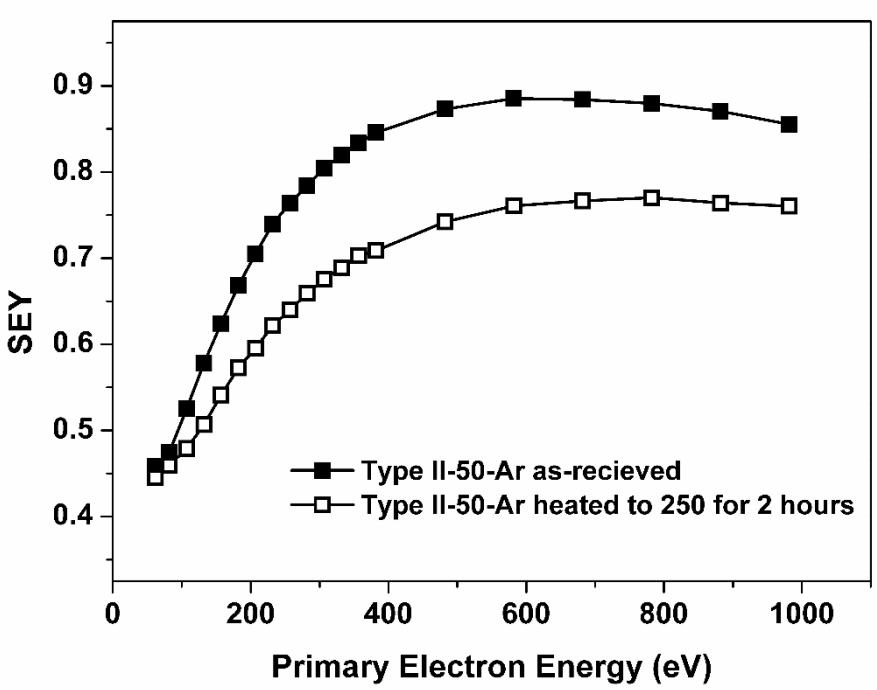

Figure 6-16 SEY of grooved Cu in Ar with 50 μm microstructure distance as a function of primary electron energy before and after thermal treatment.

The surface chemical composition on grooved laser treated Cu samples in Air in the as-received state and after the thermal treatment is presented in **Figure 6-17**. The CuO is characterized by high intensity shake-up satellite structures at 943 eV. The thermal treatment results in a decrease of the oxygen concentration on the surface, which lead to increase of metal copper concentration. Cu2p3/2 and Cu2p1/2 peaks have moved to the binding energies of 932.7 and 952.7 eV, which associated with Cu_2O after thermal treatment. But it is hard to see the carbon peaks on the surfaces of the grooved laser treated Cu samples.

Comparison of **Figure 6-17 (2) and Figure 6-18(2)**, Type II in Air has a much stronger Cu^{2+} satellite peak, which means that laser irradiation in air induces a stoichiometric oxide as compared to the one laser irradiated in Ar. It is well known that the SEY of an oxide surface has a higher value of SEY as compared with the less oxide surface. However, in the case of two surfaces, the SEY of laser irradiated in Ar produced a higher SEY value which is opposite of expected result. The reduction of of SEY for the higher oxide surface could be due to the deeper grooves created during laser irradiation because the surface became oxides at the onset of the first laser pulse which decreased the surface

reflectivity. This means that a higher portion of the laser beam absorbed by the surface and hence leading to deeper grooves.

Figure 6-18 summarizes XPS of grooved laser treated Cu samples in Ar in the as-received state and after the thermal treatment. The big difference of grooved laser treated Cu samples in Ar and Air is that grooved laser treated Cu samples in Ar has low oxygen concentration on the surface. The effect of the thermal treatment also decreases the oxygen concentration on the surface. Cu2p3/2 and Cu2p1/2 peaks have moved to the Cu_2O binding energies of 932.7 and 952.6 eV after thermal treatment. Carbon concentration is also very little on the surface on the as-received and heated surfaces. This can be due to burning the carbon at the surface in the presence of oxygen in the atmosphere during laser treatment.

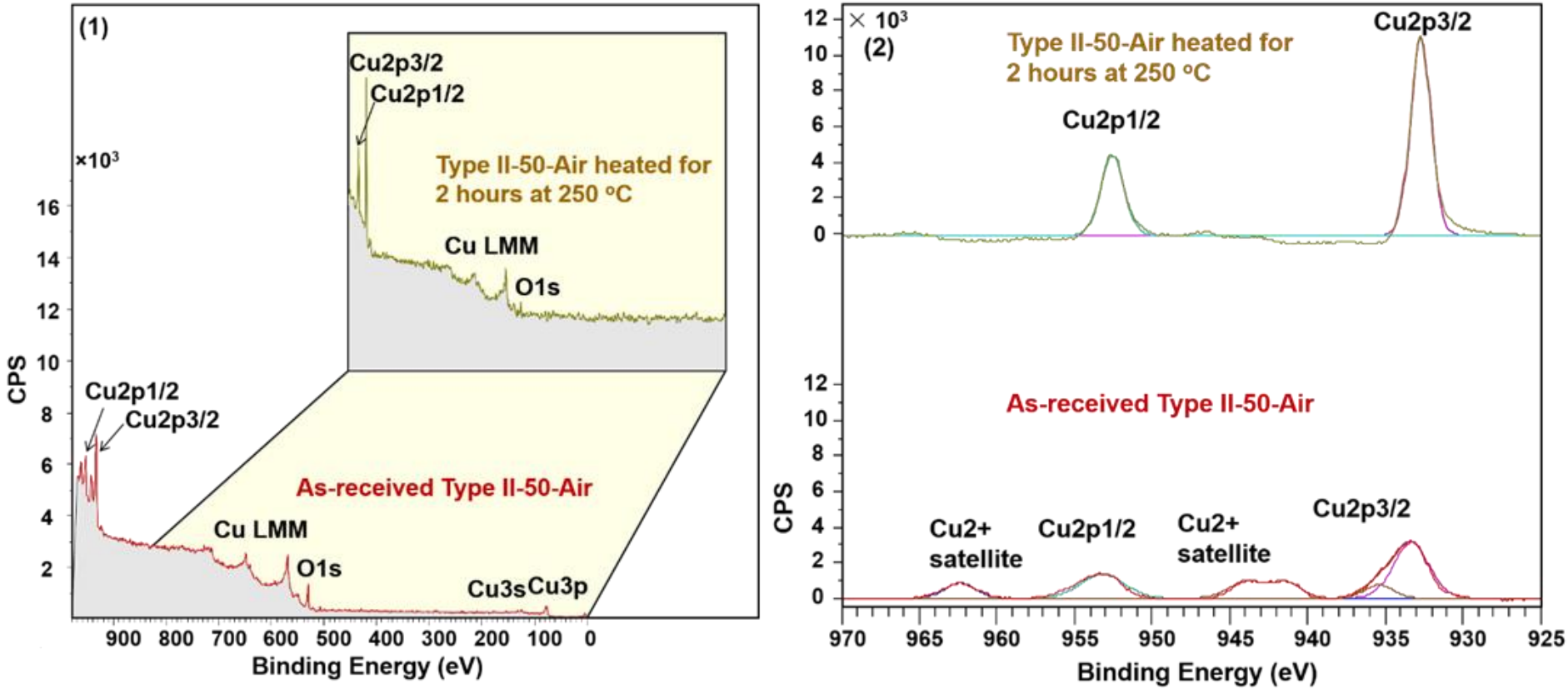

Figure 6-17 XPS for 50 μm grooved Cu in Air before and after thermal treatment (1) Full spectrum (2) Region spectrum of Cu peak

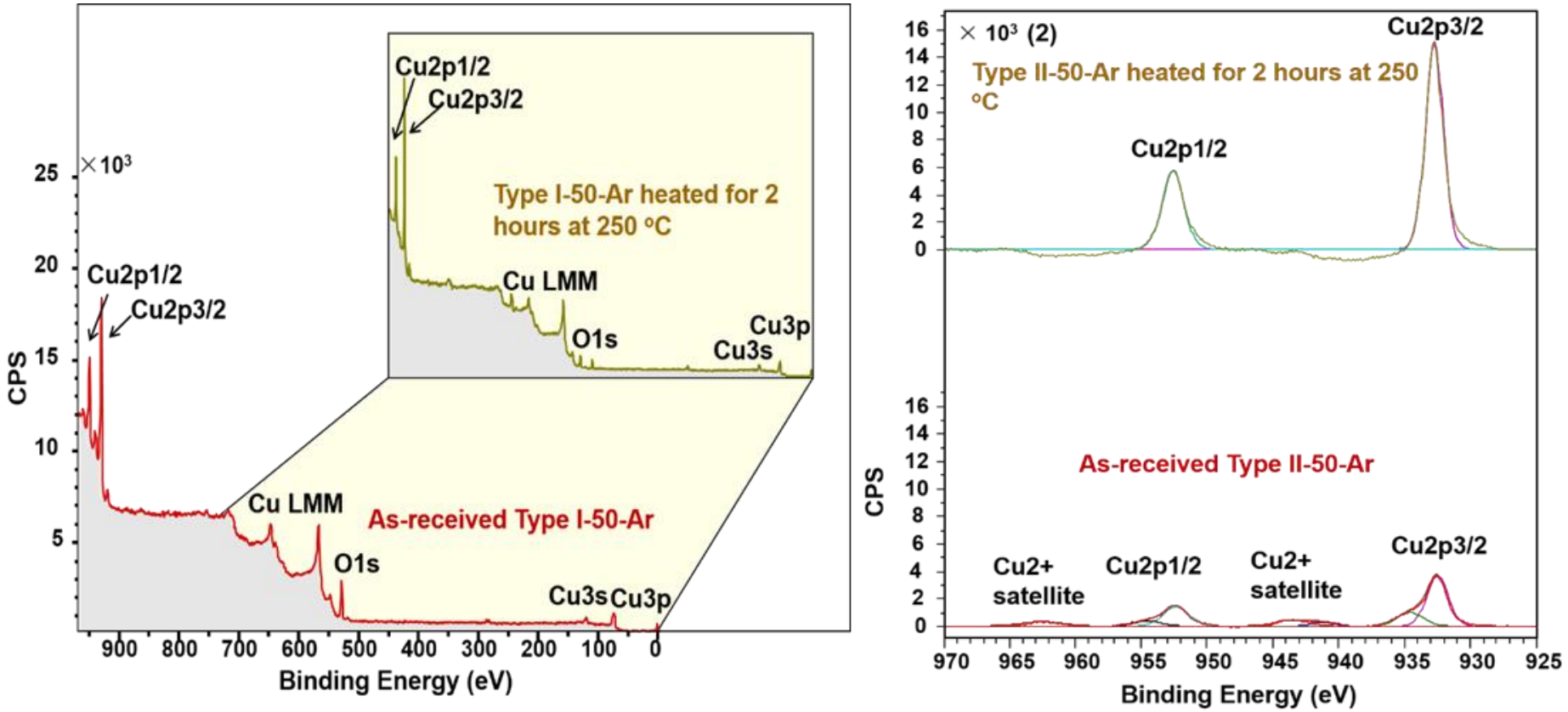

Figure 6-18 XPS for 50 μm grooved Cu in Ar before and after thermal treatment (1) Full spectrum (2) Region spectrum of Cu peak

6.2.4 Type III laser engineered Cu in Air

Thermal treatment is one of the recovery methods to reduce the SEY. In this section, Type III laser treated Cu in Air is investigated for thermal treatment testing at 250 ^{0}C for 2 hours.

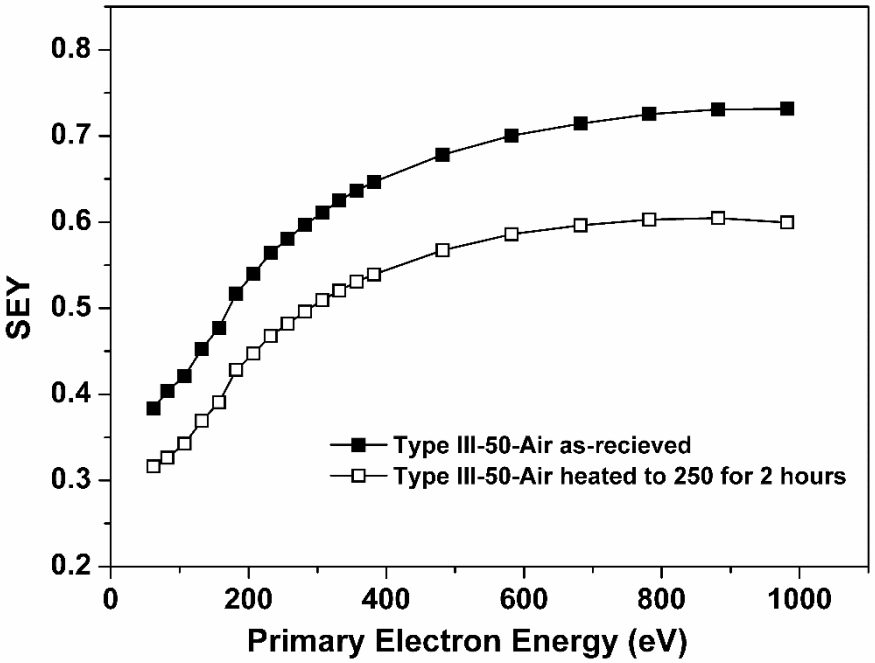

Figure 6-19 SEY of Type III Cu in Air with 50 μm hatch distance as a function of primary electron energy before and after thermal treatment.

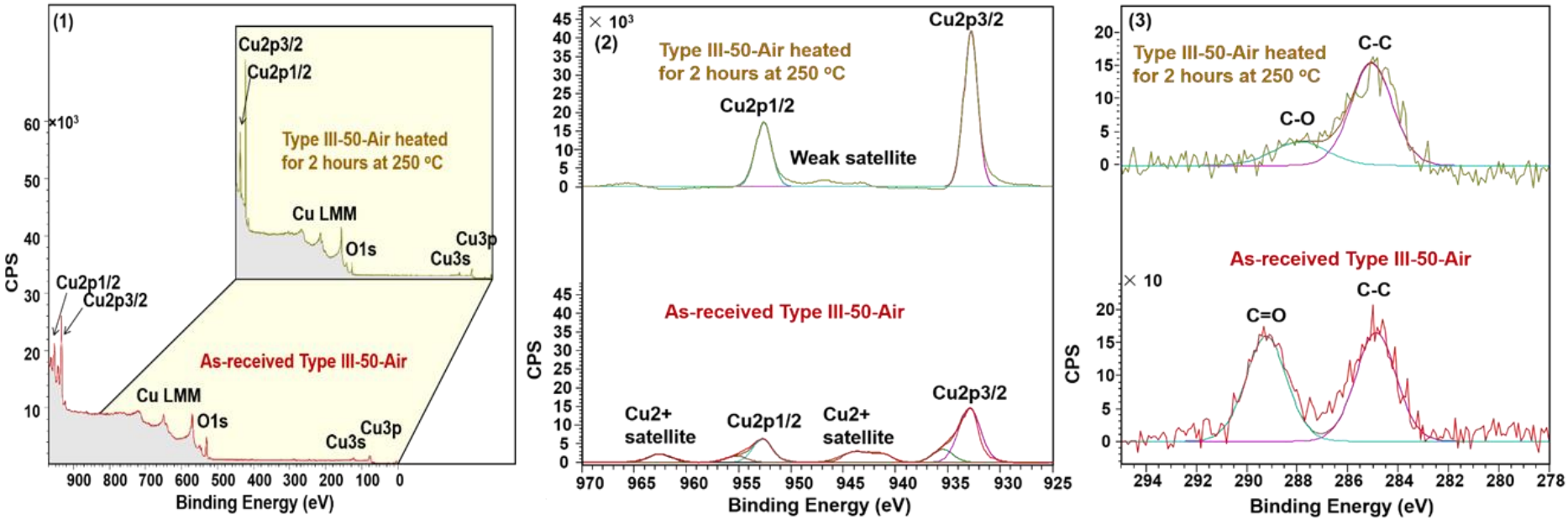

Figure 6-20 XPS for Type III Cu in Air with 50 μm hatch distance before and after thermal treatment (1) Full spectrum (2) Region spectrum of Cu peak (3) Region spectrum of C peak

In **Figure 6-19**, the variation of the SEYs for Type III laser treated Cu in Air is shown. The δ_{max} is 0.73 before the thermal treatment. However, after 2 h heating, the SEY has a significant decrease to 0.60. No visible change in E_{max} (1000 eV) is observed before and after the heating.

Figure 6-20 illustrates the surface changes of Type III laser treated Cu before and after the thermal treatment. In **Figure 6-20** (1), the oxygen concentration has been decreased by the effect of the heating. In **Figure 6-20**(2), it is clearly shows that the Cu(II) shake-up disappeared and CuO has been transformed to Cu_2O. Cu2p3/2 and Cu2p1/2 peaks have moved to the binding energy of 932.8 eV and 952.7 eV, respectively. In **Figure 6-20** (3), the C1s line for as-received sample displays two clear peaks at about 285.1 eV and 289.3 eV, binding energies related to C-C and C=O, respectively. After heating, the peak associated to C-C bond grows. But binding energy of the other C1s peak is shift to 287.5 eV and the intensity reduced dramatically.

6.3 Ti-Zr-V on the Laser Treated Copper

As the Ti-Zr-V has the good vacuum properties and black copper has really low SEY, the Ti-Zr-V on the black copper will be studied in this section. **Figure 6-21** shows the SEYs of the Ti-Zr-V on the Type I Cu with 60 μm hatch distance in air and Type III Cu before and after thermal activation. The δ_{max} of as-received Type I Cu with 60 μm hatch distance in air are 0.75. However, the δ_{max} of as-received Ti-Zr-V on the Type I Cu with 60 μm hatch distance in air is 0.91, which is higher than blackened Cu itself. Then after heating to 200 ºC for 2.5 hours, it is reduced to 0.62. The δ_{max} of the Type III Cu in Air is 0.73. Similarly, the δ_{max} of as-received Ti-Zr-V on the Type III Cu in Air is 0.99, which is still higher than that of Type III Cu in Air. After heating to 300 ^{0}C, it dropped to 0.75. However, it is still higher than that of as-received Type III Cu in Air.

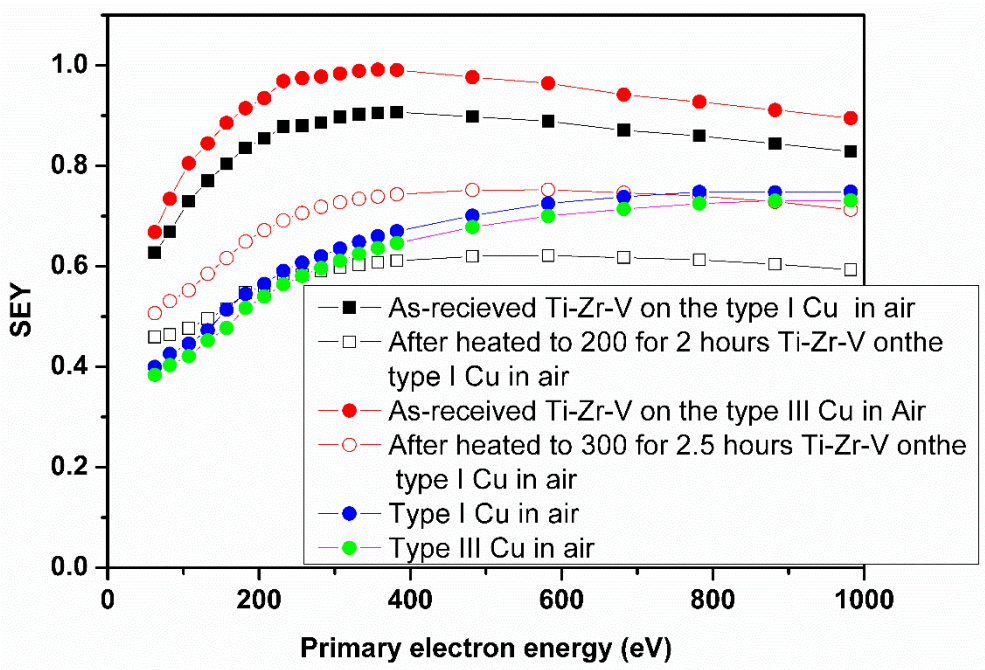

Figure 6-21 SEY reduction of Ti-Zr-V on the black copper as a function of primary electron energy showing variation with annealing treatments.

The XPS of Ti-Zr-V on the Type I Cu with 60 μm hatch distance in air and the Type III Cu in Air are plotted in **Figure 6-22** and **6-23**, respectively. From both as-received XPS spectra, they reveal that the surface, as expected, has obvious strong C1s and O1s peaks. Not only Ti2p, Zr3d and V 2p but also Cu2p exists on the surface, which illustrate the Ti-Zr-V coatings did not cover all the surface on both samples. All metal peaks are in the oxide state, for example, in the **Figure 6-22 (1)**, the $Ti2p_{3/2}$ and $Ti2p_{1/2}$ peaks are shifted to 458.7 and 464.4 eV, respectively, indicating the presence of TiO_2. The $Zr3d_{5/2}$ and $Zr3d_{3/2}$ peaks are shifted to 182.2 and 184.6 eV, respectively, indicating the presence of ZrO_2. The $V2p_{3/2}$ and $V2p_{1/2}$ peaks are shifted to 516.4 and 522.4 eV, respectively, indicating the presence of VO_2. The $Cu2p_{3/2}$ exhibits the component at the BE of 932.7 eV, a shoulder at 934.8 eV and a satellite structure at BE ~10 eV higher due to the CuO oxide phase.

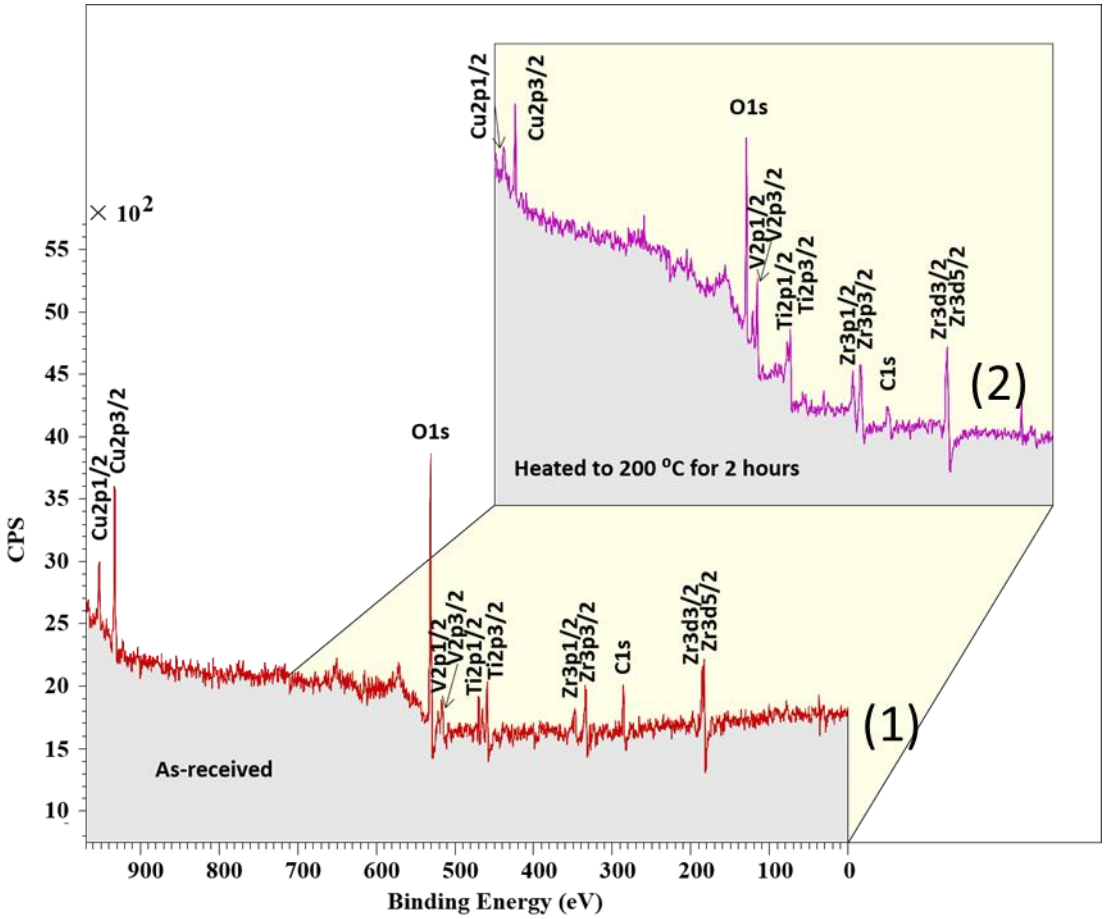

Figure 6-22 The XPS spectra of Ti-Zr-V on the Type I Cu with 60 μm hatch distance in air (1) as-received, (2) after thermal treatment to 200 ºC for 2 hours

After annealing, the oxide layer of both two samples have been removed. The oxygen peaks on both samples decrease dramatically, seen in **Figure 6-22(2)** and **Figure 6-23(2)**. All Ti2p, V 2p and Cu2p metal peaks have shifted towards metal state, for example, in the **Figure 6-22** (2), the $Ti2p_{3/2}$ and $Ti2p_{1/2}$ peaks are shifted to 455.1 and 461.1 eV, respectively. The $V2p_{3/2}$ and $V2p_{1/2}$ peaks are shifted to 513.3 and 520.8 eV, respectively. The $Cu2p_{3/2}$ spectrum illustrates that the Cu(II) has disappeared and the peak at BE of 932.3 eV has higher intensity and more narrow compared with the as-received surface. However, The $Zr3d_{5/2}$ and $Zr3d_{3/2}$ peaks are not shifting, which keep at the binding energy of 182.2 and 184.6 eV, respectively, indicating that ZrO_2 still appear on the surface. This means that Zr element has not started activating at 200 °C and it needs much higher annealing temperature compared with other elements.

XPS of Ti-Zr-V on the Type III Cu in Air shows almost the same change before and after thermal treatment as that of Ti-Zr-V on the Type I Cu in air. Apart from

Zr element, after annealing at 300 °C for 2.5 hours, the $Zr3d_{5/2}$ and $Zr3d_{3/2}$ peaks are shifted to 179.9 and 182.4 eV, respectively, indicating the Zr has been started activating.

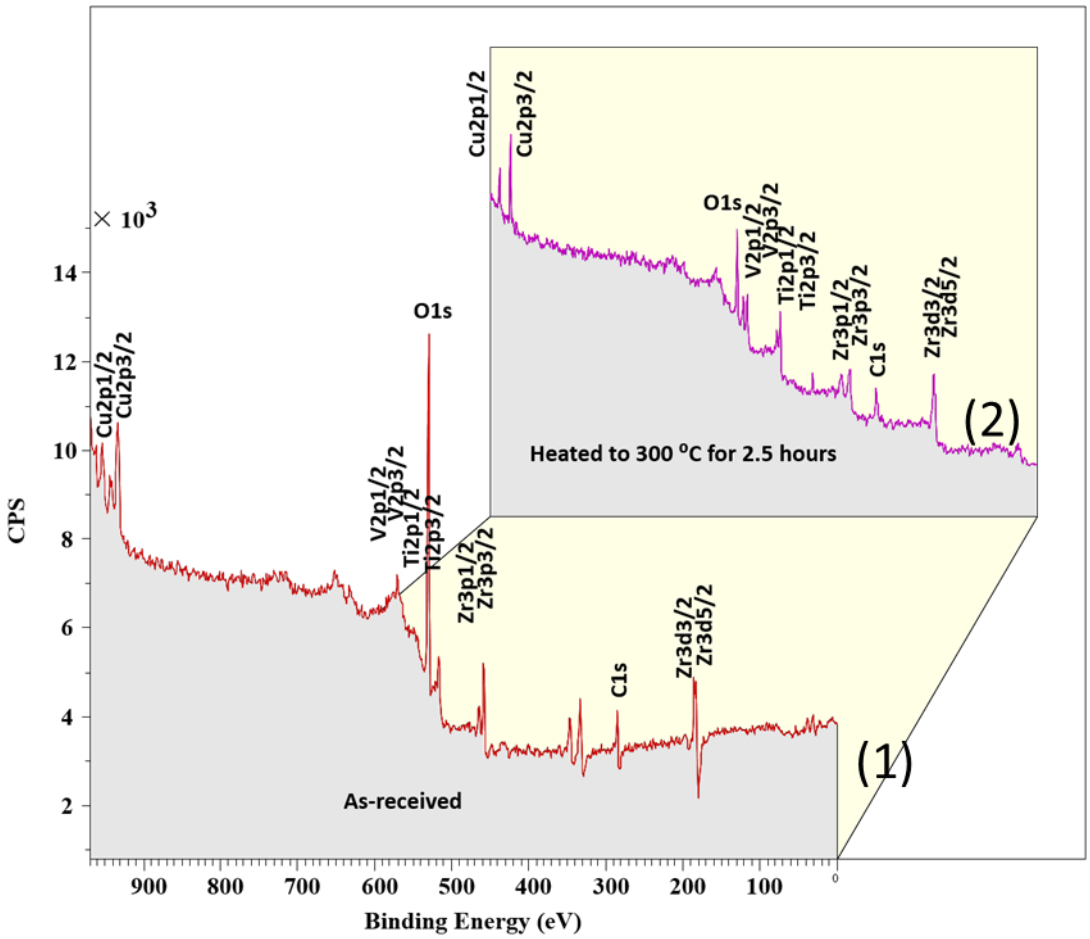

Figure 6-23 The XPS spectra of Ti-Zr-V on the Type III Cu in Air (1) As-received, (2) after thermal treatment to 300 ºC for 2.5 hours

In **Table 6-5,** it shows that the chemistry comparison between Ti-Zr-V on the two Types of treated Cu. It clearly shows that deposition of Ti-Zr-V produced a large amount of oxygen and some carbon on the surfaces. The oxygen on the Type III Cu in Air is even more than that of Type I with 60 μm hatch distance in Air. So this may be the reason for that the SEY increases after depositing the Ti-Zr-V on the two Types of laser treated copper. The SEY of Ti-Zr-V on the Type III Cu in Air is even higher than that of Type I with 60 μm hatch distance in Air.

Table 6-5 XPS chemistry comparison between Ti-Zr-V on the Type I with 60 μm hatch distance and Type III Cu in Air

Sample	Cu2p3/2 933 eV	C1s 285 eV	O1s 531 eV	Ti2p3/2 458 eV	Zr3d5/2 182 eV	V2p3/2 516eV
	Peak area (a.u.) at binding evergy					
Ti-Zr-V on the Type I Cu	1267	652	2647	856	846	839
Ti-Zr-V on the Type III Cu	9650	2461	15082	3272	3205	3239

6.4 SEY of laser treated stainless steel

Nanosecond pulsed laser treated stainless steel, similar with laser treated Cu, also form a laser organised surface microstructures. The surface structures will be shown by SEM.The δ_{max} of as-received stainless steel is about 2.0 in the literature [8]. In this section, the SEY of treated SS in Air and Ar with varying microstructure distances will be described before and after heating. Then the surface changes of blackening stainless steel will be demonstrated by XPS as a function of thermal treatments.

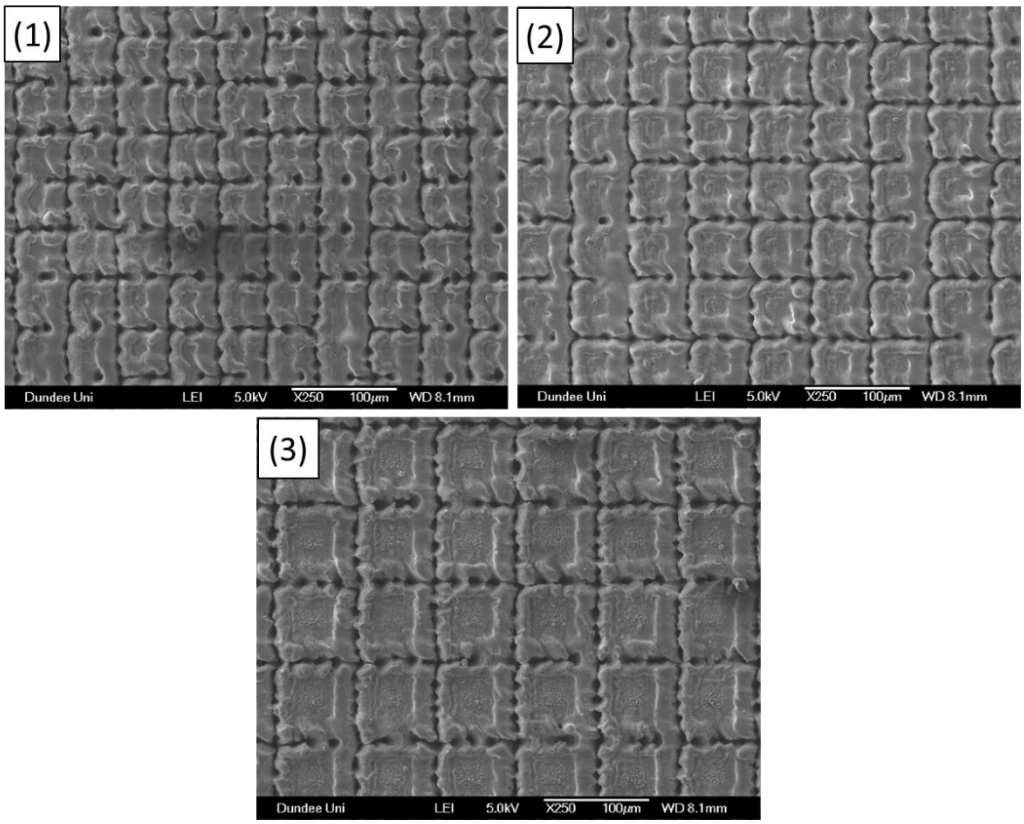

Figure 6-24 Stainless steel structure in Air with different hatch distances (1) 50 µm, (2) 60 µm, (3) 80 µm

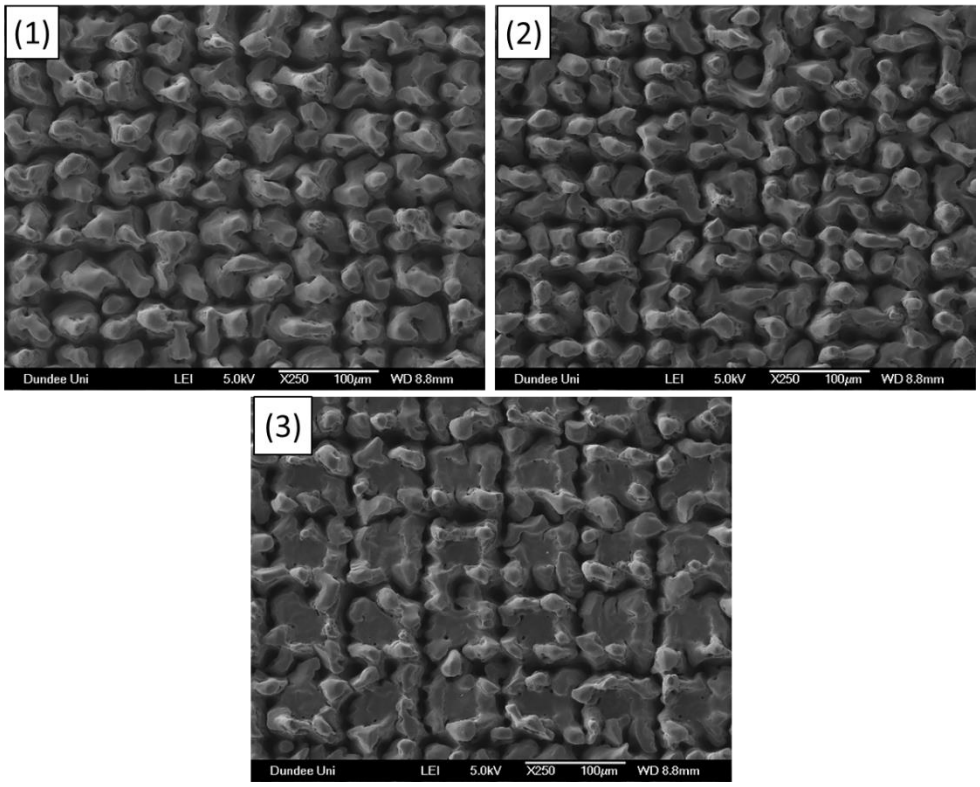

Figure 6-25 Stainless steel in Ar with different hatch distances (1) 50 µm, (2) 60 µm, (3) 80 µm

Figure 6-24 and **Figure 6-25** shows the SEM graphs of stainless steel structures in Air and Ar with different hatch distances. It describes that the stainless steel structures in Air with 50, 60, 80 µm hatch distance have the same closed square pyramid shaped structure. But the size of square pyramid increases with the increase of hatch distance. However, the structures of stainless steel in Ar are different with that in Air. The square pyramid has been formed gradually with increasing the hatch distances.

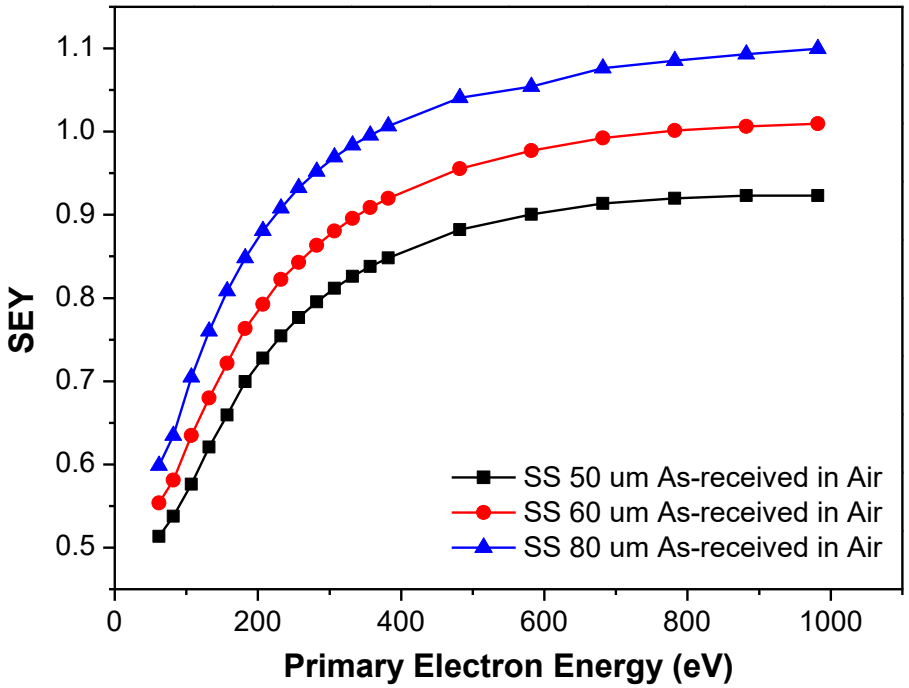

Figure 6-26 SEY of as-received treated SS in Air with varying microstructure distance as a function of primary electron energy

Figure 6-26 and **Figure 6-27** show the SEY curves measured on the as-received blackened stainless steels in Air and Ar, respectively. The SEY curves of as-received 50 µm, 60 µm and 80 µm stainless steel in Air have the similar trend. The SEY increases with increasing the primary electron energy and reaches the maximum point at 1000 eV, which is 0.92, 1.0 and 1.1 for 50, 60 and 80 µm, respectively. The SEY curve for as-received stainless steel in Ar is different. The δ(Ep) of stainless steel in Ar increases with gradually reducing gradient at low primary electron energies and reaches the highest point around 400 eV. The δ(Ep) of stainless steel in Air increases with primary electron energy but increases slowly after 400 eV. δ_{max} of as-received stainless steel in Ar are 0.98, 1.18, 1.40 for 50, 60 and 80 µm, respectively.

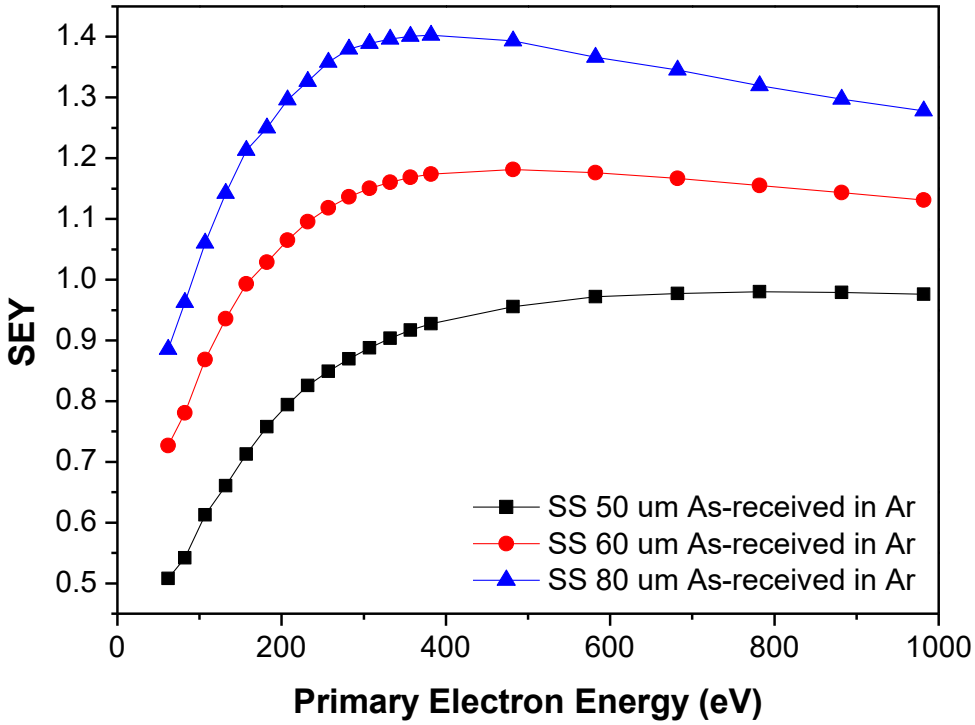

Figure 6-27 SEY of as-received treated SS in Ar with varying microstructure distance as a function of primary electron energy

Figure 6-28 describes the thermal effect to the SEY on the 60 µm stainless steel in Air and Ar as an example. After heating to 300 ^{0}C for 2.5 hours, δ_{max} decreased to 0.73 and 0.88 for the 60 µm stainless steel in Air and Ar, respectively. However, after heating, the shape of SEY has been changed. The SEY increases with increasing the primary electron energy and reaches the maximum point at 1000 eV.

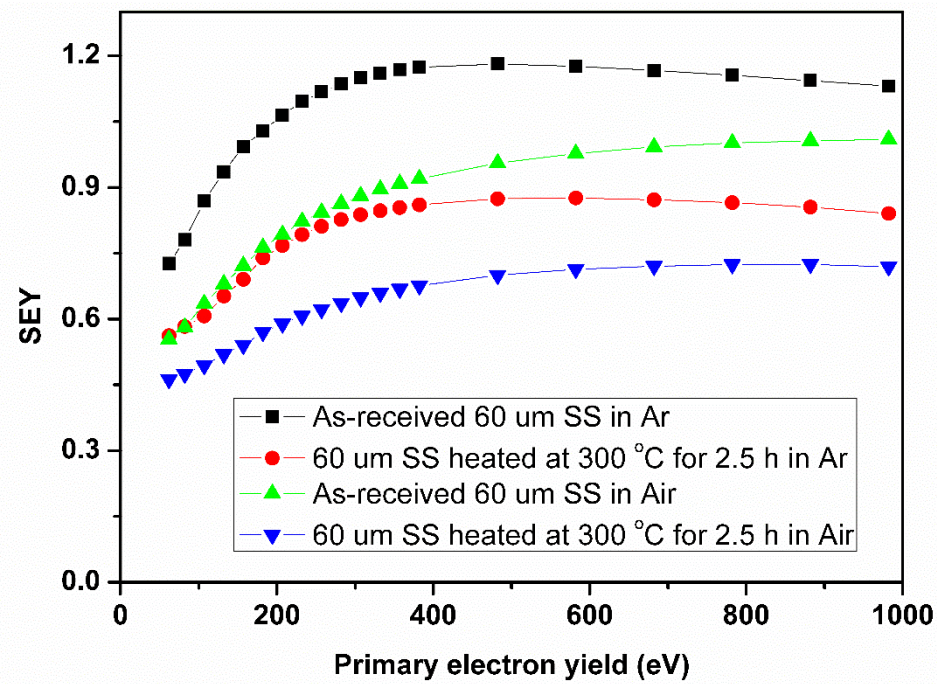

Figure 6-28 SEY of 60 µm SS in Ar and Air as a function of primary electron energy before and after thermal treatment

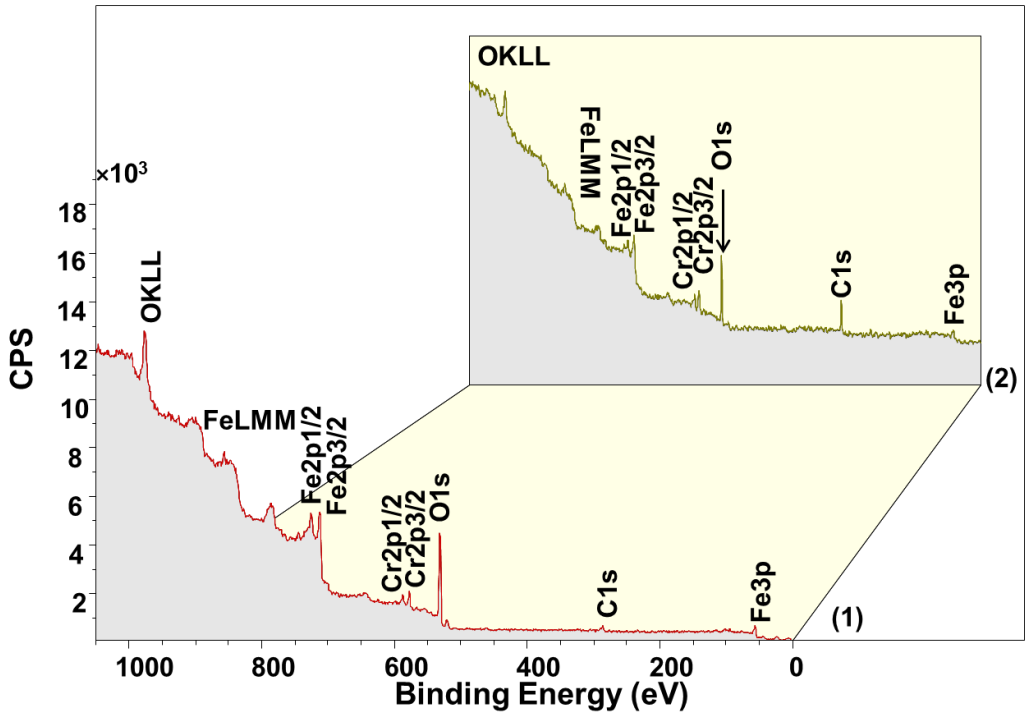

Figure 6-29 Full spectrum XPS for treated 60 µm SS in Air before and after thermal treatment (1) as-received, (2) heated to 300 ^{0}C for 2.5 hours

The XPS spectrum taken on the as-received 60 µm stainless steel surface (seen **Figure 6-29**) shows the Fe and Cr spectral features but also reveals the presence of C and O indicated by the C1s and O1s peaks at around 285 and

531 eV, respectively, due to surface contamination after the prolonged exposure to in air. The details of the Fe2p, Cr2p, O1s and C1s core level spectra for as-received 60 µm stainless steel are shown from **Figure 6-30** to **Figure 6-32**. The Fe2p spectrum exhibits that the Fe2p3/2 peak is at binding energy (BE) of 711.2 eV and a satellite structure is at BE~7 eV higher due to the Fe_2O_3 oxide phase. The Fe2p1/2 peak is at BE of 724.8 eV and a satellite structure is at BE~8 eV higher. Fe oxide peaks are significantly shifted to higher binding energy than the Fe metal peak [9]. The Cr2p spectrum shows that the Cr2p3/2 and Cr2p1/2 peak appears located at BE of 577.0 and 586.8 eV where Cr_2O_3 is present. The C1s spectrum consists of a main wide structure located at 285.2 eV and a weak wide peak centered around 289.1 eV, which derives from the different compounds forming the adsorbed layer. The first wide peak can be ascribed to the presence of C-C and C-H bonds. The weaker peak at 289.1 eV are indicative for the presence of C=O

The XPS spectra of 60 µm stainless steel surface after thermal treatment to 300 ^{0}C for 2.5 hours is shown in **Figure 6-29**. Fe and Cr spectral features still appear and C and O still exist on the surface at around 284 and 531 eV. The Fe2p, Cr2p, O1s and C1s core level spectra for 60 µm stainless steel after thermal treatment are shown in detail from **Figure 6-30** to **Figure 6-32**. After heating, the BE of Fe2p3/2 peak is shift to 709.9 eV and a satellite structure is at BE~6 eV higher. The Fe2p1/2 peak is at BE of 723.4 eV and a satellite structure is at BE~7 eV higher. This indicates that heating reduce the iron to lower oxidation levels from 3+ to 2+. So the Fe_2O_3 disappear and FeO produce on the surface after thermal treatments. No Cr peak shift is detectable after vacuum heating. The Cr2p spectrum shows that the Cr2p3/2 and Cr2p1/2 peaks still stay the same binding energy as as-received surface, which shows the Cr_2O_3 is present. But the intensity of Cr increases significantly after heating. The surface Cr enrichment results from the high oxidation affinity to form oxides and hydroxides [10]. The driving force for the Cr segregation is the displacement of oxides and hydroxides from Fe to Cr, so the Cr migrates to the surface in order to replace Fe 3+ to Fe 2+ and reduce them to lower oxidised state [10]. The intensity of Fe on the surface as well decreases due to the segregation of Cr. The C1s spectrum loses the C=O component at 289.1 eV and transform to C-O at BE of

286.3 eV. The C-C components still exist and its intensity increases and moves slightly towards low binding energy. This means the intensity of O has been reduced after thermal treatment. However, C has been enriched on the surface, which is from the desorption from the bulk.

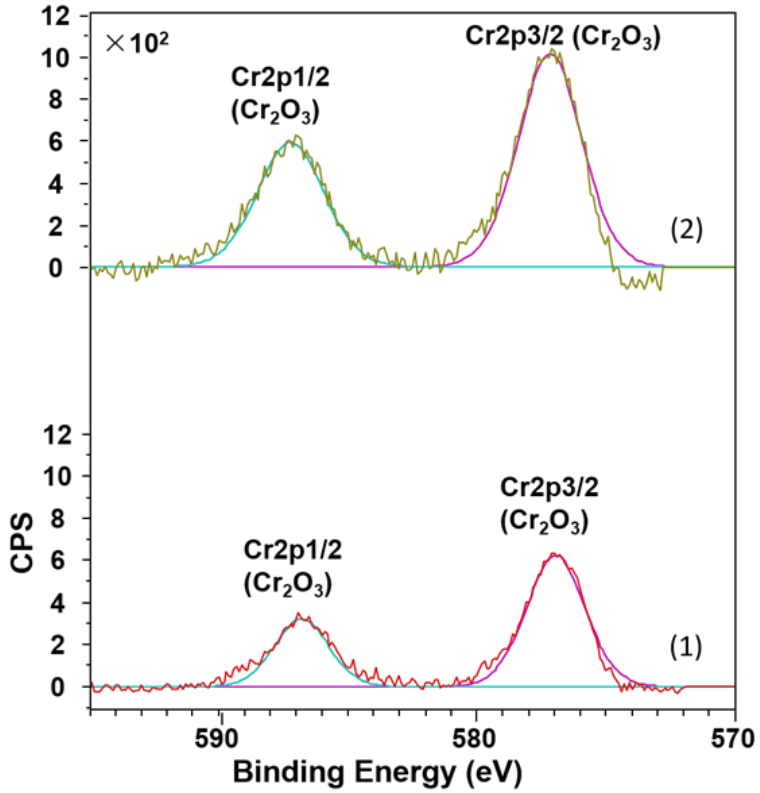

Figure 6-30 The Fe2p spectra for 60 μm stainless steel before and after thermal treatment (1) as-received, (2) heated to 300 ^{0}C for 2.5 hours

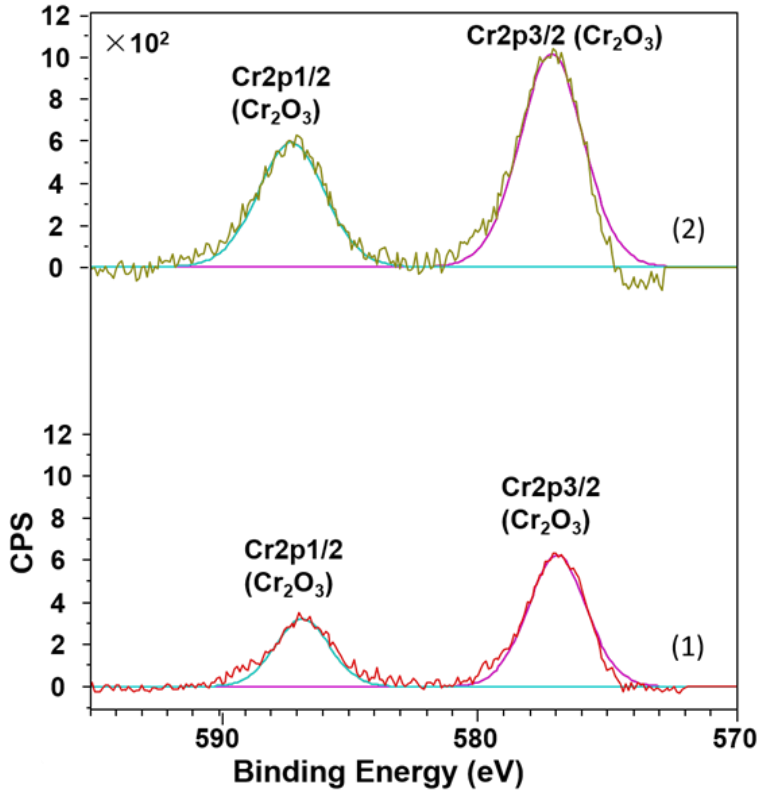

Figure 6-31 The Cr2p spectra for 60 μm stainless steel before and after thermal treatment (1) as-received, (2) heated to 300 ^{0}C for 2.5 hours

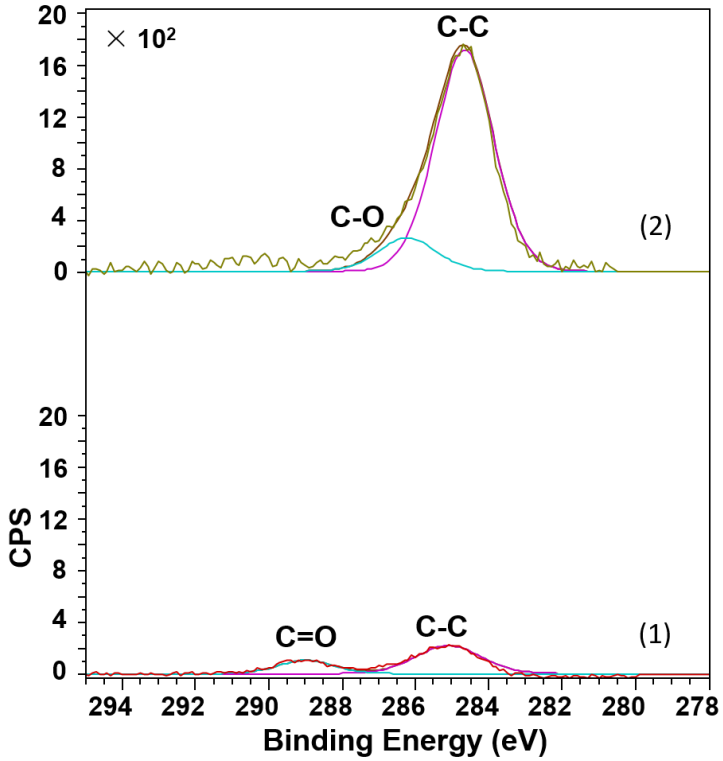

Figure 6-32 The C1s spectrum for 60 μm stainless steel before and after thermal treatment (1) as-received, (2) heated to 300 ºC for 2.5 hours

6.5 The SEY of bulk Ti and Ti powder

In section 6.2.4, nanostructure laser engineered Cu in Air has the lowest SEY, compared with the other laser treated Cu. From the SEM pictures, the top of closed pyramid is covered with nano-spherical coral structures. So in this section, the comparison of Ti powder and bulk Ti will simulate the difference between nanostructure laser engineered Cu and other laser treated Cu. **Figure 6-33** shows that the SEY of bulk Ti and Ti power samples. Ti powder samples are made by gluing the pure Ti powders on the top of stainless steel sample plate. The sizes of Ti powders are ranging from 10 to 120 μm. The δ_{max} of bulk Ti is 2.34 but the δ_{max} of Ti power is only 1.4, which means that the δ_{max} of Ti power is much lower than that of bulk Ti. As the SEY increases with surface density, the density of Ti powder is lower than that of bulk sample.

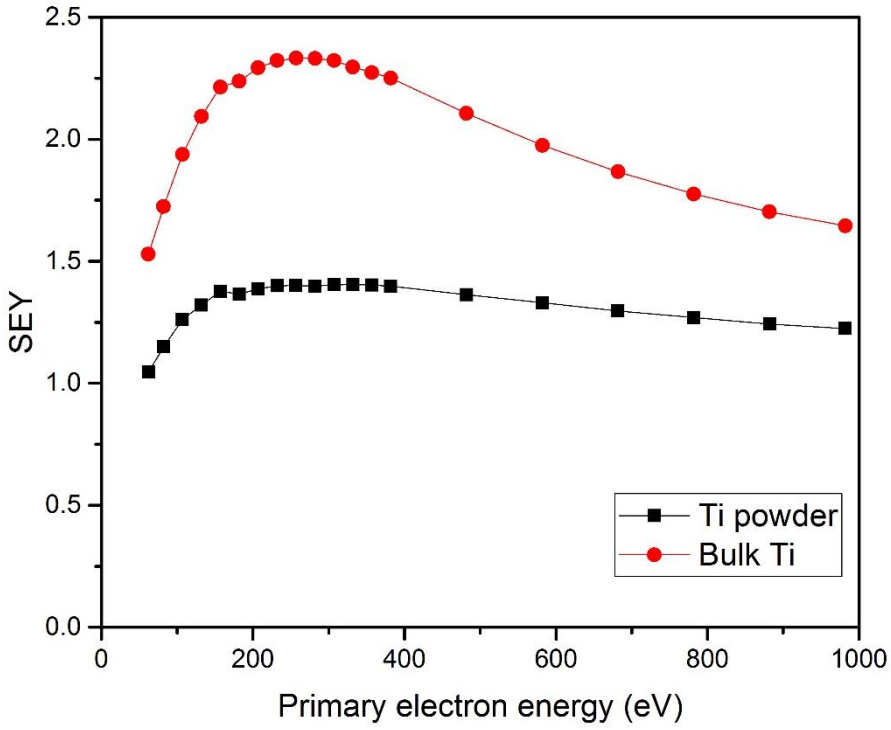

Figure 6-33 the SEY between Ti power and bulk Ti

6.5 Discussion

The laser treated surfaces have been introduced in this chapter. The special pyramid shaped structures increase the roughness of the surface, so the laser treated surfaces have much lower SEY than that of normal surface. The SEY as a function of the primary electron energy is depended by the primary electron

energies and the secondary electron escape depth. The secondary emission process usually contains three steps which are the generation of secondary electrons by primary electrons, transport to the surface with interactions in the escape depth and emission from the surface by overcoming the work function [11]. Increasing the surface roughness is a promising technique to mitigate the electron cloud by suppressing the secondary electron emission [12]. The reason is that the secondary electrons leave from a rough surface and they may again intercept with surrounding substance. Then a big fraction of secondary electrons will be absorbed by the surface instead of escaping from the surface. Therefore, the SEY is critically low [13].

The effects of hatch distances to SEY have also been studied in this section. The SEY of Cu or stainless steel with 50 μm hatch distance is lower than that with 60, 80 μm hatch distances. The reason is similar with suppression of the SEY for a grooved metal surface, which has been described in chapter 2. The effective secondary electron emission is reduced due to the multiple collisions with the grooved surface [14]. A primary electron hits the surface at a point and produces secondary electrons. Due to different emission angles, some of the secondary electrons can escape the groove and move away from the surface. However, the others continue hitting the groove sides. With some probability they will be absorbed, the rest continue generating other secondary electrons. This process may repeat several times until the higher generations of the secondary electron energies are so low that the electrons cannot escape from the surface and they are eventually absorbed by the surface [14, 15]. However, for rectangular grooves, the limitation of this approach is that no suppression effect occurs on the top of the grooves. For example, the structures of Type I with 50 μm hatch distance has a closed square pyramid shaped structure. When the hatch distances get larger, the hollow starts to form the open square based top pyramid (volcano throat like). The structures of Type I with 60 and 80 μm have larger top area than that with 50 μm hatch distance. So the SEY of Cu or stainless steel with 50 μm hatch distance is lowest.

However, the lowest SEY of as-received sample we achieved so far is 0.73. (Type III Cu). The small structures on the top of pyramid form the less density

porous surface, which can also reduce SEY. After several collisions between the nano-spherical coral structures, the primary electrons will be lost into the material.

As NEG coatings have good pumping properties, Ti-Zr-V has been deposited on the Type I and Type III in air. However, after deposition, the surfaces have a large amount of oxygen, which causes the SEYs are to be higher than that of the Type I and Type III in air, respectively.

On the other hand, the E_{max} of these laser treated Cu is around 800 eV, which is much higher than that of untreated bulk copper (250 eV). The E_{max} of laser treated stainless steel in air or in Ar is about 1000 eV and 400 eV, respectively, which are higher than that of untreated bulk stainless steel (250 eV).This means the secondary electrons excited by primary electrons from rough surface reaches the escape depth at higher energy than that from flat surface. From purely geometric argument, an electron hitting on an angled surface will penetrate less than an electron impinging perpendicularly at a fixed primary energy [16]. So in order to achieve the same average penetration on a rough surface, which can be treated as being composed by a lot of small tilted surfaces, the primary electron should have a higher energy [16]. As a result, the E_{max} shift to high energy for laser treated Cu.

Changing surface chemical composition is another way to reduce the SEYs of metals. Oxide contamination layers are formed if the surfaces are exposed to air and as a result, the SEY of metal surfaces are usually higher than those of atomically clean metal surfaces [17]. For example, as-received Al alloys have a very large SEY, which is over 3 [8] However, δ_{max} for the atomically clean Al surfaces is approximately 1.0 [18]. Adsorbed gases and oxidation layers can be removed by surface heating. For example, in all cases of laser treated Cu, oxygen is diffused into black coppers and at the same time CuO transforms to sub-stoichiometric oxide. The SEY of semiconducting metal oxides such as Cu_2O, Nb_2O_5 is usually lower than that of the parent metals [18]. So after heating to 250 ºC for 2 hours, the SEYs of all these blackened coppers are even lower than that of as-received blackening coppers.

6.6 Conclusion

The SEY of metal surfaces modified by a nanosecond pulsed laser irradiation has been studied in this chapter, such as copper, stainless steel and Al alloys. The functions of thermal treatment and electron bombardment have been studied on the laser treated surface alongside with XPS analysis of surface chemical composition. The SEYs of as-received Cu, stainless steel and Al alloys were 1.90, 2.25, 2.55, separately. The SEYs of as-received laser treated Cu, stainless steel and Al alloys were 1.12, 1.12 and 1.45, separately. From XPS analysis, the surface of both normal metals and laser treated metals were covered by oxidized layer. The low value of δ_{max} for as-received laser sample was mainly depended on the surface topography induced by the laser processing. After electron bombardment, the SEYs of laser treated Cu, stainless steel and Al alloys were reduced to 0.78, 0.76 and 0.76, respectively. For example, XPS results of Cu showed that the conditioning effect changed the surface chemistry by gradually building a thin layer of graphitic-like C-C carbon. The intensity of Cu increase and the O peak decreased. The Cu2p spectrum illustrated that the metallic component had gained intensity and was more narrow compared with the as-received surface and the satellite at was reduced.

Then three types of laser treated Cu structures in air or Ar have been studied as a function of thermal treatment and electron conditioning. The SEM graphs for these three types of structures described the differences between each other. For type I structures in Air, hatch distances also effected the shape of the morphology. Type I with 50 μm hatch distance had closed square pyramid shaped structure. However, with the hatch distances getting larger, a hollow started to form the open square based top pyramid. The SEY of type I structure with 50 μm hatch distance had the lowest value (0.75). The SEYs of type I structure with 60 μm and 80 μm were 0.75 and 0.80, respectively. The open pyramid was similar with rectangular grooves. There was no suppression effect occurs on the top of the grooves. However, the structures of Type I with 50 μm hatch distance had a closed square pyramid shaped structure, which meaned that the top area is smallest. The structures of Type I with 60 and 80 μm had

larger top area than that with 50 μm hatch distance. So the SEY of Cu with 50 μm hatch distance was lowest. SEYs of type I structures in Ar had the same trend. The SEYs of type I structures in Ar with 50, 60 and 80μm hatch distance were 0.79, 0.84 and 0.94, respectively. The SEYs of type I structure in Ar was larger than those in air. After thermal treatments, the SEYs of type I structure in both air and Ar decreased, which were due to reduce of oxygen on the surface. Cu2p3/2 and Cu 2p1/2 peaks moved to the lower binding energy, which were associated with Cu_2O. Type II structures showed a groove surface. The SEY of the as-received grooved Cu in air with 50 μm hatch distance was 0.76 and 0.57 after heating. Similarly, the SEY of as-received grooved Cu in Ar 50 μm hatch distance was 0.89 and 0.77 after heating, which was higher than that in air. Type III structure was covered with nano-spherical coral structures on the top of the closed pyramid. The SEY of type III laser treated Cu in air 50 μm hatch distance was 0.73, which was the lowest value obtained so far for as-received sample. The small structures on the top of pyramid form the less density porous surface, which can also reduce SEY. After heating, the SEY decreased to 0.60. The E_{max} of these laser treated Cu was around 800 eV, which was much higher than that of untreated bulk copper (250 eV). The reason was that an electron hitting on an angled surface would penetrate less than an electron impinging perpendicularly at a fixed primary energy.

Ti-Zr-V coatings have been to deposit on the Type I Cu with 60 μm hatch distance in air and Type III Cu. However, the δ_{max} of as-received Ti-Zr-V on the Type I Cu with 60 μm hatch distance in air was 0.91, which was higher than blackened Cu itself (0.75). After heating to 200 ºC for 2.5 hours, it was reduced to 0.62. The δ_{max} of the Type III Cu in Air was 0.73, which was much lower than that of as-received Ti-Zr-V on the Type III Cu in Air (0.99). After heating to 300 ^{0}C, the δ_{max} of Ti-Zr-V on the Type III Cu in Air dropped to 0.75. However, it was still higher than that of as-received Type III Cu in Air. From XPS analysis, Ti-Zr-V did not cover the whole laser treated Cu surface. It also clearly showed that deposition of Ti-Zr-V produced a large amount of oxygen and some carbon on the surfaces. The oxygen on the Type III Cu in Air was even more than that of Type I with 60 μm hatch distance in Air.

The SEYs of laser treated stainless steel in Air and Ar with varying

microstructure distances have been described simply in the last section. The SEY curves of as-received 50 μm, 60 μm and 80 μm stainless steel in Air had the similar trend. It increased with increasing the primary electron energy and reaches the maximum point at 1000 eV, which was 0.92, 1.0 and 1.1 for 50, 60 and 80 μm, respectively. However, the Ep(δ) of stainless steel in Ar increased with gradually reducing gradient at low primary electron energies and reached the highest point around 400 eV. Then it increased with primary electron energy slowly after 400 eV. δ_{max} of as-received stainless steel in Ar were 0.98, 1.18, 1.40 for 50, 60 and 80 μm, respectively.

Reference

[1] Tang G, Hourd AC, Abdolvand A. Nanosecond pulsed laser blackening of copper. Applied Physics Letters 2012;101:231902.

[2] Valizadeh R, Malyshev OB, Wang S, Zolotovskaya SA, Allan Gillespie W, Abdolvand A. Low secondary electron yield engineered surface for electron cloud mitigation. Applied Physics Letters 2014;105:231605.

[3] Larciprete R, Grosso DR, Commisso M, Flammini R, Cimino R. The Chemical Origin of SEY at Technical Surfaces. Conf Proc 2013.

[4] Grosso DR, Commisso M, Cimino R, Larciprete R, Flammini R, Wanzenberg R. Effect of the surface processing on the secondary electron yield of Al alloy samples. Physical Review Special Topics - Accelerators and Beams 2013;16:104-.

[5] Cimino R, ., Commisso M, ., Grosso DR, Demma T, ., Baglin V, ., Flammini R, ., et al. Nature of the decrease of the secondary-electron yield by electron bombardment and its energy dependence. Physical Review Letters 2012;56:112-8.

[6] Larciprete R, Grosso DR, Commisso M, Flammini R, Cimino R. Secondary electron yield of Cu technical surfaces: Dependence on electron irradiation. Physical Review Special Topics - Accelerators and Beams 2013;16:011002.

[7] Ghijsen J, Tjeng LH, van Elp J, Eskes H, Westerink J, Sawatzky GA, et al. Electronic structure of ${\mathrm{Cu}}_{2}$O and CuO. Physical Review B 1988;38:11322-30.

[8] Baglin V, J.Bojko, Gröbner O, Henrist B, Hilleret N, Scheuerlein C. The Secondary Electron Yield Of Technical Materials And Its Variation With Surface Treatments. EPAC 2000. Vienna, Austria2000. p. 217-21.

[9] Yamashita T, Hayes P. Analysis of XPS spectra of Fe2+ and Fe3+ ions in oxide materials. Applied Surface Science 2008;254:2441-9.

[10] Cavallini M. XPS study of mechanically polished stainless steel surfaces. Materials Chemistry 1980;5:29-35.

[11] Cazaux J. About the secondary electron yield and the sign of charging of electron irradiated insulators. European Physical Journal Applied Physics 2001;15:167-72.

[12] Suetsugu Y, Fukuma H, Shibata K, /KEK T, Pivi M, Wang L, et al. Experimental Studies on Grooved Surfaces to Suppress Secondary Electron Emission2010.

[13] Bruining H. Physics and applications of secondary electron emission: Pergamon Press; 1954.

[14] Wang L, Raubenheimer TO, Stupakov G. Suppression of secondary emission in a magnetic field using triangular and rectangular surfaces. Nuclear Instruments & Methods in Physics Research 2007;571:588-98.

[15] Pivi M, King FK, Kirby RE, Raubenheimer TO, Stupakov G, Le Pimpec F. Sharp reduction of the secondary electron emission yield from grooved surfaces. Journal of Applied Physics 2008;104:104904.

[16] Vallgren CY. Low Secondary Electron Yield Carbon Coatings for Electron Cloud Mitigation in Modern Particle Accelerators: Chalmers University of Technology; 2011.

[17] Henrist B, Hilleret N, Scheuerlein C, Taborelli M. The secondary electron yield of TiZr and TiZrV non-evaporable getter thin film coatings. Applied Surface Science 2001;172:95–102.

[18] Hilleret N, Scheuerlein C, Taborelli M. The secondary-electron yield of air-exposed metal surfaces. Appl Phys A 2003;76:1085-91.

Chapter 7. Conclusions and future plans

7.1 Conclusions

The e-cloud limits the operation of particle accelerators with positively charged beams of high intensity and short bunch spacing. The original electrons come from residual gas molecules, photoelectron and secondary electron emission. If the secondary electron yield of the chamber is greater than one, beam induced multipacting will happen, which will lead to the build-up of e-cloud. E-could can affect the operation and performance of accelerator in many ways, such as the increase of vacuum pressure, beam instability, beam loses and so on. This thesis is to systematically study low SEY materials for accelerator chambers. Two series of materials have been studied, which are transition metals and their coatings and laser treated metals.

Thesis starts from the descriptions of the basic theory of SEY. In chapter 2, the basics of SE emission and energy distribution of SE emission have been introduced. Theory calculation of SE emission has been derived. Then existing methods used to suppress electron clouds have been discussed. At the end, some low SEY materials have been given as examples. Chapter 3 described the experiment methods and procedures in this thesis. Transition metal coatings are prepared by PVD and the blackened metal surfaces are produced by nanosecond pulsed laser. Characterization methods include the SEY measurement, SEM, XRD and XPS. Surface treatments consist of electron irradiation and in-situ thermal treatment method. The SEY measuring facility is design and built by myself, which has been introduced in chapter 4. The SEY measuring facility consist of load lock chamber, SEY measurement chamber and surface treatment and analysis chamber. Beam profile of the Kimball electron gun has been measured by phosphor screen and wire scanner methods in order to make sure the spot size of primary electron. Bias effect has been studied in order to receive almost all the secondary electron emission. Finally, error analysis of SEY measurements has been calculated.

In chapter 5, the SEYs of the transition metals and their alloys coatings are

studied as a function of electron conditioning and thermal treatment alongside with XPS analysis. The SEYs of as-received bulk Ti, Zr, V and Hf are 2.30, 2.31, 1.72 and 2.45, respectively. The SEY of Ti, Zr, V and Hf coatings have the similar trend, which are 1.74, 2.23, 1.58 and 2.34, respectively. As the SEY increases with Z atomic number and Hf (72) has the highest atomic number, then Hf has the biggest SEY for both bulk samples and thin films. SEY is also influenced by the sample density. So the SEY of the thin film is much lower than that of bulk sample for the same materials. Expert material characteristics, secondary electron emission as a surface process is influenced by the modifications of a material's outer layers. In this thesis, electron bombardment and thermal treatment have been studied on bulk and thin film samples. After electron bombardment, the SEYs of bulk Ti, Zr, V and Hf are 1.19, 1.27, 1.48 and 1.40 with the electron doses of 7.9×10^{-3}, 6.4×10^{-3}, 1.3×10^{-3} and 5.2×10^{-3} $C\cdot mm^{-2}$, respectively. The SEYs of Ti, Zr, V and Hf thin films are 1.21, 1.30, 0.94 and 1.08 after different electron dose bombardments. The decreases of SEY is due to the graphitization on the surfaces. Carbon contents on the surfaces increases due to the electron-induced carbon deposit by cracking the carbon-containing residual gas molecules. So the electron conditioning is accompanied by a clear chemical modification and produces a graphite-like layer on the surface. The SEYs of as-received samples are increased by adsorbed gases and oxidation layers on the surface, which can be removed by surface heating. After thermal treatment, the oxygen on the surface diffuses into the bulk via the grain boundaries and the surface transforms from an oxide to a metallic state. The XPS results show clearly that metal oxide has been removed and the surface has transformed to the metal state via oxygen diffusing into the bulk. The SEY of Ti-Zr-V on the stainless steel is 1.82, which is almost the average of the SEY of the individual metal thin film (1.85). However, the SEY of Ti-Zr-V on the stainless steel is 1.34, which is higher than the average of the SEY of the individual metal coatings (1.0). The reason is that the thermal treatment can change the surface concentration.

In chapter 6, the laser treated surfaces have been introduced. Increasing the surface roughness can suppress the secondary electron emission, which is a

promising technique to mitigate the electron cloud. Primary electron hit the surface and produces secondary electrons. Due to different emission angles of secondary electrons, some of the secondary electrons can escape from the surface and move away. But the rest will continue hitting the surrounding surfaces. With some probability they will be absorbed, the others continue generating other secondary electrons. This process may repeat several times until the higher generations of the secondary electron energies are so low that the electrons cannot escape from the surface and they are eventually absorbed by the surface The special pyramid shaped structures of laser treated samples increase the roughness of the surfaces, so the laser treated surfaces have much lower SEY than that of normal surface. The effects of different hatch distances and atmosphere to SEY have also been studied in my thesis. The SEY for Cu or stainless steel with 50 μm hatch distance is lower than that with 60 and 80 μm hatch distance. The difference is related to the surface structures. For example, the structures of Type I with 50 μm hatch distance has a closed square pyramid shaped structure. But the surfaces of Type I with 60 and 80 μm hatch distances form the open square based top pyramid (volcano throat like). Then the structures of Type I with 60 and 80 μm have larger top area than that with 50 μm hatch distance. So the SEY of Type I with 50 μm hatch distance is lowest. The lowest SEY of an as-received sample in my thesis is 0.73. (Type III Cu). The small structures are on the top of pyramid, which forms the less density porous surface. So the SEY reduces even lower. After several collisions between the nano-spherical coral structures, the primary electrons will lost into the material. NEG coatings also have been deposited on the blackened surfaces. However, after deposition, the surfaces have a large amount of oxygen, which causes the SEYs are much higher than that of blackened substrates. The E_{max} of these laser treated samples moves to higher energy. From purely geometric argument, an electron hitting on an angled surface will penetrate less than an electron impinging perpendicularly at a fixed primary energy. The primary electron should have a higher energy in order to achieve the same average penetration on a rough surface. The effects of thermal treatments and electron bombardments on laser treated surfaces have also been studied. Similarly, after each treatments, the SEY of the laser treated surfaces reduces.

7.2 Future plans

For transition metal and their coatings: more research for V samples need to be done in order to find out the reason that it has much lower SEY than that of Ti, Zr and V samples. Besides that, the XRD needs to be done on the thin films to find out the relations between the crystalline size and activation temperature. For laser treated samples: More research experiments need to be done in order to explain the reason that the SEY of laser treated samples in Ar are higher than that on Air. The study of laser treated stainless steel should be continued.

List of publications

1. S Wang，OB Malyshev，R Valizadeh，EA Seddon，M.D. Cropper，THE SECONDARY ELECTRON YIELD FROM TRANSITION METAL，Proceedings of IPAC2014, Dresden, Germany.

2. Valizadeh R, Malyshev OB, Wang S, Zolotovskaya SA, Allan Gillespie W, Abdolvand A. Low secondary electron yield engineered surface for electron cloud mitigation. Applied Physics Letters 2014;105:231605.

3. S Wang，S.A. Zolotovskaya, R. Valizadeh, O.B. Malyshev, J. Smith, W. A. Gillespie, A. Abdolvand, REDUCTION OF SECONDARY ELECTRONS ON A LASER MICROSTRUCTURED SURFACE, In preparation.

4. Sihui Wang, Oleg B. Malyshev, Reza Valizadeh, Elaine A. Seddon, Mike D. Cropper , The secondary electron yield from transition metals , In Preparation.